

Coherent Dijets in Ultra-peripheral Pb+Pb Collisions at

$$\sqrt{s_{NN}} = 5.02 \text{ TeV}$$

By

Samuel Boren

Submitted to the graduate degree program in Department of People who read Abstracts and the Graduate Faculty of the University of Kansas in partial fulfillment of the requirements for the degree of Doctor of Philosophy.

MEMBER 1, Chairperson

MEMBER 2, Occasional Visitor

Committee members

MEMBER 3

MEMBER 4, The One Who Never Answers Email

The One with an Extra Long Name

The Fifth Beatle

Date defended: _____ October 02, 2016 _____

The Thesis Committee for Samuel Boren certifies
that this is the approved version of the following thesis :

Coherent Dijets in Ultra-peripheral Pb+Pb Collisions at $\sqrt{s_{NN}} = 5.02$ TeV

MEMBER 1, Chairperson

Date approved: _____ October 06, 2016 _____

Abstract

This dissertation describes the study of coherent dijet photoproduction in ultra-peripheral heavy-ion collisions. Ultra-peripheral collisions have impact parameters larger $2R$ where R is the radius of the heavy-ion. These collisions are mediated entirely by the exchange of low-virtuality photon according to the Weizacker-Williams approximation. The angular correlation of coherently photoproduced dijets is sensitive to elliptic gluon distribution. The azimuthal anisotropy of the ion recoil momentum P_T and the dijet transverse momentum Q_T is presented for two bins of Q_T : $0 < Q_T < 5$ GeV and $5 < Q_T < 10$ GeV.

Acknowledgements

Contents

1	Introduction	1
1.1	The Standard Model	1
1.2	Quantum electrodynamics	3
1.3	Quantum chromodynamics	4
1.4	Deep inelastic scattering	6
1.5	PDFs	8
1.6	Quark gluon plasma	9
1.7	Wigner distribution	15
2	Ultra-peripheral collisions and photoproduction	20
2.1	Ultra-peripheral heavy-ion collisions	20
2.2	Vector meson photoproduction	23
2.3	Photon-photon interactions	29
2.4	Coherent dijet photoproduction and diffraction	31
3	The experiment	40
3.1	Large Hadron Collider	40
3.1.1	ATLAS	40
3.1.2	ALICE	41
3.1.3	LHCb	41
3.1.4	TOTEM	41
3.1.5	CASTOR	42
3.2	Compact Muon Solenoid	42

3.2.1	Tracker	43
3.2.1.1	Pixel tracker	45
3.2.1.2	Strip tracker	46
3.2.2	Electromagnetic calorimeter	46
3.2.3	Hadronic calorimeter	47
3.2.3.1	Hadronic forward calorimeters	48
3.2.4	Muon detector	50
3.2.5	Zero degree calorimeter	51
3.2.6	Particle flow algorithm	51
4	Measuring luminosity	54
4.1	Instantaneous luminosity	54
4.2	Luminometers	55
4.2.1	Pixel cluster counting	55
4.2.2	Pixel luminosity telescope	56
4.2.3	Hadronic forward calorimeter	57
4.2.4	Fast Beam Conditions Monitor	57
4.3	Van de Meer scanning calibration	58
4.4	Corrections to VDM scans	58
4.5	Systematic uncertainty	59
4.6	Author’s contributions	60
5	Trigger development and performance	64
5.1	Introduction to triggering	64
5.2	Triggering at CMS	65
5.3	Author’s contributions	68
5.3.1	Pb+Pb 2015 UPC Triggers	68
5.3.2	p+Pb 2016 UPC Triggers	69

5.4	Studies from trigger menus	70
6	Data analysis	72
7	Systematic uncertainties	77
8	Results and conclusions	78
A	Monte Carlo Generation and Reconstruction	94

List of Figures

1.1	QED components of Feynman Diagrams [13].	4
1.2	QCD coupling constant as a function of Q^2 [19].	6
1.3	Collision cross section as a function of Bjorken- x , with data compared to HERA-PDF calculations [26].	7
1.4	Subnuclear tomography (Ask Daniel again)	9
1.5	QCD phase diagram showing the temperature T as a function of baryon chemical potential μ_B . Different phases such as the critical point, QGP, and hadron gas are seen [37].	10
1.6	J/Ψ suppression in Pb-Pb collisions [34]	11
1.7	Heavy-ion collision overlap region	12
1.8	v_2 vs collision energy [34]	13
1.9	STAR $Au + Au$ at $\sqrt{s_{NN}} = 130$ GeV: (a) v_2 as a function of centrality with hydrodynamic calculations (empty rectangles) and data (black dots); (b) v_2 as a function of p_T [50].	13
1.10	CMS (a) pPb and (b) PbPb, angular correlations [43]	14
1.11	Pictorial time-line of the Universe, showing phase transitions [52].	15
1.12	Space-time diagram of a heavy-ion collision [54].	16
1.13	Interconnectedness of Parton Distributions [33]	17
1.14	Feynman Diagram of Coherent Dijets in Dipole Framework [31]	18
1.15	Theoretical Quark GTMDs [62]	19
2.1	(a.) electromagnetic field of stationary charge (b.) eletromagnetic field of boosted charge [65]	21

2.2	Ratio of H1 data cross-section to NLO-QCD cross-section [70]	23
2.3	$AuAu \rightarrow AuAu\rho^o$, (a.) UPC exclusive ρ^o diagram, (b.) with mutual nuclei excitation [85]	24
2.4	UPC exclusive $\rho^o p_T$, (a.) topology triggered (b.) minimum bias triggered [85]	25
2.5	$\gamma + \text{proton} \rightarrow J/\Psi + \text{proton}$ cross-section [91].	25
2.6	(a) dimuon invariant mass spectrum, (b) dimuon p_T spectrum [94].	26
2.7	Differential cross section versus rapidity for coherent J/Ψ production in ultra-peripheral PbPb collisions at $\sqrt{s_{NN}} = 2.76\text{TeV}$ [94]	27
2.8	Υ photoproduction mass spectrum [114]	28
2.9	$\sigma_{\Gamma_{\gamma p}}$ vs $W_{\gamma p}$ [114]	28
2.10	$\gamma\gamma$ Diagrams of light-by-light scattering, (a.) channels, (b.) analogous [115]	30
2.11	$\gamma\gamma$ kinematics, (a.) acoplanarity, (b.) invariant mass [115]	30
2.12	Event Display of ATLAS photon-photon scattering [116]	31
2.13	Feynman diagrams for coherent jet photoproduction in (a) direct-photon in ep, (b) resolved-photon in ep [70]	33
2.14	Ratio of H1 data cross-section to NLO-QCD cross-section [70]	34
2.15	Beam envelope vs. distance to vertex in H1 [70]	35
2.16	H1, Diffractive $e + p$ products, Kinematics [125]	36
2.17	H1, Diffractive Dijets, Cross Section [125]	37
2.18	ZEUS, Diffractive Dijets, Kinematics [121]	38
2.19	ATLAS UPC Dijets, (left) p_T and (right)invariant mass [127]	39
3.1	CMS Detector [136]	43
3.2	CMS radial cross-section [137]	44
3.3	Pseudorapidity acceptance of tracker [139]	45
3.4	ECAL components [140]	46
3.5	Reconstructed data, ECAL energy resolution [142]	47
3.6	L1 trigger, ECAL energy resolution [142]	48

3.7	HCAL energy resolution [142]	49
3.8	HCAL Components [142]	49
3.9	Pseudorapidity acceptance of muon detector [142]	51
3.10	Performance of particle flow alorgithm compared to calorimeter readout [151] . .	53
4.1	PLT triple coincidence	56
4.2	PCC VdM Scans [152]	58
4.3	Systematic Uncertainty During 2015 pp Run [152]	60
4.4	Luminosity by CMS fill.	61
4.5	CMS Run Registry.	62
4.6	CMS lumi during HI-2015.	62
4.7	CMS Lumi by Era.	63
5.1	Rossi circuit with three Geiger-Muller coincidence circuits [159]	64
5.2	Flow of information in L1 trigger	66
5.3	Leading tower energy distribution in HF	66
5.4	High multiplicity PbPb collision	67
5.5	UPC Upsilon candidate	67
5.6	Example of trigger rate.	68
6.1	Raw ϕ distribution.	73
6.2	Mixed ϕ distribution.	74
6.3	Subtracted ϕ distribution.	75
6.4	Final ϕ distribution.	76
A.1	RAPGAP process: boson-gluon fusion.	94
A.2	Left: Energy Distribution Before Fitting, Right: Energy Distribution After Fitting .	95

List of Tables

5.1	L1 Trigger Average Rates for Run 263757	69
5.2	HLT Average Rates for Run 263757	69
5.3	L1 Trigger Average Rates for Run 285530	70
5.4	HLT Average Rates for Run 285530	70

Chapter 1

Introduction

Microseconds after the big bang, the universe was filled with a hot, dense state of strongly interacting subnuclear particles [1]. There is evidence that this phase of matter, the quark gluon plasma (QGP), is reproduced in the high energy densities reached by ultra-relativistic heavy-ion collisions [2]. Measurements at the Relativistic Heavy Ion Collider (RHIC) and the Large Hadron Collider (LHC) are consistent with the QGP having the sheer viscosity of a perfect fluid [3]. Heavy-ion initial state properties must be rigorously measured to distinguish between the effects of the QGP and of the inherent properties of the nucleus.

This thesis seeks to further knowledge of initial state phenomena in heavy-ion collisions by measuring the gluon distribution within the nucleus. In the context of coherent dijet photoproduction from ultra-peripheral collisions (UPC), the distribution of the so-called "elliptic" gluons is encoded in the angular correlation of the dijet[4]. In UPCs all interactions between nuclei are from electromagnetic or electroweak processes [5]. Such photo-nuclear interactions are described via the equivalent photon approximation from the Weizacker-Williams formalism [6][7].

Before discussing the physics of ultra-peripheral collisions to that of UPC dijets, we will give an overview of the standard model of high energy physics, followed by an introduction to relativistic heavy-ion collisions and how these are connected to photon-induced interactions.

1.1 The Standard Model

The Standard Model describes the fundamental particles of the universe in terms of fermions and bosons. Fermions are particles with half-integer spin, while bosons have integer-spin. Fermions

must obey the Pauli Exclusion Principle: only one fermion at a time can occupy a given state. However, multiple bosons can simultaneously occupy a specific state [8]. Subnuclear particles – protons and neutrons – contain large numbers of both fermions and bosons. Fermions and bosons have different statistical properties. Fermi-Dirac statistics describe the energy distribution of fermions. Likewise, the boson energy distribution is described by Bose-Einstein statistics [9].

Among the fermions are the leptons, neutrinos, and quarks. The leptons consist of the electron, muon, and tau, as well as their anti-particles. The leptons are believed to be fundamental: high energy experiments have yet to observe internal lepton-structure. Neutrinos are weakly interacting particles detected primarily through the precise measuring of missing transverse energy in the products of particle collisions. Quarks are the constituent particles of baryons, which contain three valence quarks, and mesons, which contain two valence quarks. In addition to the valence quarks are the sea quarks, which appear and disappear as quark-antiquark pairs within hadrons. The hadrons are particles made of quarks and gluons. Gluons are particles that mediate the strong nuclear force; likewise, photons mediate the electromagnetic force, and weak-gauge bosons mediate the weak nuclear force. A fourth boson, the graviton, is expected to transmit the gravitational force, but this particle has not been observed [10].

The behavior of fundamental particles is best described within the framework of quantum field theory (QFT). QFT defines a Lagrangian for fundamental particles. This Lagrangian then predicts the outcome of particle collisions. Different terms in the Lagrangian correspond to the various interactions between particles. The Standard Model Lagrangian, $\mathcal{L}_{StandardModel}$ can be broken down into three basic terms:

$$\mathcal{L}_{StandardModel} = \mathcal{L}_{QED} + \mathcal{L}_{QCD} + \mathcal{L}_{Higgs} + \dots, \quad (1.1)$$

where \mathcal{L}_{QED} is the QED Lagrangian, \mathcal{L}_{QCD} is the QCD Lagrangian, and \mathcal{L}_{Higgs} is the Higgs Lagrangian. The QED and QCD Lagrangians will be the most important in what follows [10].

The most accessible approach to quantum field theory is through the use of Feynman diagrams. First, one imagines an interaction between particles. Then, one draws this process into a Feynman diagram, which is essentially a pictorial representation of exchanges between particles. The La-

grangian can be interpreted into Feynman rules. These rules describe how the Feynman diagram translates into a calculation for the quantum mechanical amplitude of the process. The quantum mechanical amplitude, in turn, is proportional to the cross-section of the process. This is important because, sense the cross-section is invariant between experiments, one can use it to effectively test for invariant quantities in the Lagrangian [11].

1.2 Quantum electrodynamics

Quantum electrodynamics (QED) is a theory of electromagnetic interactions in terms of relativistic quantum field theory. The QED Lagrangian is,

$$\mathcal{L} = \bar{\psi}(i\gamma^\mu D_\mu - m)\psi - \frac{1}{4}F_{\mu\nu}F^{\mu\nu}, \quad (1.2)$$

where ψ is spin- $\frac{1}{2}$ field, γ^μ are the Dirac matrices, D_μ is the gauge covariant derivative, m is the electron mass, and $F_{\mu\nu}$ is the electromagnetic field tensor [11].

QED addresses three specific processes: photon motion, electron motion, and the emission or absorption of a photon by an electron. First a Lagrangian is established based on Maxwell's laws and quantum mechanics. The photon constitutes a spin-1 solution to the differential equations derived from the QED Lagrangian. Likewise, electrons are described, at non-relativistic scales, by the Schrödinger equation, and at relativistic scales by the Dirac equation. Figure 1.1 shows the resulting processes allowed by QED: the translation of an electron, the translation of a photon, and the scattering of a photon off an electron [12].

The QED coupling constant, α_{em} , is approximately 1/137 at perturbative scales [14]. In general, the cross section of a given process is proportional to the $(\alpha_{em})^n$ where n is the number of vertices in the Feynman diagram. The more complex the Feynman diagram, the smaller its cross section. However, at small scales, i.e. non-perturbative momentum transfers Q^2 , the coupling constant increases. α_{QED} is defined as

$$\alpha_{QED}(Q^2) = \frac{\alpha_{em}}{(1 - \frac{\alpha_{em}}{3\pi}\ln(\frac{Q^2}{m^2}))}, \quad (1.3)$$

where $\alpha_{QED}(Q^2)$ is the QED coupling constant at high Q^2 , and m is the electron mass [15]. High

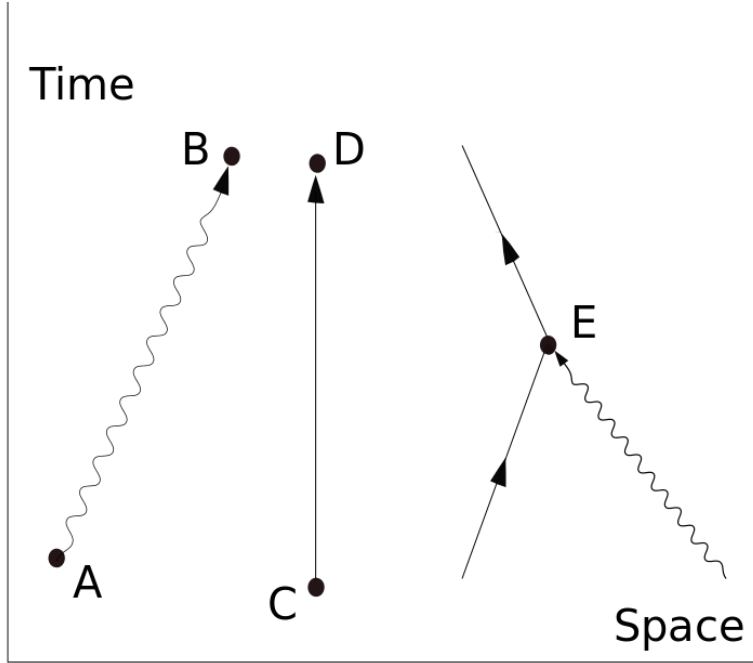


Figure 1.1: QED components of Feynman Diagrams [13].

values of Q^2 are non-perturbative because, at small scales and high momentum, the fluctuation of photons into electron-positron pairs begins to saturate. Particle and anti-particle pairs can pop into exist, persist a short time, and then annihilate so long as quantum numbers are conserved.

1.3 Quantum chromodynamics

The parton model, first proposed by Richard Feynman, posits that hadrons in general, and nucleons in specific, are made of more fundamental constituent particles which may or may not be the quarks implied by the SU(3) symmetry. In addition to the quarks, the partons also include any field quanta associated with nuclear forces. In time, these field quanta are named "gluons".

The quarks are a family of fermions that compose the baryons and the mesons. Baryons consist of three quarks in a color neutral state, while mesons consist two quarks in a color neutral state. "Color" in this context refers to the six kinds of strongly-interacting charge available to quarks: red and anti-red, blue and anti-blue, and green and anti-green. Color charge has no relation to optical phenomena, but provides a useful analogy for the stable combinations of quarks. The net color-

charge of a baryon or meson is colorless. By way of analogy, a red quark, green quark, and blue quark can together form a hadron, in the way that conventional red, green, and blue can together form white [16].

Gluons are the QCD analogues of the photons in QED. Gluons are spin-1 and massless, but unlike photons, which do not carry electromagnetic charge, gluons carry strongly-interacting charge [17]. The QCD Lagrangian, which encodes the interactions of gluons and quarks, is

$$\mathcal{L}_{QCD} = \bar{\psi}_i (i(\gamma^\mu D_\mu)_{ij} - m \delta_{ij}) \psi_j - \frac{1}{4} G_{\mu\nu}^a G_a^{\mu\nu}, \quad (1.4)$$

where m now represents the quark mass, the δ_{ij} is the delta function and $G_{\mu\nu}^a$ is gluon field tensor,

$$G_{\mu\nu}^a = \partial_\mu \mathcal{A}_\nu^a - \partial_\nu \mathcal{A}_\mu^a + g f^{abc} \mathcal{A}_\mu^b \mathcal{A}_\nu^c. \quad (1.5)$$

The SU(3) group of the quarks is indexed as i, j, \dots ; the adjoint SU(3) group, for the gluons, is indexed a, b, c . \mathcal{A}_ν^a is the gluon field, f^{abc} are the SU(3) structure constants, and g is the strong coupling [18].

Unlike QED, the QCD coupling increases with distance [19]. Figure 1.2 shows the running of the QCD coupling with Q^2 :

$$\alpha_{QCD}(Q^2) = \frac{4\pi}{(11 - \frac{2}{3}n_f)\ln(\frac{Q^2}{\Lambda_{QCD}^2})}, \quad (1.6)$$

where n_f is the number of quark flavors, Q^2 is the momentum transfer, and Λ_{QCD}^2 is the mass scale [20]. The running coupling has the practical consequence of the strong-interactions being stronger in high momentum transfer collisions. The direct results of the running QCD coupling include the dual phenomena of asymptotic freedom and color confinement. At large distances, string tension describes the binding force of the quarks. At short distances, however, Coulomb-like interactions dominate [21]. The QCD coupling constant can be measured via the cross-section of inelastic proton-proton collisions, and also the cross section of electron-positrons into triple jets [22].

[something about pQCD and NLO-pQCD] [23][24].

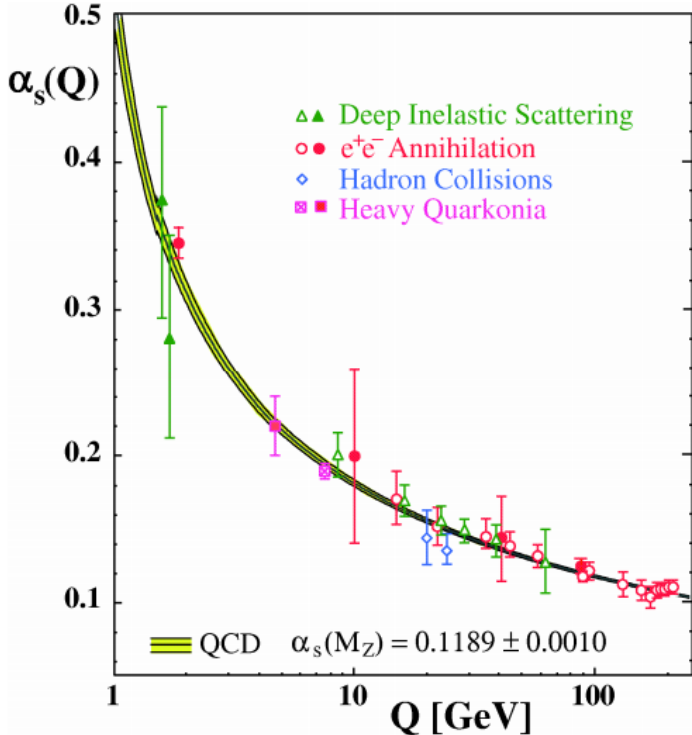


Figure 1.2: QCD coupling constant as a function of Q^2 [19].

1.4 Deep inelastic scattering

At the turn of the century, Ernst Rutherford probed the gold atom by bombarding a gold sheet with alpha-particles. The angular distribution of the scattered alpha-particles demonstrates that the mass of the atom is concentrated in a small volume, i.e, the atom is mostly empty space. Further experiments revealed that the atomic nuclei consisted of separate positively and neutrally charged particles: protons and neutrons. Scattering experiments are the basic tool for exploring the nucleus. In particular DIS commonly refers to the scattering of a lepton off hadrons. For example, experiments at HERA focused on electron-proton collisions. In these collisions, the electron was used as a source of photons and neutrinos. When these particles scatter off the proton, the dependence of the collision cross section, on momentum transfer and scattering angle of the source electron, reflects the structure of the proton. DIS experiments provided the first evidence of two phenomena: the parton model and Bjorken-scaling.

The momentum transferred, Q^2 , is an important quantity for characterizing DIS measurements.

In addition to Q^2 , Bjorken- x is necessary to describe the nuclear phase space. Bjorken- x represents the momentum fraction of partons. In the context of lepton-proton scattering, it was observed that at high momentum transfers the structure functions of the proton were functions of Q^2/v , where Q^2 is the squared four-momentum of the virtual photon emitted by the electron, and v is the energy lost by the electron in the collision [21].

"Scaling" is an interpretation of the data from DIS. First proposed by James Bjorken, scaling is reflected in the incoherence of photon-proton interactions at photon energies above $1 \text{ GeV}/c$ [25]. Predictions from perturbative QCD are in good agreement with DIS data from HERA, as seen in figure 1.3 [26]. In this graph the Bjorken- x momentum fraction is designated x , and σ_r represents the F_2 structure function, and Q^2 is the transferred momentum from the electron to the proton. The order of magnitude of σ_r set by the Bjorken- x .

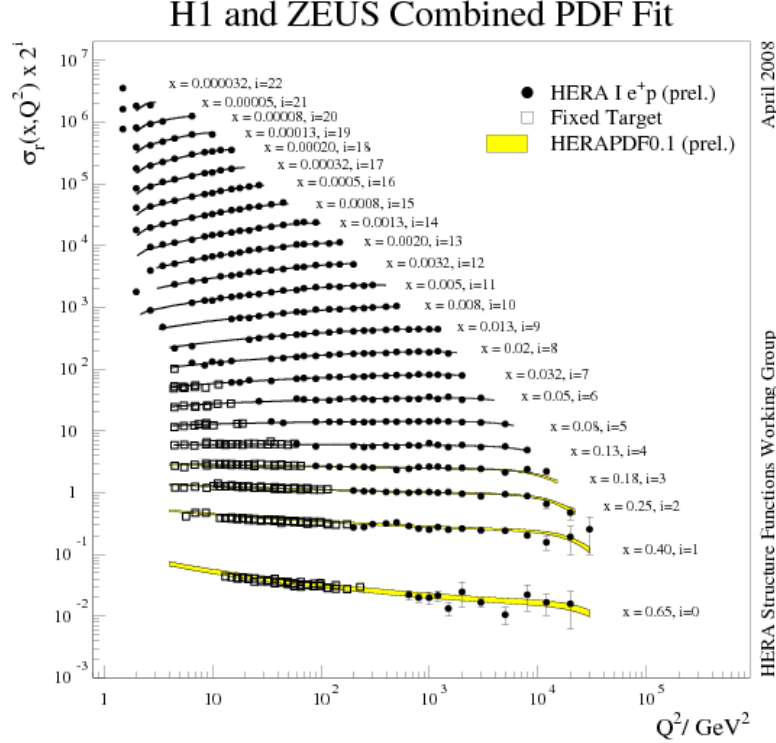


Figure 1.3: Collision cross section as a function of Bjorken- x , with data compared to HERA-PDF calculations [26].

At the small scales probed by high energy photons, the decreasing QCD coupling causes quarks and gluons to interact weakly. This phenomena is called "asymptotic freedom". Because gluons

themselves carry color charge, the gluons about a quark tend to have an anti-screening behavior: the gluon color adds to the quark color, increasing the net color charge of the area. At smaller distances to a quark, then, there are fewer and fewer gluons augmenting the color interaction.

1.5 PDFs

QCD describes the interaction between quarks and gluons, but within a nucleon the calculations are too complicated to solve for the behavior of each individual parton. Theorists employ the factorisation theorem to use data from DIS experiments to make predictions. The factorisation theorem is discussed in greater detail later in section 2.3. Parton distribution functions (PDFs) are a method of encoding data from DIS experiments in the form of probability density. PDFs give the probability of finding a species of parton with given momentum fraction, x , and a given squared energy scale, Q^2 [27][28][29][30].

In electron-proton deep inelastic scattering, the electron interacts with the proton electromagnetically by the emission of a virtual photon. This virtual photon has a four momentum q and a virtuality $Q^2 = -q^2$. When virtuality is low, the virtual photon is approximately "real"; these quasi-photons are discussed in greater detail in chapter 2. The virtual photon, originating from the electron, interacts with a parton and changes its initial momentum fraction, x . The Q^2 of the probing virtual photon and Bjorken-x of interacting parton are determined from the collision products. The data can be used to fill out a probability density, $F_i(x, Q^2)$, of finding a parton species i at a given momentum fraction x with a probe of virtuality Q^2 .

The HERA results show that the parton density rapidly increases as the momentum fraction decreases. Conservation of momentum demands that the splintering of partons must eventually cease. The specific saturation point, where recombination begins dominates, is a characteristic of high energy gluons within a hadron.

[[31] [32]] Figure 1.4 shows an illustration of how the nucleus appears at varying momentum fractions.

The quantum field theory lagrangian of the strong interaction is relatively simple, but because

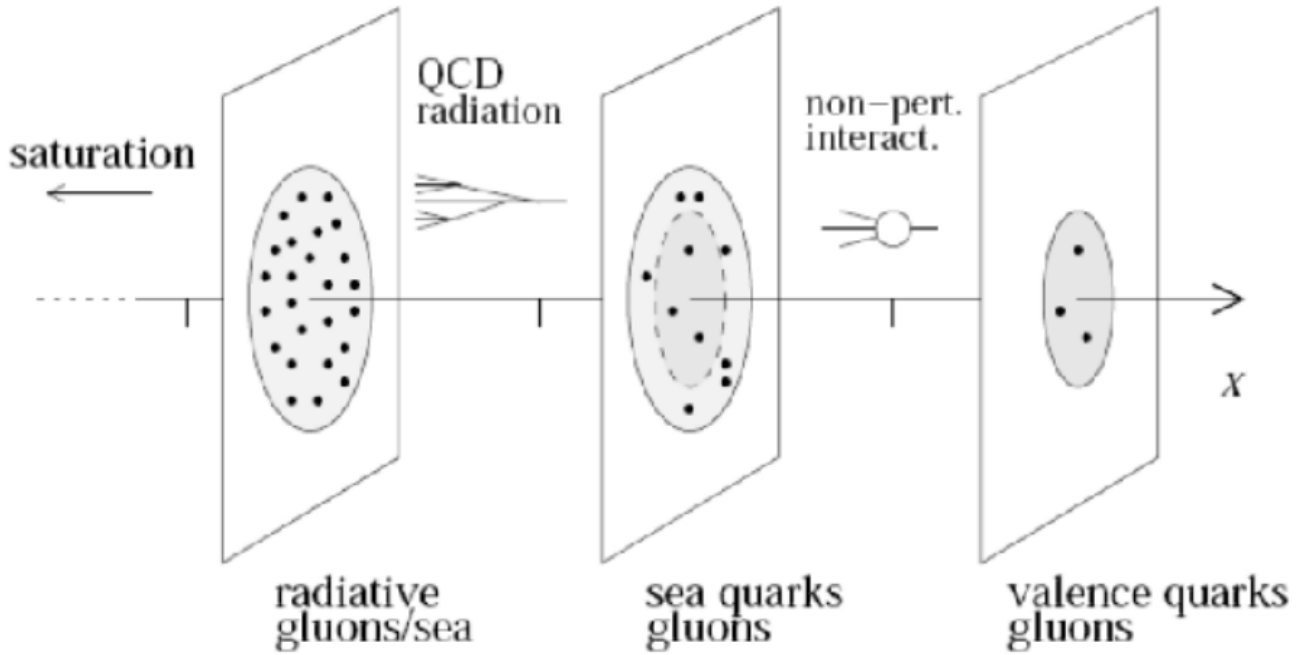


Figure 1.4: Subnuclear tomography (Ask Daniel again) .

of confinement and asymptotic freedom the hadronic bound states are too complex for an analytic solution. Furthermore, collider experiment data requires a quantitative interpretation to be useful. The gap between QCD and heavy-ion data is bridged using the parton model, which considers hadrons as composed of quarks and gluons. Parton density functions (PDFs) model the longitudinal momentum distribution of the partons. PDFs are supplemented by transverse momentum distributions (TMDs) and generalized parton distributions (GPDs). In addition to transverse momentum, GPDs describe the transverse spatial distribution. TMDs and GPDs are derived from the final state particles of a collision. Markus Diehl maps the relationship between various distribution functions in figure 1.13 [33].

1.6 Quark gluon plasma

From 1980's to 2000's, the Super Proton Synchrotron (SPS) and the Relativistic Heavy Ion Collider (RHIC) performed heavy ion experiments to study the possibility of deconfined plasma in a

high parton density medium [34][35][36]. These experiments confirmed the developing model of the QCD phase space; see Figure 1.5 [37]. Essentially, quark matter organizes itself differently depending on temperature and baryon density. At low energies, quark matter exists in bound states: the hadrons. However, in the high energy limit, quarks and gluons take the form of a strongly interacting plasma: QGP. The QGP represents the extreme case of asymptotic freedom; the QCD coupling constant becomes small enough that quarks and gluons no longer behave as bound states. There are two ways of achieving the high energies necessary to form QGP. High baryon densities cause the quarks of separate hadrons to interact at small distances where asymptotic freedom takes effect. It is not currently possible to achieve these densities in laboratory experiments, though this state is thought to occur in neutron stars. By contrast, particle colliders like the LHC increase the energy density by colliding heavy-ions at ultra-relativistic velocities. The high temperature environment produces QGP. The early universe, mere milliseconds after the Big Bang, is thought to have existed as QGP [38].

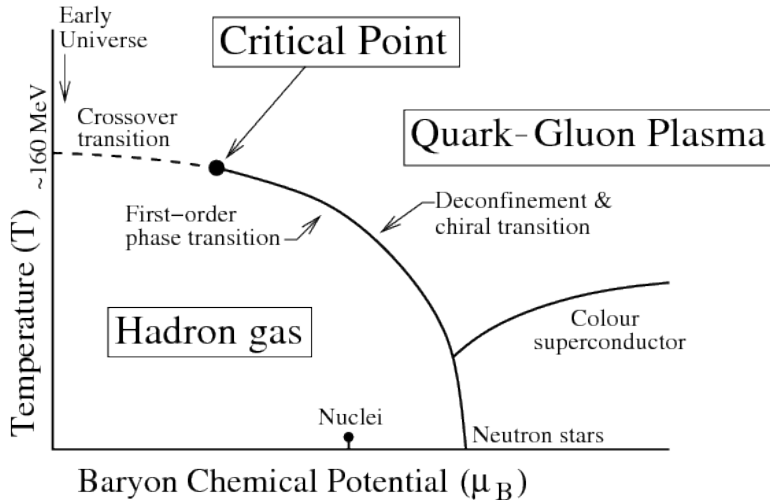


Figure 1.5: QCD phase diagram showing the temperature T as a function of baryon chemical potential μ_B . Different phases such as the critical point, QGP, and hadron gas are seen [37].

There are a number of experimental signatures of QGP formation. Thermal physics understands phase transitions as occurring at specific temperatures and densities. At the boundary between two phases, one can define a critical point at which there is a seemingly discontinuous change in the behavior of observables. For the SPS and RHIC heavy-ion program the main ob-

servables were charm suppression and strangeness enhancement, elliptic flow, and jet quenching [39][40][41].

The QGP is thought to suppression the production of J/Ψ mesons in heavy-ion collisions. Figure 1.6 shows the suppression of J/Ψ with respect to Drell-Yan scattering in Pb-Pb collisions at SPS [34].

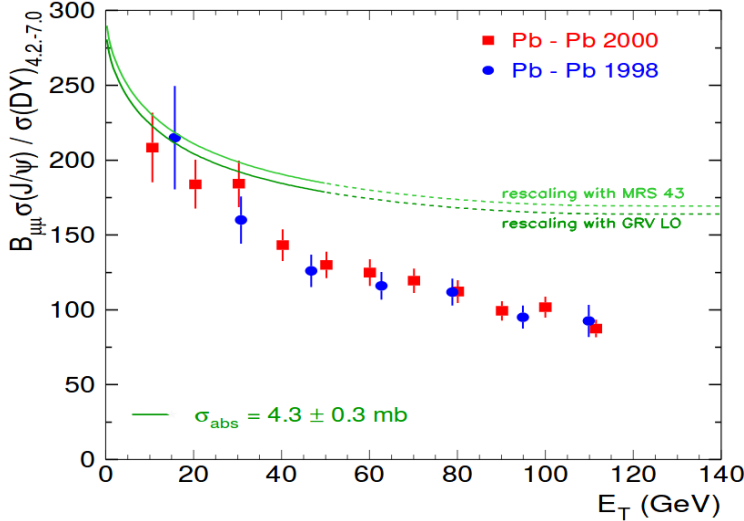


Figure 1.6: J/Ψ suppression in Pb-Pb collisions [34]

The predicted viscosity of QGP would cause elliptic flow in the overlap region of heavy-ion collisions [42]. At RHIC, it was demonstrated that heavy-ion collisions can produce a medium that exhibits elliptic flow. The angular correlations of the final state particles, produced by heavy-ion collisions, were analyzed and shown to be consistent with the medium flowing as a nearly ideal fluid [43]. "Ideal fluid" refers to how the high temperature nuclear medium can be modelled by hydrodynamic equations in which the shear viscosity is extremely low [44]. Viscosity is a measure of how readily a medium converts kinetic energy into thermal energy. For example, when highly viscous material like honey is struck with projectiles, almost all of the kinetic energy of the projectile will be converted into thermal energy within the honey, with only slight deformations, i.e. "splashes", to the honey's volume.

In so far as the QGP is a perfect medium, the initial state properties of the heavy-ion will propagate through the collision and have a significant effect on the final state particles. The angular

distribution of final state particles can be modelled using Fourier series,

$$1 + \sum_{n=1}^{\infty} 2v_n \cos[n(\phi - \Psi)], \quad (1.7)$$

where n is the order of the Fourier expansion, v_n is the Fourier coefficient, ϕ is the azimuthal angle, and Ψ is the event-plane angle. The 2nd order term, v_2 , is referred to as "elliptic flow" and is predicted to quantify the pressure gradient of the overlap-region in the heavy-ion collision. The over-lap region is an ellipse, with a long axis and a short axis. Figure 1.7 is an illustration of the overlap region of a heavy-ion collision. Because the pressure gradient is higher for the short axis than for the long axis, the nuclear medium in the overlap region will flow outward along the short axis, and this is reflected in the alignment of the tracks in the direction of the flow [45][46][47][48][49][50][51].

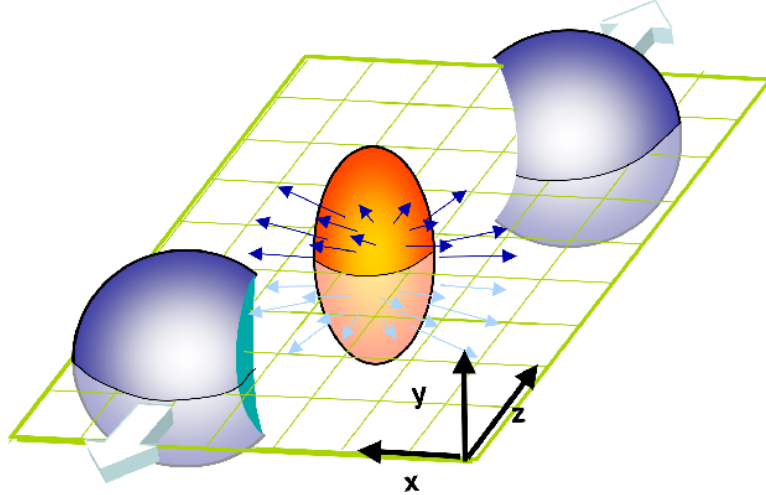


Figure 1.7: Heavy-ion collision overlap region

The viscosity of the nuclear medium directly affects how the initial properties of the overlap region affect the elliptic flow. A highly viscous medium will resist deformation such that the shape of the overlap region, i.e. its ellipticity, will not necessarily carry over to the final-state tracks. However, because the QGP medium is a nearly ideal liquid, the elliptic correlation of the final-state should arise from that of the initial-state. The RHIC result emphasizes the great importance of a precisely understood heavy-ion initial state. Figure 1.8 compares the v_2 elliptic flow results from various heavy-ion experiments [34].

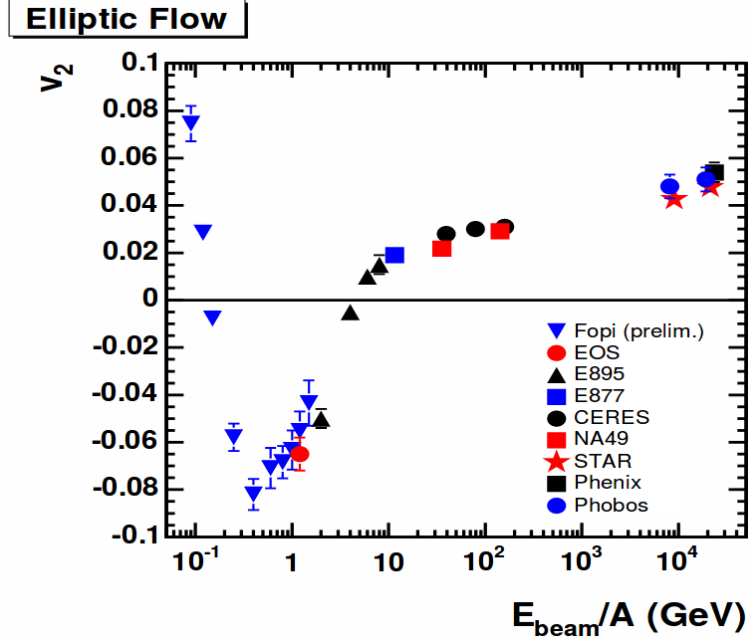


Figure 1.8: v_2 vs collision energy [34]

Figure 1.9 shows results from $\sqrt{s_{NN}} = 130$ GeV $Au + Au$ collisions. The hydrodynamic limit is thought to describe the behavior of QGP. At lower centrality the hydrodynamic limit is in good agreement with data, but the overestimation of data at high centrality is consistent with the rapid thermalization of QGP shortly after collision. The linear p_T dependence of elliptic flow implies that the expansion is enhanced in the collision plane [?].

Figure 1.10 displays one of the most striking phenomena associated with heavy-ion flow: "the

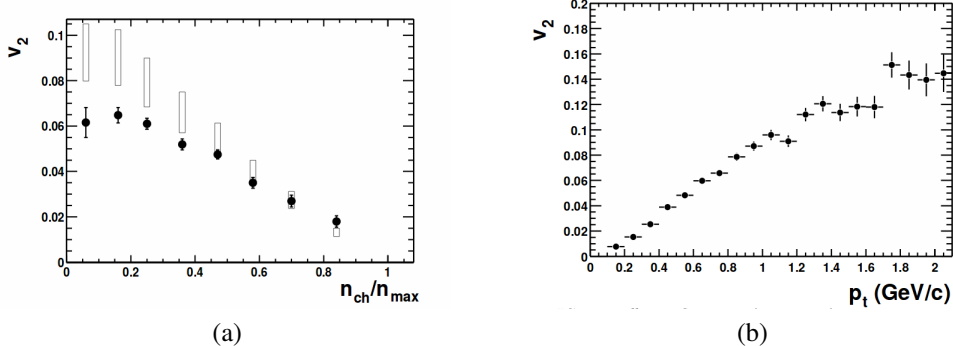


Figure 1.9: STAR $Au + Au$ at $\sqrt{s_{NN}} = 130$ GeV: (a) v_2 as a function of centrality with hydrodynamic calculations (empty rectangles) and data (black dots); (b) v_2 as a function of p_T [50].

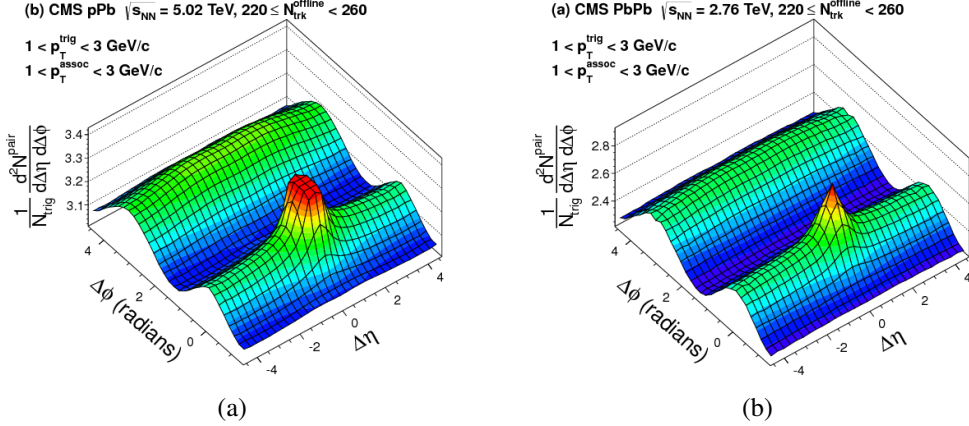


Figure 1.10: CMS (a) pPb and (b) PbPb, angular correlations [43]

Ridge". There is a distinct pattern to the two-particle correlations of high p_T tracks in heavy-ion collisions. Notice that compared to pPb data the PbPb ridge is narrower, implying a stronger correlation and more pronounced elliptic flow [43].

The QGP is particularly interesting because of its implications for the early universe. Figure 1.11 is a simplified cosmological timeline. In the first hundred or so microseconds after the Big Bang, the universe was small, dense, and highly energetic [52]. The energy density of the early universe would have been in excess of $1 \text{ GeV}/(\text{fm})^3$. Note that $1 \text{ GeV}/(\text{fm})^3$ is the energy density at which QGP is thought to form. The universe cools and hadrons form out of the quarks and gluons. The protons and neutrons condense into nuclei. The positively charged nuclei gather negatively charged electrons, forming the atoms that in cosmic time become stars [53]. The progression from a hot, dense medium to stable hadrons is also seen in heavy-ion collisions, as illustrated by figure 1.12 [54]. The y-axis represents time, and the x-axis represents the longitudinal separation of the ions. Notice that after the ions cross, there is a "cascade" during which the partons take on thermal energy until reaching a critical temperature for QGP formation. The hadron gas passes through two temperature "freeze-out". When particles stop forming the chemical freeze-out temperature. These particles stop exchanging kinetic energy after cooling beyond the "kinetic freeze-out" [55].

Lastly, hadronic jets would interact strongly with the QGP; therefore, dijets will have significant energy imbalance depending on the multiple interactions of the components jet with the QGP.

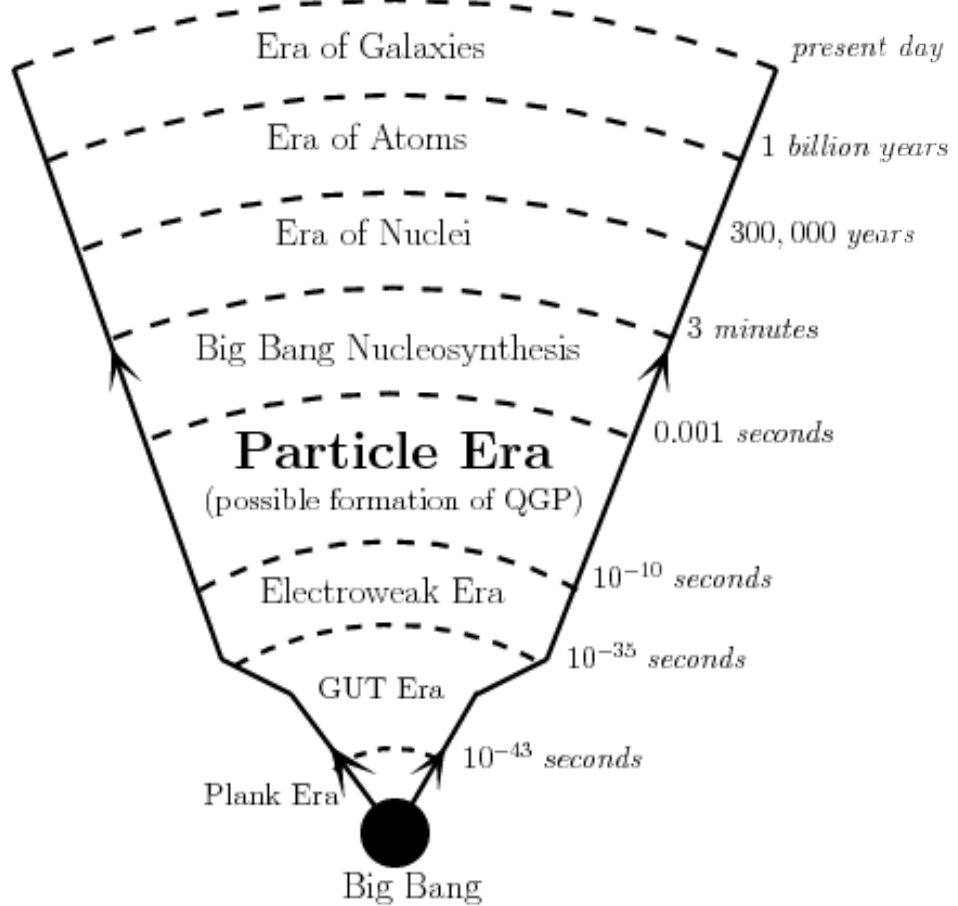


Figure 1.11: Pictorial time-line of the Universe, showing phase transitions [52].

All of these cases require a good understanding the heavy-ion initial state as a basis for comparison [56].

The Large Hadron Collider (LHC) stands at the forefront of high energy nuclear physics research. The LHC is capable of reaching heavy-ion collision energies of up to 7 TeV per nucleon-nucleon, which is sufficient energy for a QGP to be formed and to last long enough to measure its properties [57][58][59].

1.7 Wigner distribution

The Wigner distribution was first developed as part of an attempt by Eugene Wigner to map solutions to Schrodinger equation into phase probability distributions, i.e. a statistical mechanics

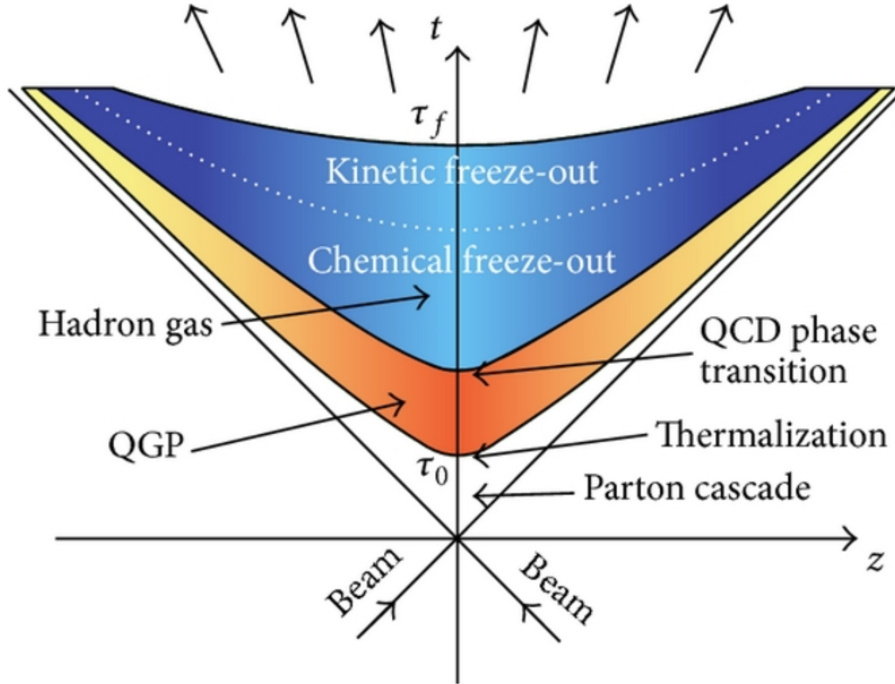


Figure 1.12: Space-time diagram of a heavy-ion collision [54].

interpretation of quantum mechanics.

$$P(x, p) \stackrel{\text{def}}{=} \frac{1}{\pi\hbar} \int_{-\infty}^{\infty} \psi^*(x+y) \psi(x-y) e^{2ipy/\hbar} dy \quad (1.8)$$

The Wigner distribution $P(x, p)$ can be used to calculate the expectation value of any given variable by considering the Wigner transformation $g(x, p)$ of that variable's operator, \hat{G} ,

$$\langle \hat{G} \rangle = \int dx dp P(x, p) g(x, p) . \quad (1.9)$$

Notice that in order to derive expectation values, the probability distribution must be integrated with respect to a function of position or momentum, which are still non-commuting according to the uncertainty principle.

The Wigner distribution is a quantum phase space distribution that describes elliptic gluons [60]. Specifically, by considering the color dipole scattering amplitude, the angular correlation of the nucleon recoil momentum and the dijet transverse momentum can provide a three-dimensional, tomographic image of the gluons within a high energy nucleus. This tomographic image takes the form of a Wigner distribution, which contains all the information of both TMDs and GPDs

without violating the uncertainty principle. Specifically, the angular correlation directly measures the Fourier transform of the gluons. This is possible because the dipole amplitudes are functions of the impact parameter, and because collinear factorization holds.

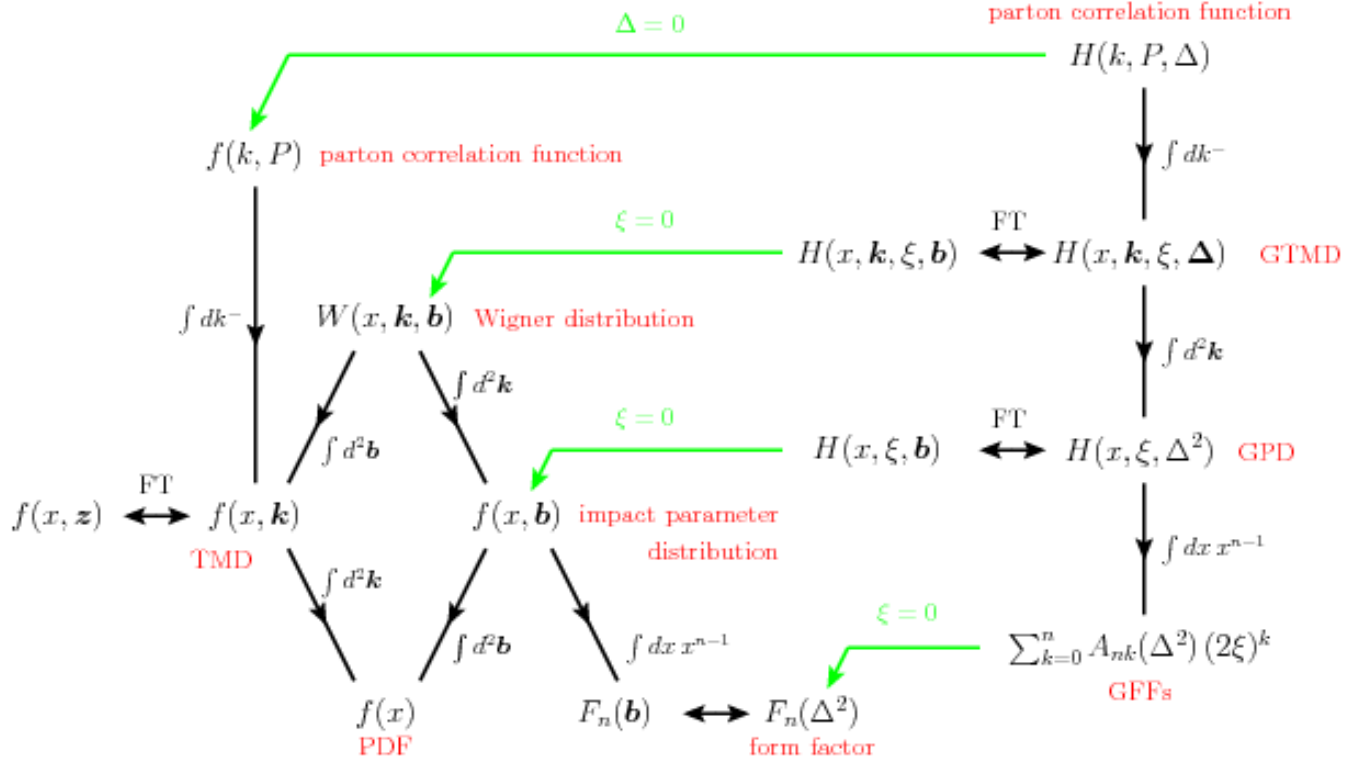


Figure 1.13: Interconnectedness of Parton Distributions [33]

TMDs and GPDs manifest non-perturbative QCD effects. The Wigner distribution, at this scale, reflects the relationship between the position and momentum of partons. Integrating the Wigner function over the transverse distance yields the TMD, while integrating over transverse momentum yields a GPD with spatial information.

Yoshitaka Hatta uses the dipole framework to show that the azimuthal angular correlations of coherent dijets are generated by the underlying Wigner distribution of the small-x gluons. Furthermore, these correlations are consistent with predictions based on standard collinear factorization. Relevant kinematic variables are mapped in the figure 1.14. The diagram shows a virtual photon interacting with a nucleon. k_1 and k_2 are the transverse momenta of the final state jets. These jets originate from a quark-antiquark pair.

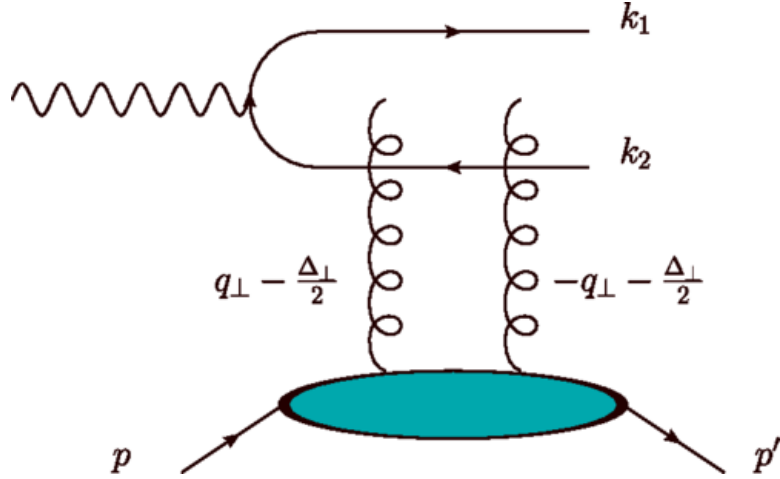
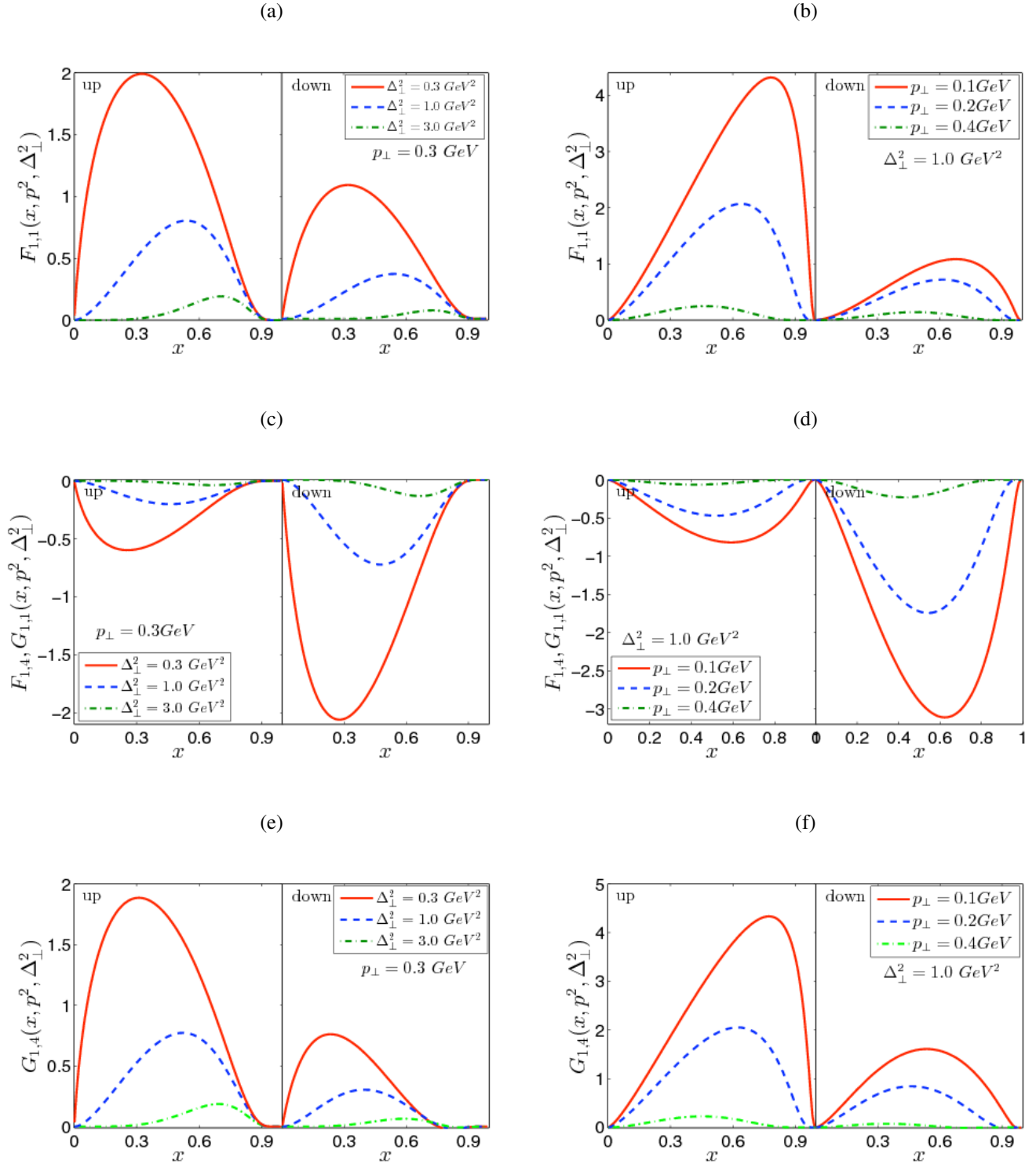


Figure 1.14: Feynman Diagram of Coherent Dijets in Dipole Framework [31]

It is expected that the dominant contribution to the angular correlation is the elliptic, corresponding to $n = 2$ in the Fourier transform [46]. The interior of the proton displays an intricate structure. UPC collisions allow an unprecedented access to the nuclear structure in general and the small- x gluons in particular [61]. Figure ?? shows the theoretical calculation of the elliptic quark distribution - GTMD - for the u and d quarks; notice that for small- x values and large proton recoil, the *GTMD* is enhanced [62].

Figure 1.15: Theoretical Quark GTMDs [62]



Chapter 2

Ultra-peripheral collisions and photoproduction

In this chapter, we will review recent LHC results on ultra-peripheral collisions (UPCs). First we will discuss the unique features of UPCs, and how they are selected. We then present the results from ALICE and CMS on vector meson photoproduction as an example of how UPCs can probe the nuclear gluon distribution. The ATLAS results for light-by-light scattering are also described. The final section explains dijet photoproduction in UPCs, and how the factorisation theorem informs the interpretation of coherent dijet correlation. Finally, we present the physics motivation to study the angular correlation of UPC dijet, which is the analysis presented in this thesis.

2.1 Ultra-peripheral heavy-ion collisions

In classical electrodynamics, all of electrical and magnetic phenomena can be derived from four fundamental equations: Maxwell's laws. Below these equations are given in their differential form.

Gauss's law relates the divergence of a static electric field, \vec{E} , to its source charge density, ρ ,

$$\nabla \cdot \vec{E} = \frac{\rho}{\epsilon_0}, \quad (2.1)$$

where ϵ_0 is permittivity of free space. Gauss's law for a static magnetic field, \vec{B} , reveals the stark contrast between electricity and magnetism. The divergence of a static magnetic field is always a net 0. This reflects the seeming non-existence of magnetic monopoles.

$$\nabla \cdot \vec{B} = 0 \quad (2.2)$$

Faraday's law describes the curl of an electric field in terms of the dynamics of a magnetic field. The electric field and the magnetic field are coupled, and a change in one will affect the properties of the other. For a given electric field, \vec{E} , the curl is equal to the partial derivative of a magnetic

field, \vec{B} , with respect to time, t ,

$$\nabla \times \vec{E} = -\frac{\partial \vec{B}}{\partial t}. \quad (2.3)$$

Ampere's law addresses the curl of a magnetic field, \vec{B} , and once more the absence of magnetic monopoles gives rise to distinct properties. In addition to the partial derivative of \vec{E} with respect to time t , there is a corrective term for the electric charge current density, \vec{J} , and the sum is multiplied by μ_0 , the permeability of free space,

$$\nabla \times \vec{B} = \mu_0 \left(\vec{J} + \epsilon_0 \frac{\partial \vec{E}}{\partial t} \right). \quad (2.4)$$

The complementarity of the classical electric and magnetic fields gives rise to the photon flux so important for ultra-peripheral collisions, and will be discussed in greater detail in the next chapter [63].

Ultra-peripheral collisions occur at impact parameters greater than the sum of the heavy-ion radii. In these collisions, hadronic interactions are strongly suppressed while photonuclear activity is enhanced proportional to the square of the nuclear charge [5]. The electromagnetic field of an incoming heavy-ion, from the perspective of a target, is equivalent to a flux of virtual photons; Figure 2.1 illustrates the Lorentz contraction of the field of a boosted charge [64][65].

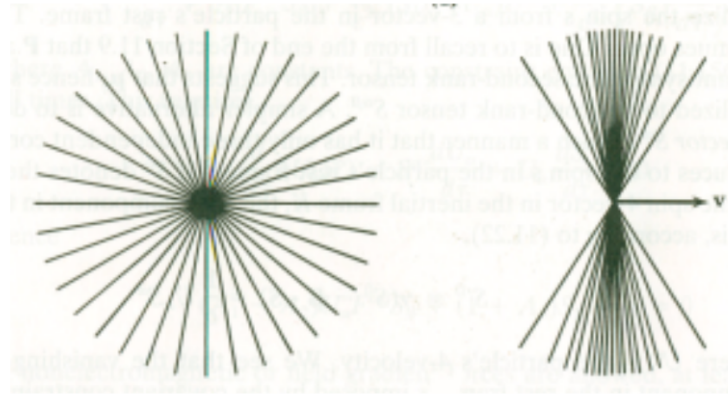


Figure 2.1: (a.) electromagnetic field of stationary charge (b.) eletromagnetic field of boosted charge [65]

UPC models typically address two elements: the photon flux, $N_{\gamma/Pb}$, and the photoproduction cross-section, $\sigma_{\gamma Pb}$. These quantities are related to the UPC cross-section, σ_{PbPb} , in the following

equation

$$\frac{d\sigma_{PbPb}}{dy} = N_{\gamma/Pb}(y, M)\sigma_{\gamma Pb}(y) + N_{\gamma/Pb}(-y, M)\sigma_{\gamma Pb}(-y), \quad (2.5)$$

where there are two terms to reflect that either heavy-ion can be a source of photons [66].

The Weizsacker-Williams appoximation (WWA) calculates the density of photons, about the nucleus, as a function of energy. WWA is a semi-classical formulation. Maxwell's equations are solved for a stationary point charge boosted to an ultra-relativistic velocity. In the target's frame, the Fourier transform of the source field is taken [67]. The Fourier frequency modes are interpreted through the quantum mechanical equation of photon energy. The photon flux as function of energy is given by

$$N(\omega, b) = \frac{\alpha}{\hbar\omega} \left(\frac{Z}{b\beta\pi} \right)^2 \left(\frac{\omega b}{\gamma v} \right) K_1^2 \left(\frac{\omega b}{\gamma v} \right), \quad (2.6)$$

where α is the QED coupling constant, ω is the photon energy, Z is the atomic number of the nuclei, b is the impact parameter, β is ratio of the nuclei speed to the speed of light, γ is the Lorentz boost of the nuclei, K_1^2 is a Bessel function, v is the photon frequency [65].

There are ways to represent the photon flux as solely a function of photon wavelength:

$$n(k) = \frac{2\alpha Z^2}{\pi} \left[\xi K_0(\xi) - \frac{\xi^2}{Z} (K_1^2(\xi) - K_0^2(\xi)) \right] \quad (2.7)$$

Gluons are the particle exchanged in strong interactions. However, gluons themselves carry color charge. By analogy, photons transmit the electromagnetic force, but do not themselves have an electric charge. The gluons are spin-1, meaning that more than one can occupy the same quantum state [68].

The photoproduction cross-section is proportional to the gluon distribution. At low momentum transfer, photons interact electromagnetically, i.e. directly, with partons [69]. High energy, "resolved" photons possess a hadronic structure; instead of directly interacting with the nuclei, these photons fluctuate into mediating quark-antiquark pairs.

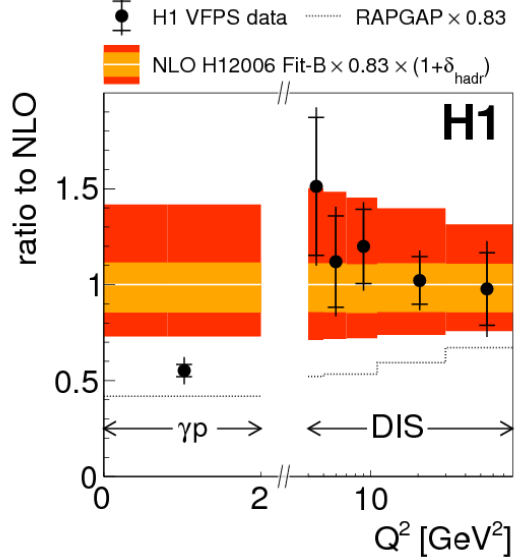


Figure 2.2: Ratio of H1 data cross-section to NLO-QCD cross-section [70]

2.2 Vector meson photoproduction

The vector mesons are a subset of the mesons that have spin-1 and negative parity. There are three vector mesons that are particularly interesting for UPC studies: the ρ^o , the J/Ψ , and the $\Upsilon(1s)$. The ρ^o is an antisymmetric superposition of, up and down, quark-antiquark pairs, $(1/\sqrt{2})(u\bar{u} - b\bar{b})$. The J/Ψ consists of a charm quark and a charm antiquark. The $\Upsilon(1s)$ consists of a bottom quark and a bottom antiquark. J/Ψ and its excited states are referred to as charmonia; likewise, $\Upsilon(1s)$ and its excited states are referred to as bottomonia.

The Bjorken x probed by a specific UPC vector meson is set by the mass M , the rapidity y , and collision energy \sqrt{s} , such that

$$x = \frac{M_{J/\Psi}}{\sqrt{s}} e^{\pm y}. \quad (2.8)$$

The vector meson mass also sets the hard scale, Q^2 , of the photoproduction,

$$Q^2 \frac{M_{J/\Psi}}{4}. \quad (2.9)$$

The virtual photons present in UPC can fluctuate into a quark-antiquark pair which can take the form of a low mass meson [71][72][73]. This meson then interacts with the target nuclei via colorless gluon exchange, emitting a vector meson [74] [75] [76][77]. If the virtual photon inter-

acts coherently with the target nucleus, this is reflected in the transverse momentum of the vector meson [78]. The vector meson decays into a dilepton pair detectable by CMS [79][80][81][82]. STARLIGHT is a Monte Carlo generator designed to model vector meson photoproduction in UPC [83].

For a given final state X , the collision cross section is given as

$$\sigma_X = \int d\omega \frac{n(\omega)}{\omega} \sigma_X^\gamma(\omega), \quad (2.10)$$

where $n(\omega)$ is the number of photons emitted at an energy ω , and $\sigma_X^\gamma(\omega)$ is the photonuclear cross-section of the photon-nucleon interaction. The Weizacker-Williams approximation provides $n(\omega)$. The integral reflects how a state X can result from the interaction of a quasi-real photon of varying energy [84].

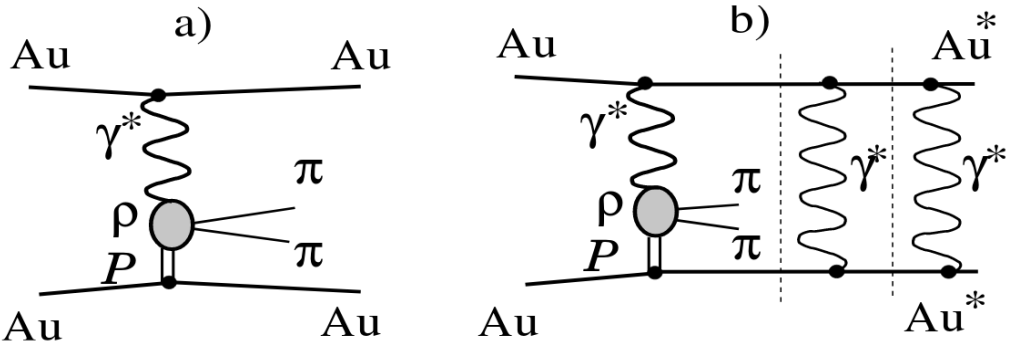


Figure 2.3: $AuAu \rightarrow AuAu\rho^o$, (a.) UPC exclusive ρ^o diagram, (b.) with mutual nuclei excitation [85]

One of the first observations of vector meson photoproduction in UPC was that of exclusive coherent ρ^o production at STAR. For this process the source nuclei emits a virtual photon that fluctuates into a ρ^o meson that scatters elastically off the target nuclei. The ρ^o decays into a pair of oppositely charged dimuons. These dimuons leave two back to back tracks in the STAR tracker. The Feynman diagrams for the process are seen in figure 2.3. In exclusive production there are only two tracks in the tracker, with the rest of the detector being empty. In mutual nuclei excitation, the further exchange of virtual photons excite both nuclei and produce tracks in addition to those of the dimuon. The exclusive events are selected using a low-multiplicity trigger, while the mutual excitation events are selected using a minimum bias trigger with the additional requirement of

neutron emission detected in both of STAR's ZDC [85].

One of the key signatures of UPC coherent ρ , and UPC coherent mesons in general, is the low- p_T peak. If the virtual photon has energy on the order of $1/2R_A$, where R_A is the radius of the nuclei, the photon couples with the whole nucleus. The low momentum corresponds to large wavelength of the photon with respect to the nuclear radius [86][87][88][89]. The p_T spectrum of the ρ detected by the topology and minimum-bias triggers are shown in figure 2.4.

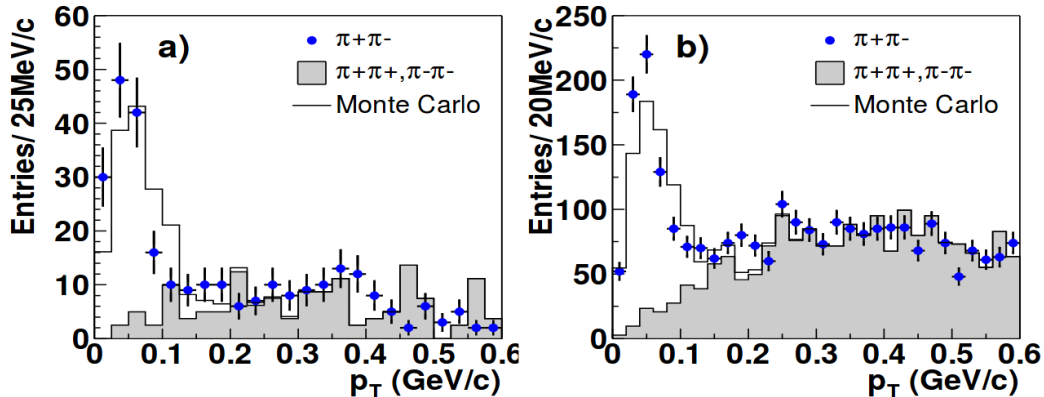


Figure 2.4: UPC exclusive ρ^0 p_T , (a.) topology triggered (b.) minimum bias triggered [85]

Ultra-peripheral coherent J/Ψ photoproduction was studied in the ALICE 2011 Pb-Pb data [90]. Notice that the cross-section of coherent J/Ψ photoproduction, for $\gamma + p \rightarrow J/\Psi + p$, has a power-law dependence on the photon-proton center-of-mass energy, as seen in figure 2.5 [91]. This data can be used to measure the gluon distribution as a function of Bjorken-x [92].

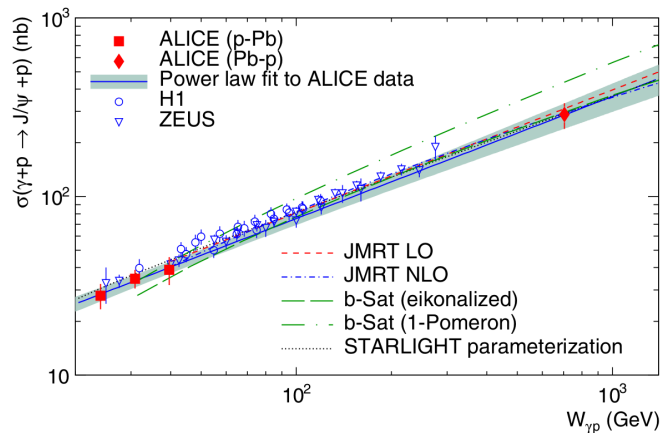


Figure 2.5: $\gamma + \text{proton} \rightarrow J/\Psi + \text{proton}$ cross-section [91].

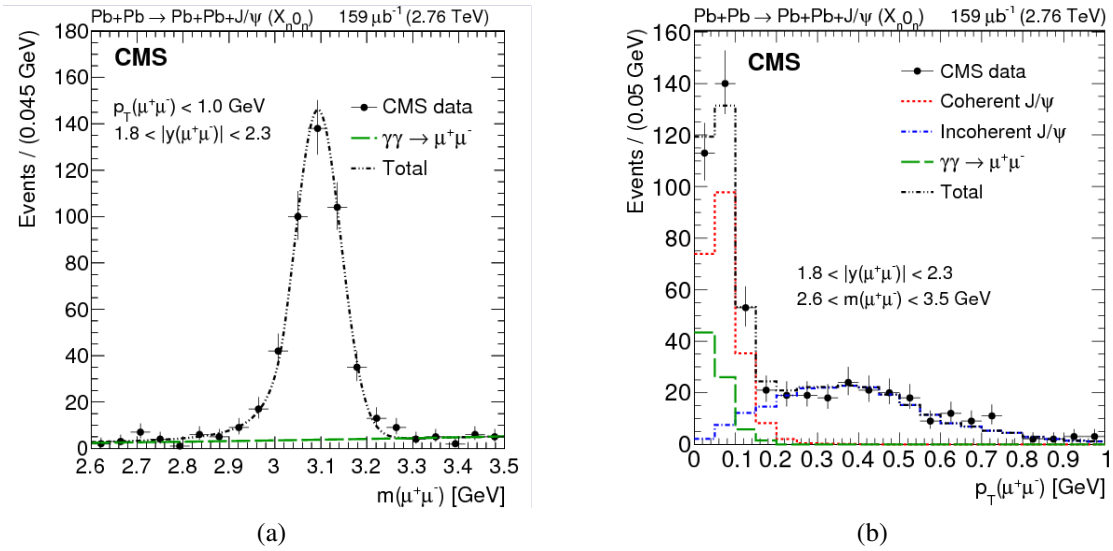


Figure 2.6: (a) dimuon invariant mass spectrum, (b) dimuon p_T spectrum [94].

CMS and ALICE have studied J/ψ and ρ^0 photoproduction off the proton in proton-Pb collisions [93]. In coherent UPC photoproduction of J/Ψ , the transverse momentum distribution peaks at about 60 MeV because, for coherent production, the photon energy is inversely proportional to the Pb ion diameter, $1/2R_{Pb}$.

UPC vector mesons are a clean probe of the nuclear initial state [95][96]. The high temperature environment of heavy-ion collisions produces a near viscosity free medium that exhibits collective flow. However, collective flow phenomena are also observed in heavy-ion collisions below the QGP phase transition. A good understanding of the heavy-ion initial state, before the phase transition, is necessary to detect authentic QGP phenomena. UPC productions can probe the initial state because the interaction is purely electromagnetic; hadronic activity is strongly suppressed, excluding the possibility of QGP forming [97][98].

The UPC J/Ψ in particular is sensitive to the gluon distribution at low Bjorken-x [99]. The UPC J/Ψ photoproduction cross-section can be calculated from a Glauber model of the heavy-ion [100]. The Glauber model approach depicts the nucleus as a sum of protons and neutrons by scaling up the photon-nuclear cross section derived from electron-proton collisions [101]. Forward neutron tagging was used to separate the coherently and incoherently produced J/Ψ [102] [103]

[104][105][106][107][108].

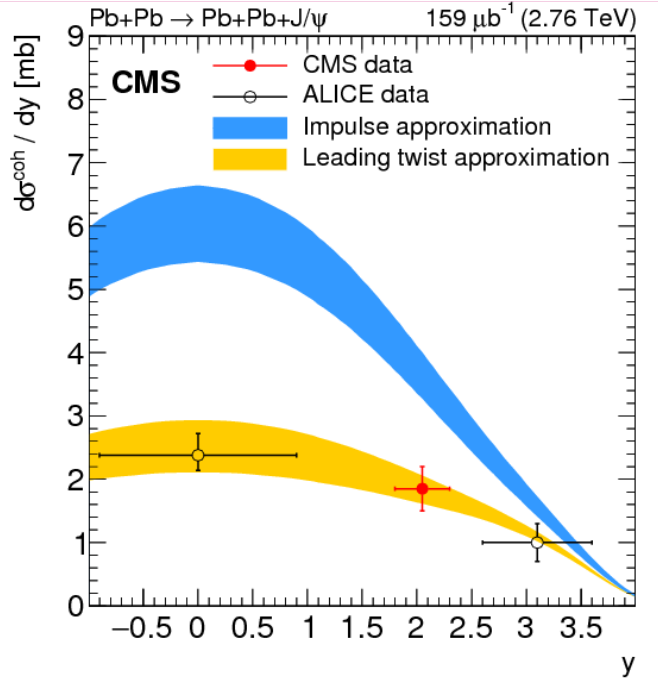


Figure 2.7: Differential cross section versus rapidity for coherent J/Ψ production in ultra-peripheral PbPb collisions at $\sqrt{s_{NN}} = 2.76\text{TeV}$ [94]

Studies of UPC J/Ψ at CMS show that the measured cross section is consistent with models of the nucleus that include moderately strong gluon shadowing, in particular EPSO9 [109][110]. Fig 2.7 compares the cross section measured by CMS and ALICE against theoretical models. In the data there is a clear difference from the Glauber model prediction. The cross sections indicate that, at the energy scale of the J/Ψ mass, the nuclear gluon density is suppressed with respect to that of the proton [111]. Further studies can be done using UPC ν [112][113].

The 2016 proton-ion run allowed CMS to observe Υ photoproduction by using the heavy ion as a photon source.

Studies of UPC J/Ψ at CMS show that the measured cross section is consistent with models of the nucleus that include moderately strong gluon shadowing, in particular EPSO9 [109][110]. Fig 2.7 compares the cross section measured by CMS and ALICE against theoretical models. In the data there is a clear difference from the Glauber model prediction. The cross sections indicate that, at the energy scale of the J/Ψ mass, the nuclear gluon density is suppressed with respect to

that of the proton [111]. Further studies can be done using UPC v [112][113].

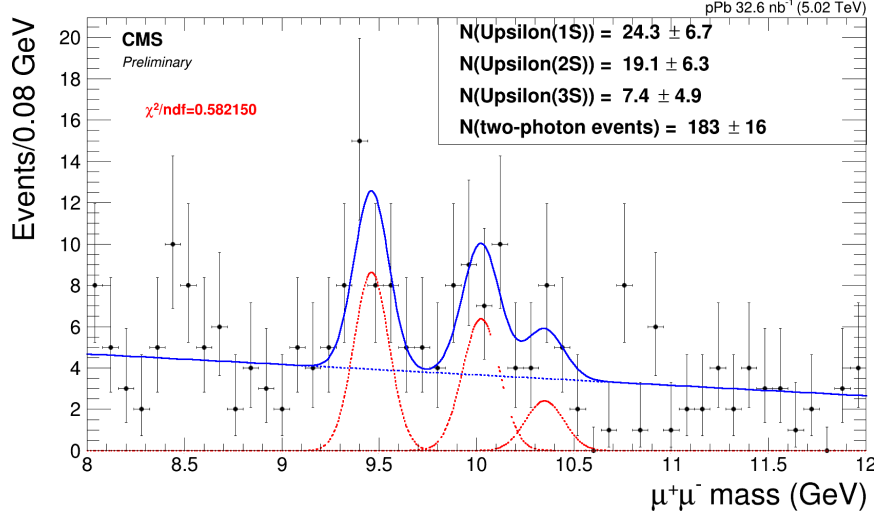


Figure 2.8: Υ photoproduction mass spectrum [114]

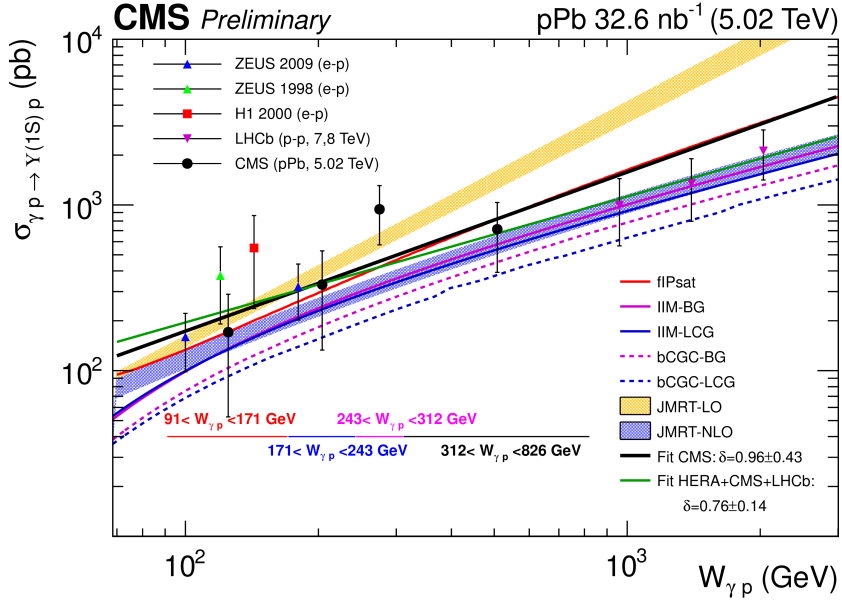


Figure 2.9: $\sigma_{\gamma p} \text{ vs } W_{\gamma p}$ [114]

The 2016 proton-ion run allowed CMS to observe Υ photoproduction by using the heavy ion as a photon source. Figure 2.8 is the mass spectrum of the photoproduced Υ off the proton. Figure 2.9 compares the cross-section of these Υ against the center of mass energy of the γp collision. If this analysis were performed on the PbPb 2015 CMS data, it would be easier to distinguish between the theoretical models of Υ production [114].

2.3 Photon-photon interactions

Classical electrodynamics forbids the scattering of a photon off another photon. According to Maxwell's equations, charge and current distributions make linear contributions to the electric and magnetic fields. For example, the electric field generated by a grid of static charges is the sum of the electric fields of the each charge considered by itself. This property, called "the principle of superposition", allows Maxwell's equations to be solved as boundary values problems via the separation of variables.

The cross section of a final state from the photon-photon interaction is given by

$$\sigma_X = \int d\omega_1 d\omega_2 \frac{n(\omega_1)}{\omega_2} \sigma_X^{\gamma\gamma}(\omega_1, \omega_2), \quad (2.11)$$

where the subscripts 1 and 2 designate the quasi-real photons that are colliding and $\sigma_X^{\gamma\gamma}(\omega_1, \omega_2)$ is the cross-section of the final state from a collision of photons with energies ω_1 and ω_2 . Once more, notice that the total final state cross-section is an integral of the all the photon energies in the photon flux.

Maxwell's equations, being a classical theory, do not take into account the quantum mechanical effects that manifest at the distance scales of sub-atomic particles. The polarization of the vacuum is one such consequence of quantum mechanics. Around a photon there is a cloud of particle-antiparticle pairs, appearing together and then annihilating each other after a time proportional to their energy. In so far as these particles have an electric charge, portions of the local area may carry a non-zero electric charge. Thus, two photons may scatter off each other in three possible exchanges: Diagrams for Delbrück scattering, photon splitting, and elastic light-by-light scattering.

Figure 2.10 illustrates the process of light-by-light scattering. The plots in figure 2.10 (a.) are the Feynman diagrams of the three light-by-light channels: Delbrück scattering, photon splitting, and elastic scattering, respectively. Notice that all three channels are variations on a closed electron-loop. Figure 2.10 (b.) shows how these processes arise in heavy-ion collisions. The photon flux from a relativistic heavy-ion is calculated from the Fourier transform of its electric field. The final state X is empty except for two photons [115].

Light-by-light scattering has been observed at ATLAS. The relevant data sample contains

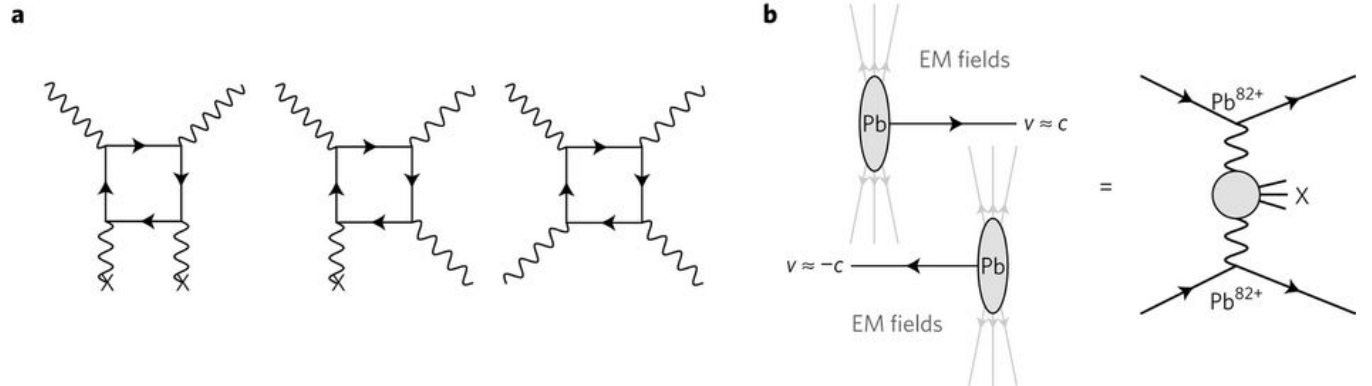


Figure 2.10: $\gamma\gamma$ Diagrams of light-by-light scattering, (a.) channels, (b.) analogous [115]

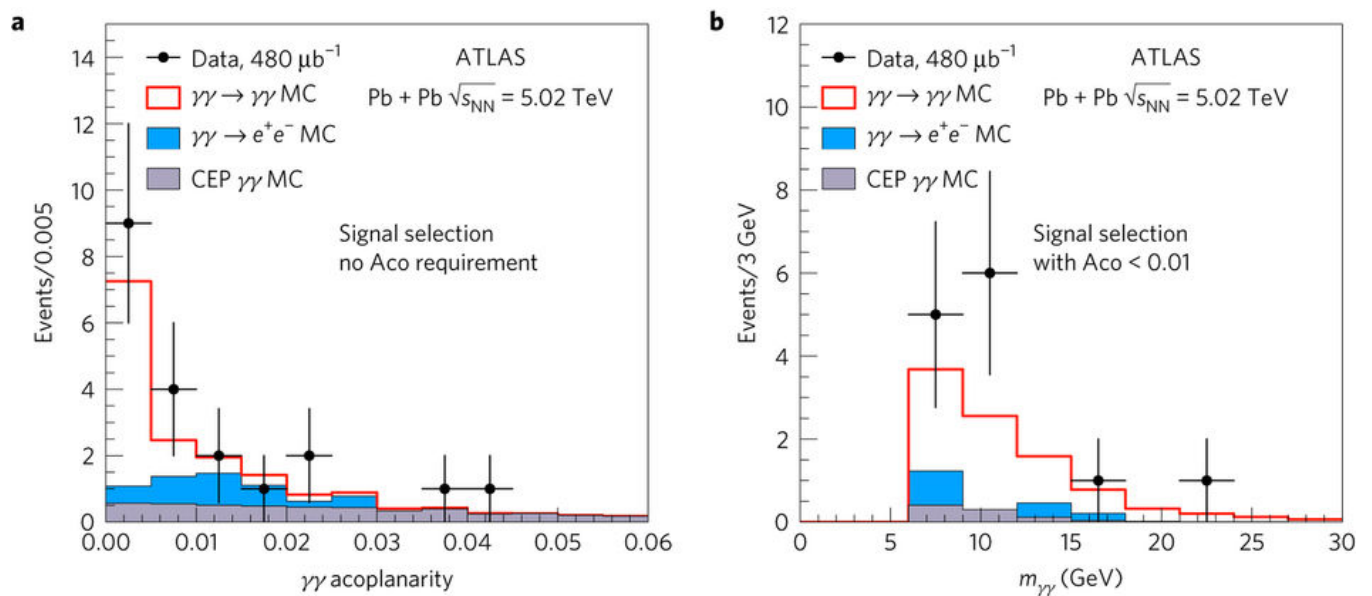


Figure 2.11: $\gamma\gamma$ kinematics, (a.) acoplanarity, (b.) invariant mass [115]

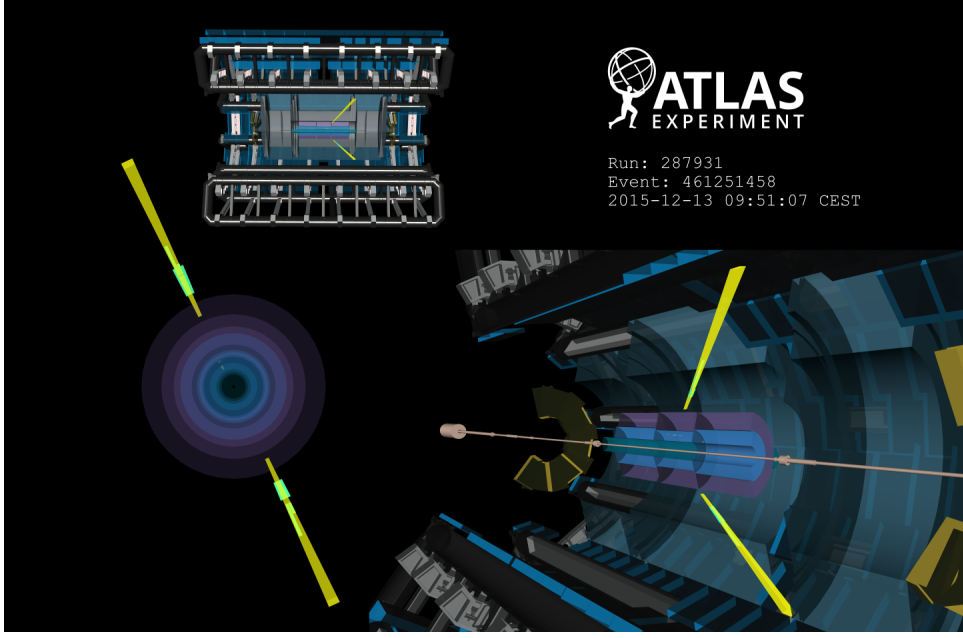


Figure 2.12: Event Display of ATLAS photon-photon scattering [116]

$480 \mu b^{-1}$ of Pb+Pb data taken at $\sqrt{s_{NN}} = 5.02$ TeV. Light-by-light MC was generated using STARLIGHT and processed through a GEANT4 simulation of ATLAS. The reconstructed MC was used to create kinematic templates for comparison against the data. These templates can be seen in figure 2.11. The most important part of the event selection is the cut on diphoton acoplanarity.

Figure 2.12 is an event display for an ATLAS light-by-light candidate [116]. Notice that the two photons are back-to-back in the plane perpendicular to the beam.

2.4 Coherent dijet photoproduction and diffraction

Jets are one of the most interesting nuclear phenomena discovered in the modern era of particle accelerators. The existence of jets is a direct result of QCD confinement. In hadron collisions, it is possible for the hadron's constituent partons to fragment away. These partons, of themselves, would not be colorless. However, QCD confinement – caused by the running QCD coupling – demands that only colorless objects can independently exist. Therefore, as the fragment partons separate, they manifest new partons around themselves and screen the color charge. The forma-

tion of colorless composites, out of colored partons, is called "hadronization". The process of hadronization continues until the kinetic energy of all the fragmented partons drops below the potential energy the binding strong force. The result is a narrow cone of hadrons fanning out from a common source: a "jet". Analyzing a jet can elucidate the properties of its mother parton [117].

An important experimental signature of deconfinement is how it affects hard-scattering processes. In a hard scattering process, partons are fragmented off from the nucleus and, due to confinement, hadronize into a cone of correlated final state particles, known as a jet. In theory, a jet should be sensitive to the medium that the mothering parton passes through. However, in order to detect the modification of a jet due to its mother parton passing through QGP, one needs a precise measurement of the jet production in of nuclear PDFs but not QGP. One can then determine QGP effects by comparison to the nuclear PDF baseline. However, there is a significant lack of data for low- x nuclear PDF. As Bjorken- x decreases, the nuclear PDF passes through stages three stages: EMC effects, anti-shadowing, and shadowing. EMC effects and shadowing are suppressions of the nuclear PDF in comparison to the proton PDF; anti-shadowing, by contrast, is the enhancement of the nuclear PDF in comparison to the proton PDF [118].

The dijet photoproduction cross-section, like that of vector meson photoproduction, displays diffractive dips in its $|t|$ dependence. Furthermore, according to the color glass condensate formalism, coherent dijet production is sensitive to gluon saturation effects at small Bjorken- x values [119][120]. Gluon saturation would affect the color-dipole orientation of nucleons in the transverse plane. This effect should be reflected in an enhanced azimuthal angle correlation of the jets.

QCD factorisation describes the diffractive-photoproduction dijet cross-section as the convolution of the partonic cross-section with the diffractive parton distributions. However, factorisation only describes H1 data if the resolved-photon contribution is suppressed.

Diffractive dijet photoproduction is not describable in perturbative QCD. For coherent processes the photon energy is small, and therefore the wavelength is large compared to the size of the nucleus. At these large distances, there isn't a hard scale, and so perturbation calculations cannot be done. Gluon splitting interactions dominate the low Bjorken- x partons. QCD collinear

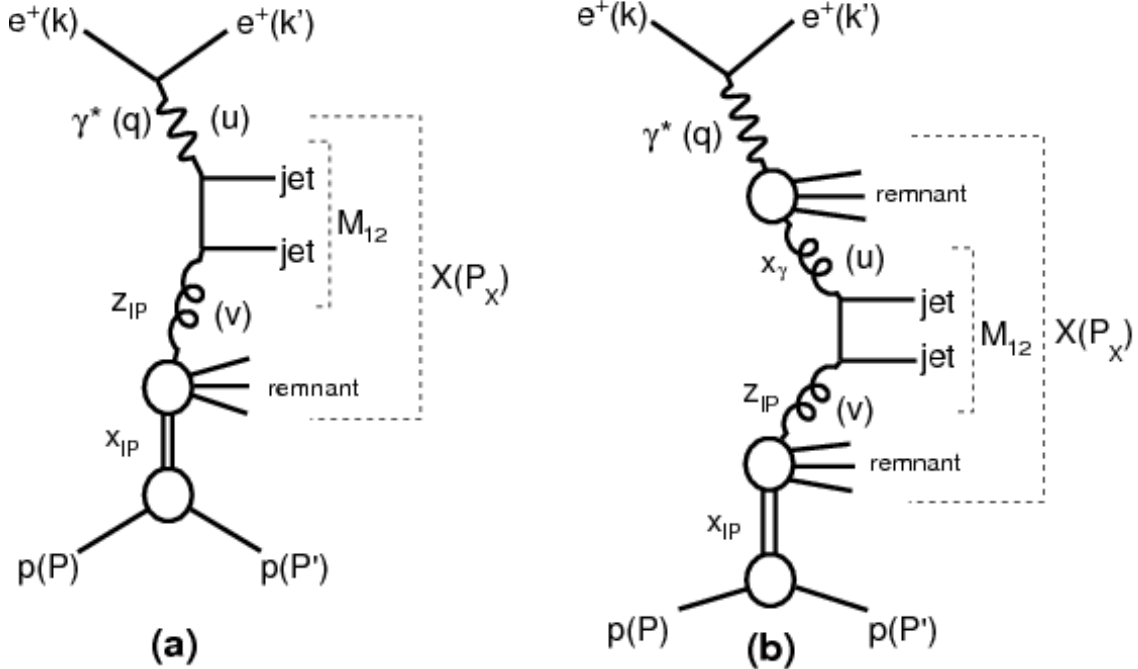


Figure 2.13: Feynman diagrams for coherent jet photoproduction in (a) direct-photon in ep , (b) resolved-photon in ep [70]

factorization describes these soft interactions via the convolution of parton cross sections, taken from perturbative QCD, and diffractive parton distribution functions, taken from experiment [70] [121]. The photon can interact directly with the nucleon, or the photon can fluctuate into a quark-antiquark pair which interacts with the nucleon. The resolved-photon has a hadronic structure and its own corresponding PDF [122].

In electron-hadron collisions, diffractive photoproduction is characterized by the presence of a large rapidity gap in the final state and an intact nucleus [123][124][95]. The Feynman diagram of electroproduction in lepton-hadron collisions is similar to that of photoproduction in ultraperipheral collisions, as seen in figure 2.13 [70]. The large rapidity gap here is due to the leading proton [125]. The diffractive dijet cross section is expressed by the convolution of partonic cross sections $d\hat{\sigma}$ and diffractive PDFs $f_{i/p}^D$.

$$d\sigma(ep \rightarrow e + 2\text{jets} + X' + p) = \sum_i \int dt \int dx_{\mathbb{P}} \int dz_{\mathbb{P}} d\hat{\sigma}_{ei \rightarrow 2\text{jets}}(\hat{s}, \mu_R^2, \mu_F^2) \times f_{i/p}^D(z_{\mathbb{P}}, \mu_F^2, x_{\mathbb{P}}, t), \quad (2.12)$$

where $x_{\mathbb{P}}$ is longitudinal momenetus fraction lost by the incoming proton, $d\hat{\sigma}_{ei \rightarrow 2\text{jets}}$ is the partonic cross-section for the process, $z_{\mathbb{P}}$ is the longitudinal momentum fraction of the pomeron entering the hard process, \hat{s} is the squared invariant energy of the subprocess, μ_R^2 is the squared renormalization scale, μ_F^2 is the squared factorisation scale, $f_{i/p}^D$ is the diffractive parton distribution, and t is the four-momentum transfer squared at the vertex.

In the proton-vertex factorisation hypothesis, the dependence on $x_{\mathbb{P}}$ and $|t|$ is factored out of the dependence on μ_F^2 and $z_{\mathbb{P}}$. Furthermore, $f_{i/p}^D$ is sum of contributions from the pomeron and Reggeon:

$$f_{i/p}^D(z_{\mathbb{P}}, \mu_F^2, x_{\mathbb{P}}, t) = f_{\mathbb{P}/p}(x_{\mathbb{P}}, t)f_{i/\mathbb{P}}(z_{\mathbb{P}}, \mu_F^2) + n_{\mathbb{R}}f_{\mathbb{R}/p}(x_{\mathbb{P}}, t)f_{i/\mathbb{R}}(z_{\mathbb{P}}, \mu_F^2), \quad (2.13)$$

where ${}_{\mathbb{P}/p}$ is the pomeron flux factor, $f_{\mathbb{R}/p}$ is the Reggeon flux factor, $n_{\mathbb{R}}$ is the normalization factor of the Reggeon, $f_{i/\mathbb{P}}$ is the pomeron parton distribution, and $f_{i/\mathbb{R}}$ is the Reggeon parton distribution.

Lepton-hadron collisions were performed at HERA and measured by the H1 experiment. These experiments reported a value for the total diffractive photoproduction cross section that is double that predicted by QCD collinear factorization; figure 2.14 compares the cross-section of H1 data to that predicted by NLO-QCD [70]. Diffractive events were selected for using rapidity gaps or the presence of leading protons in the very forward proton spectrometer (VFPS).

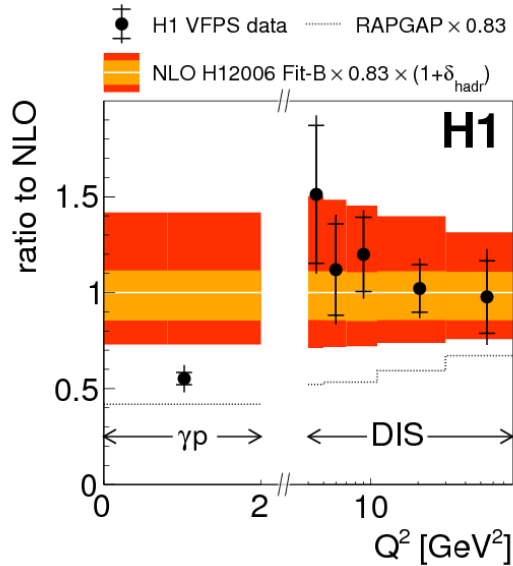


Figure 2.14: Ratio of H1 data cross-section to NLO-QCD cross-section [70]

H1 used the Very Forward Proton Spectrometer (VFPS) to trigger on low Q^2 protons. The VFPS consists of two Roman Pots located 218 m and 222 m from the H1 interaction-point in the forward direction. The VFPS can detect protons scattered at very low transverse momentum, corresponding to $0.008 < x_P < 0.028$ and $|t| < 0.6$. Each of the Roman Pots contains layers of scintillating fibers, which are covered by a layer of scintillator tiles. The fibers readout to photomultipliers, and the tiles both shield from radiation and trigger on protons. The track efficiency of VFPS is a remarkable 96%, and the background contamination is kept at 1% , making the detector excellent for studying diffractive events. Figure 2.15 shows the $|t|$ coverage of the Forward Proton Spectrometer (FPS) and VFPS [70].

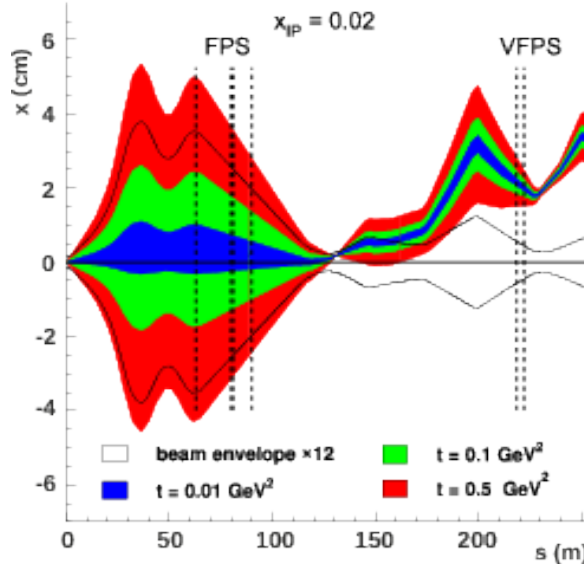


Figure 2.15: Beam envelope vs. distance to vertex in H1 [70]

The H1 data was compared to predictions based on NLO-QCD convoluted with diffractive parton distribution functions (DPDFs) from HERA inclusive diffractive deep-inelastic scattering (DDIS) data. For diffractive pp collisions the high transverse momentum jets yield a hard scale for perturbative QCD [126].

H1 used the RAPGAP MC generator to model diffractive $e + p \rightarrow e + X + p$ processes. The requirement of a leading proton, remaining intact or dissociating into a low energy state, was used to sample diffractive events. The collision product kinematics of data and MC are shown in figure

2.16. Not only is the data in good agreement with predictions from RAPGAP, but the cross section of diffractive $e + p$ scattering is well described by calculations based on DPDFs. For this process, β refers to the fraction of the pomeron's longitudinal momentum transferred to the parton within the nucleus. Figure 2.17 is the diffractive cross section as a function of β [125].

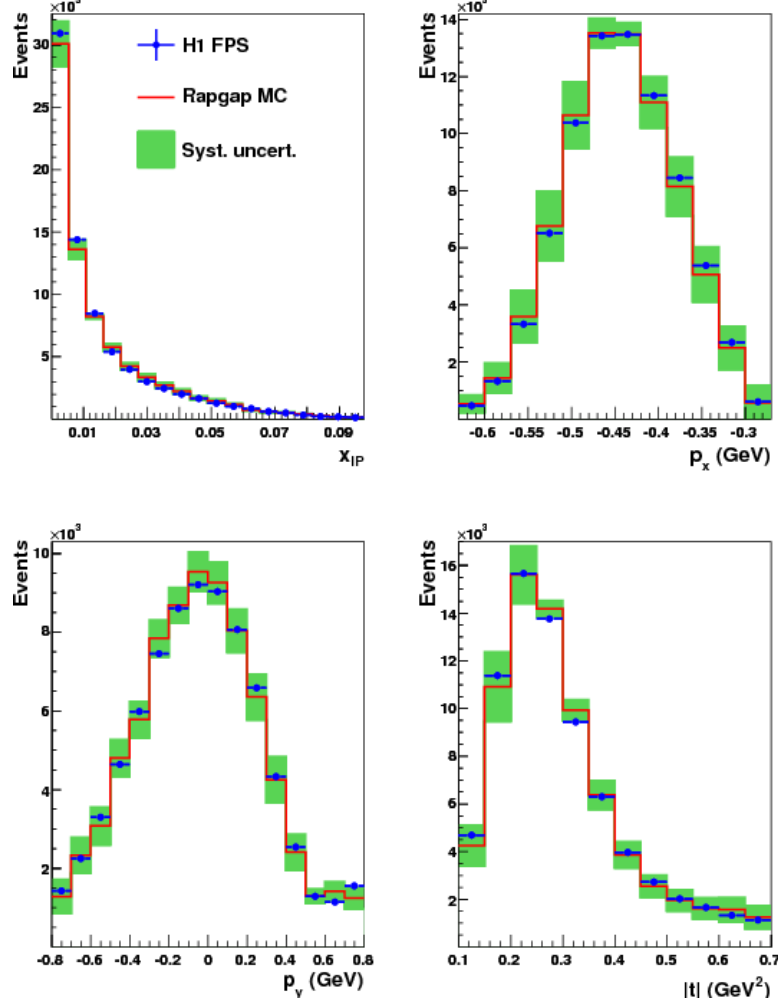


Figure 2.16: H1, Diffractive $e + p$ products, Kinematics [125]

Rapidity gaps are one of the experimental signatures used to select for diffractive events. The ZEUS collaboration, in their diffractive $e + p$ studies, defined a "large rapidity gap" (LRG) sample as having at least two empty units of rapidity in the forward proton spectrometer (FPS). Here "empty" means the FPS detected no physics objects above 400 MeV. Furthermore, the energy deposited in the FPS could not exceed 1 GeV. The data was found to be in good agreement with diffractive MC produced in SATRAP, as seen in figure 2.18 [121].

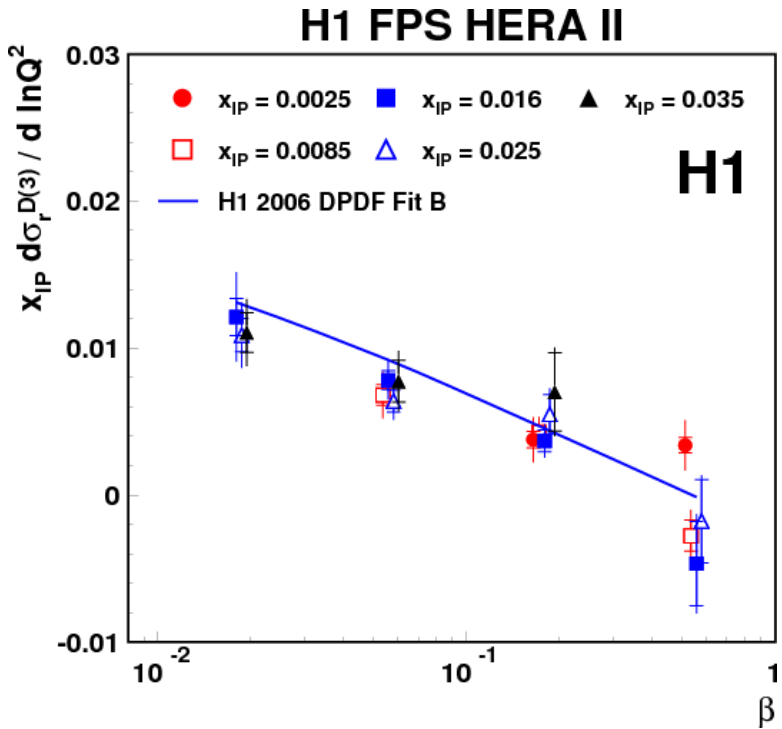


Figure 2.17: H1, Diffractive Dijets, Cross Section [125]

ATLAS has published preliminary results on UPC dijet production. It has been shown that these photonuclear dijets manifest distinct differences from dijets produced in more "hadronic" collisions. There are rapidity gaps that are similar to those seen in the diffractive productions of electron-proton collisions at HERA. The forward neutron emission spectrum also matches that expected for UPC data set. The ATLAS results are particularly interesting because Strikman, Vogt, and White have shown that UPC dijet photoproduction is sensitive to the low Bjorken-x nuclear PDFs.

ATLAS used a combination of triggering, forward calorimetry, and rapidity gap requirements to select events of photo-nuclear dijet production in ultra-peripheral heavy-ion collisions. Figure 2.19 shows the two variations of the leading order diagram for UPC dijet production. On the left is direct photo-production, in which the mediating virtual photon has low enough virtuality to interact with the nucleus as a photon. On the right is resolved photo-production, in which the virtual photon has a high enough virtuality to manifest a hadronic structure, the interaction with the nucleus is mediated by a pomeron [127]. Directly photo-produced final state particles will have a

ZEUS

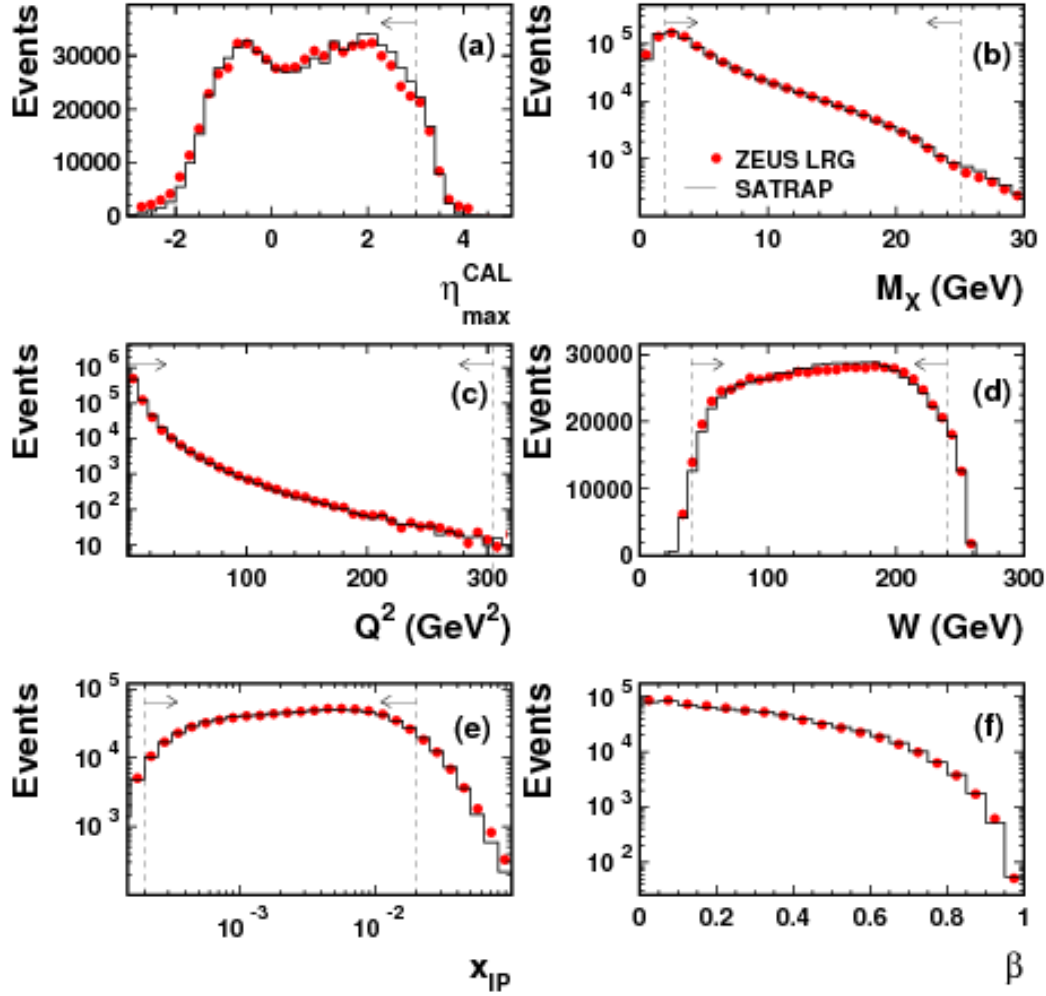


Figure 2.18: ZEUS, Diffractive Dijets, Kinematics [121]

characteristic rapidity gap in the final state because the target nucleus does not dissociate. Resolved photoproduction, however, excites the nucleus such that the rapidity gap is partially filled.

ATLAS reported the cross-section of photo-nuclear dijet production versus various dijet kinematic variables, and compared these cross-sections to those derived from MC. The MC sample was generated by Pythia and re-weighted to fit the quasi-real photon spectrum of a relativistic Pb ion [128]. The photon spectrum itself is taken from the STARLight MC generator [129][83].

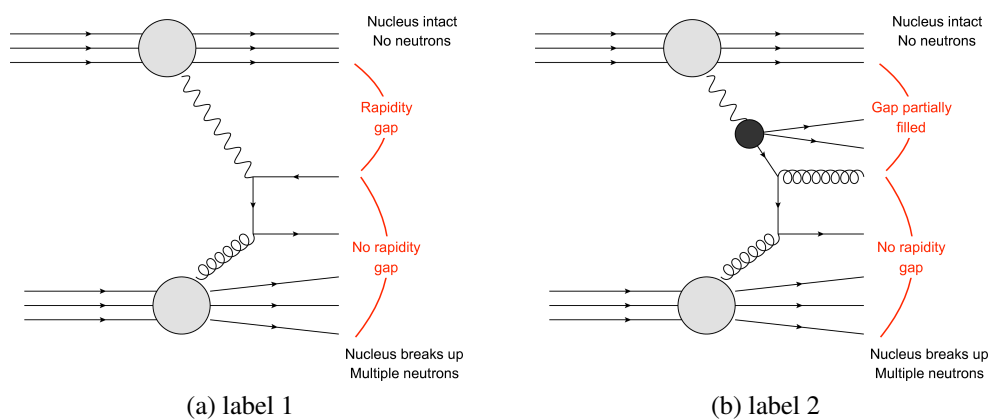


Figure 2.19: ATLAS UPC Dijets, (left) p_T and (right)invariant mass [127]

Chapter 3

The experiment

3.1 Large Hadron Collider

The Large Hadron Collider (LHC) has a radius of approximately 27 kilometers. As of this writing, it is the largest machine ever constructed. The initial purpose of the LHC was to discover the Higgs boson, but it is capable of investigating a variety of other physics phenomena, such as dark matter, extra-dimensions, and heavy-ion physics.

The beams are accelerated along a circular path using radio frequency cavities, gaining energy with each revolution. LHC is a hadron collider, meaning it is designed to collide particles made of quarks and gluons. The proton-proton, proton-Pb, and Pb-Pb collision energies are the largest ever probed experimentally. The LHC is a circular collider [130].

Heavy-ion collisions at LHC produce strongly interacting nuclear matter. The temperature and density of this matter is comparable to the state of the universe only a few milliseconds after the Big Bang.

3.1.1 ATLAS

"ATLAS" stands for "A Toroidal LHC ApparatuS". ATLAS was designed as a general purpose detector for LHC physics. Three toroidal superconducting magnets provide the field for particle identification, in contrast to the titular compact solenoid magnet of CMS. The looser design constraints of the ATLAS magnets allow for a more efficient, stand-alone measurement of muon momentum [131].

3.1.2 ALICE

"ALICE" stands for "A Large Ion Collider Experiment". ALICE, unlike ATLAS and CMS, is not a general purpose detector. ALICE was designed to study a specific phenomena: the quark-gluon plasma posited to exist during ultra-relativistic heavy-ion collisions. The primary design consideration was the correct identification of particle species at high multiplicities. ALICE retains excellent PID at approximately $dN/d\eta = 4000$, and this over a particle momentum range up to 100 GeV. PID is accomplished through a combination of time-of-flight chambers, muon filters, and the analysis of specific ionization energy [132].

3.1.3 LHCb

"LHCb" stands for "Large Hadron Collider beauty", reflecting the LHCb's purpose: b-quark ("beauty") studies. In this respect it is similar to ALICE, LHC's other specialized experiment. By examining CP violation in heavy-quark hadrons, LHCb hopes to elucidate the asymmetry of matter and antimatter. LHCb is asymmetric in the z-axis: b-hadron pairs tend to scatter in the same forward rapidity, so the experiment only covers $1.9 < \eta < 4.9$. A large dipole magnet projects an field in the vertical plane of LHC. Small asymmetries in the transverse scattering of the b-hadron system are used to test for CP violation [133].

3.1.4 TOTEM

"TOTEM" is a sub-experiment located at CMS. TOTEM uses Roman Pots (RPS), placed far forward of CMS, to measure the total proton+proton interaction cross-section. The RPS have high acceptance for the flux very close to the beam. There are two sets of RPS, one on each side of CMS, located approximately 400 meters down the z-axis from the interaction point. The differential cross-section, of proton-proton scattering, grows exponentially with the $|t|$ at low values of $|t|$. More precise measurements of this differential cross section can help distinguish between competing models of proton structure. Furthermore, the total interaction cross-section is an important

benchmark for analyzing cosmic ray showers, and can be used to independently calibrate the beam luminosity measured at other LHC experiments. Diffractive studies at TOTEM complement those at CMS.

3.1.5 CASTOR

CASTOR – Centauro And Strange Object Research – is a calorimeter at CMS covering 5.1 – 6.55 pseudorapidity. The calorimeters are both electromagnetic and hadronic, and located on either side of CMS beyond the hadronic forward calorimeters. CASTOR was designed to detect centauro events. Centauro events are caused by exotic matter produced in heavy-ion collisions. Typical centauro events are low multiplicity and high transverse momentum, on the order of 100 GeV/c, with suppressed electromagnetic activity. There is also the possibility of a very high energy, high penetrating particle in the forward region : the so called "long flying component". Centauro events have already been observed in cosmic-ray experiments, and there are phenomenological models for their production in QGP. [134]

3.2 Compact Muon Solenoid

The Compact Muon Solenoid (CMS) is a general-purpose particle detector located at Point-5 of the LHC. CMS was designed to precisely measure the momentum of muons. The titular superconducting solenoid magnet was designed to generate a 4 Tesla field, but operates at 3.8 T to increase longevity. This field is homogeneous and parallel to the beam line close to the interaction point. The momentum of a muon is measured from how it deflects when moving through the magnetic field [135]. Altogether, CMS weighs approximately 12,500 metric tons, with a diameter of 14.6 m and a length of 21.6 meters. Figure 3.1 displays the detector's various sub-systems [136].

Within the solenoid volume are a silicon pixel and strip tracker, a lead tungsten crystal electromagnetic calorimeter (ECAL), and a brass and scintillator hadron calorimeter (HCAL), each composed of a barrel and two endcap sections. Fig.3.2 radial layering of CMS component systems

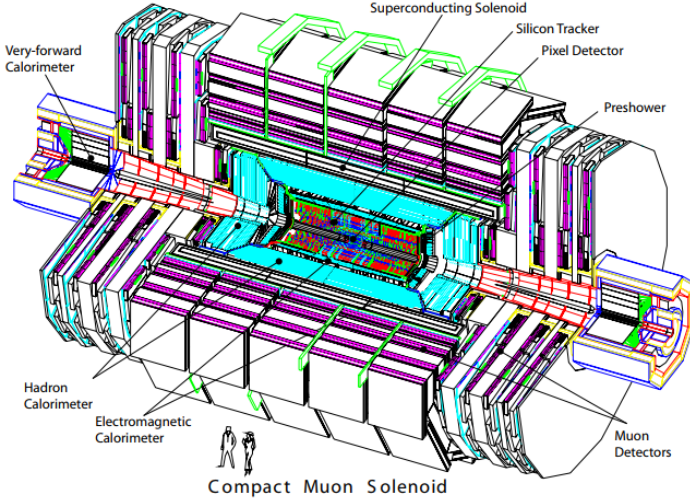


Figure 3.1: CMS Detector [136]

[137].

3.2.1 Tracker

The tracker measures the momentum of charged particles via their trajectory through a homogeneous magnetic field. The tracker consists of two units, the pixel tracker and the strip tracker, both of which are made of silicon. Compared to large-volume gas detectors, which are less expensive, silicon detectors have a faster response time. The number of tracker layers is optimized for the highest penetration by charged particles while minimizing the occurrence of multiple scattering [138].

Multiple scattering reduces the efficiency and resolution of the tracker because of bremsstrahlung. When a charged lepton passes through an electric field, the changes in acceleration will change the energy of lepton. The lepton will release photons that will contaminate the signals read by the tracker.

The high luminosities reached by LHC typically achieve some 20 to 30 collisions per bunch crossing, and increasing the number of hits in the tracker improves the pattern recognition of the particle flow algorithm. The particle flow algorithm is discussed in more detail later in this chapter.

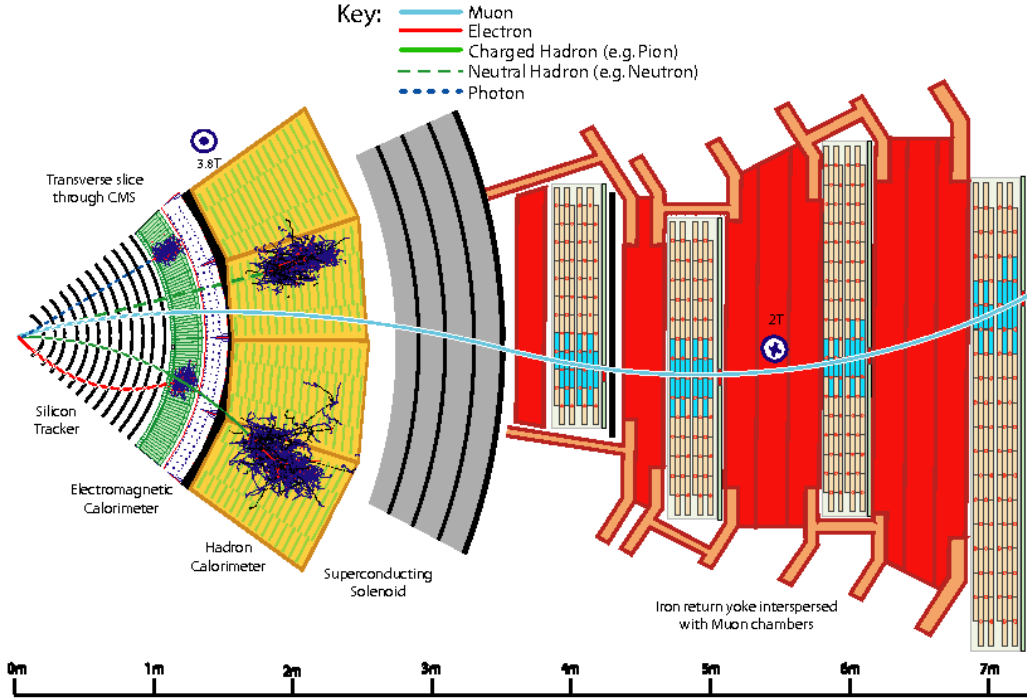


Figure 3.2: CMS radial cross-section [137]

A charged particle causes an electrical signal when passing through a silicon pixel or silicon microstrip. CMS reconstructs these electrical signals, taken at specific points of position and time, into tracks. These tracks are accurate to 10 micrometers. The tracker is meant to have a particle pass all the way through it, with only minimal effect particle's trajectory.

The tracker system is designed for high granularity and fast readout, such that each trajectory can be associated with its corresponding bunch crossing. The tracker is resilient enough to withstand the high flux of particles accompanying every bunch crossing; at design luminosity of $10^{34} \text{cm}^{-2}\text{s}^{-1}$, some 1000 particles will traverse the tracker every 25 ns. However, the mass of the tracker is minimal enough to suppress multiple scattering, off its material, that would distort particle trajectories. These design constraints – resistance and transparency – are satisfied silicon. The tracker has approximately 200m^2 of silicon surface, making it the largest silicon detector ever constructed. The pseudorapidity coverage of the pixel and strip trackers is shown in figure 3.3 [139].

In addition to excellent track reconstruction, the tracker provides high precision vertex recon-

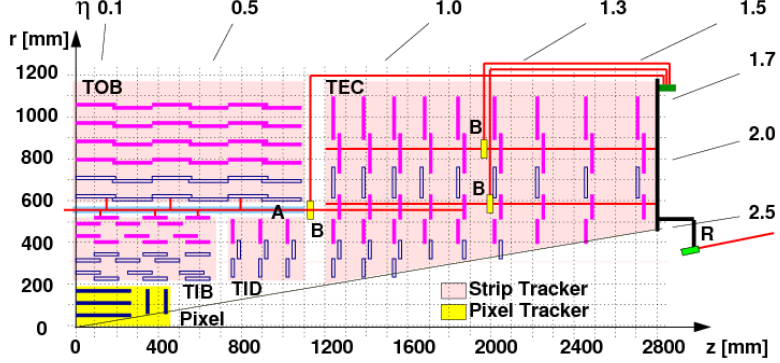


Figure 3.3: Pseudorapidity acceptance of tracker [139]

struction. Vertex reconstruction is a key ingredient in several high-profile LHC studies – Higgs, SUSY, extra-dimensions – because of the use of vertices in distinguishing non-prompt decays of heavy-quarks. The tracker is also instrumental in detecting the leptonic decays of W and Z bosons.

3.2.1.1 Pixel tracker

The first layer of the tracker is made of silicon pixel modules. This layer has a time resolution on the scale of 25 ns, meaning that it can take data for individual bunch crossings. Pixel technology is used because the high flux of particles, present at high beam luminosities, require high spatial resolution for proper pattern recognition. A major design constraint is that the pixel tracker had to be able to separate distinct tracks in high multiplicity environments. Tracks reconstructed by the pixels can be used to cross-check the results from the other parts of the tracker.

Every silicon-pixel has a corresponding readout chip. The readout chips are soldered through the bump-bonding method. The readout chip amplifies signals from the pixel. The pixel tracker is precise enough to distinguish the vertices of tracks originating from short-lived particles, such as bottomonia. The innermost elements of the pixel tracker come within 4.4 cms of the CMS interaction point. The pixel tracker covers a pseudorapidity range of $|\eta| < 2.5$ with some 66×10^6 separate pixels.

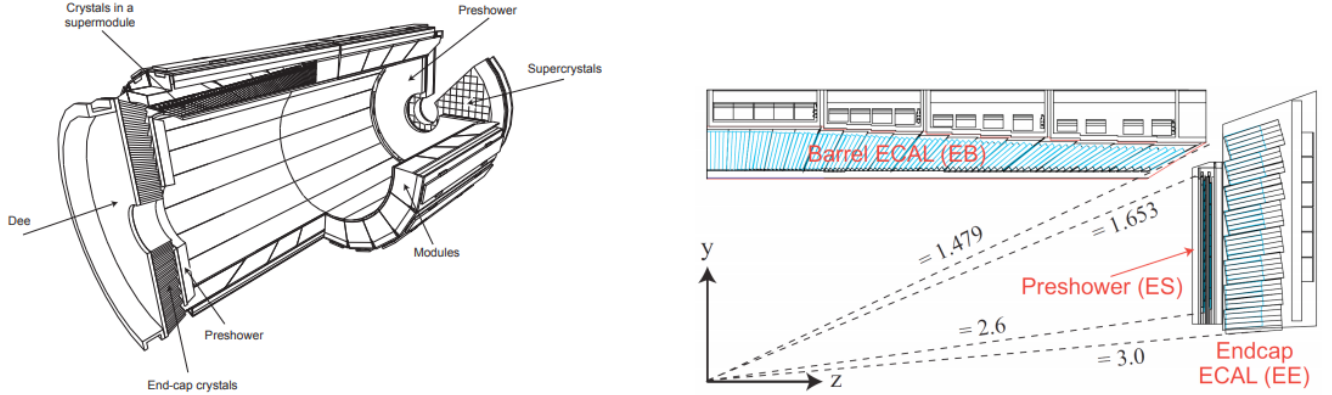


Figure 3.4: ECAL components [140]

3.2.1.2 Strip tracker

Outside the pixel tracker are the layers of the strip tracker. They function similar to the components of the pixel tracker, except the strip tracker consists of thin silicon plates. The strip tracker itself can be broken down into four components: the inner barrel layer, the inner endcaps, the outer barrel layer, and the outer endcaps. In total, these layers contain some 9.3×10^6 strips.

3.2.2 Electromagnetic calorimeter

The Electromagnetic Calorimeter (ECAL) is the dedicated CMS calorimeter for detecting electrons and photons. The calorimeter is comprised of lead tungstate ($PbWO_4$) crystals arranged in cylinder about the beam, including two endcaps, as seen in figure 3.4 [140]. The granularity of these crystals gives the ECAL excellent energy resolution, angular resolution, and spatial resolution; for example, the ECAL has the resolution suitable for the decay of the Higgs boson into two photons. The ECAL is both hermetic and homogenous [141].

The data readout is fast enough that CMS can trigger off signals in the ECAL. It takes about 25 ns for an ECAL hit to scintillate 80 percent of its lights, putting the calorimeter's rate on the same scale as the bunch crossing. Scintillation in the crystals activates photodetectors that transmit information to the L1 trigger. In the barrel these photodetectors are avalanche photodiodes (APDs). The endcaps use vacuum phototriodes (VPTs). ECAL's energy resolution, as a function of energy,

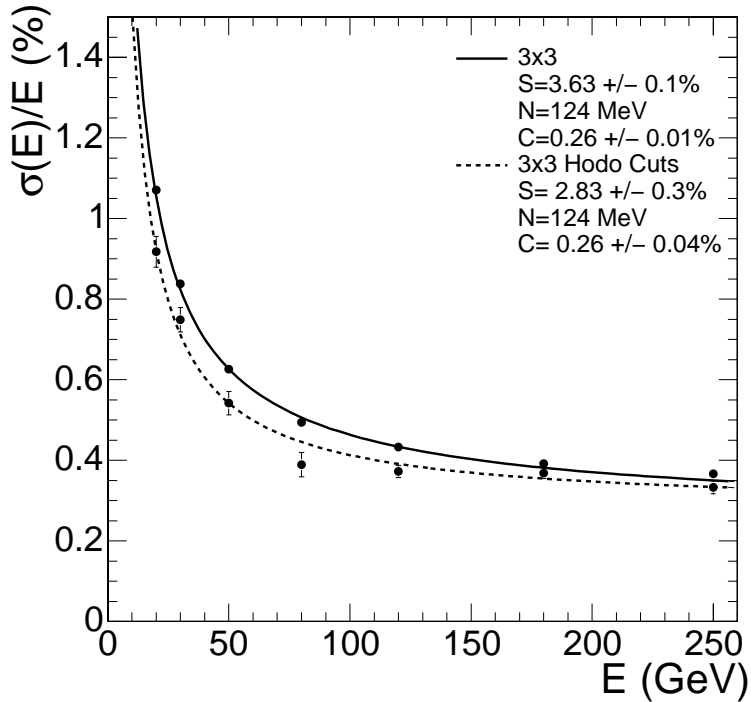


Figure 3.5: Reconstructed data, ECAL energy resolution [142]

is given by figure 3.5 [142]. The resolution increases with energy because, at large energies, parton showers become more similar as their random fluctuations average-out.

In CMS trigger development, "EG" triggers fire based on energy deposits in the ECAL; fig.3.6 gives the EG trigger energy resolution [142]. This energy comes primarily from electrons and photons. When these particles strike a tungstate crystal, the particle shower size is approximately that of the crystal. Electrons are distinguished from photons by the correlation of track to ECAL energy. The L1 trigger does not fire on tracks, which are reconstructed at the HLT level. Thus, L1 EG triggers do not distinguish between electrons and photons.

3.2.3 Hadronic calorimeter

The Hadronic Calorimeter (HCAL) is the next layer outside the ECAL. The HCAL is a sampling calorimeter, meaning that it absorbs particles and measures their energy and momentum via scintillation. HCAL has such a large acceptance that it can indirectly observe non-interacting particles such as neutrinos. The HCAL is designed to be hermetic, so that imbalances of momentum and

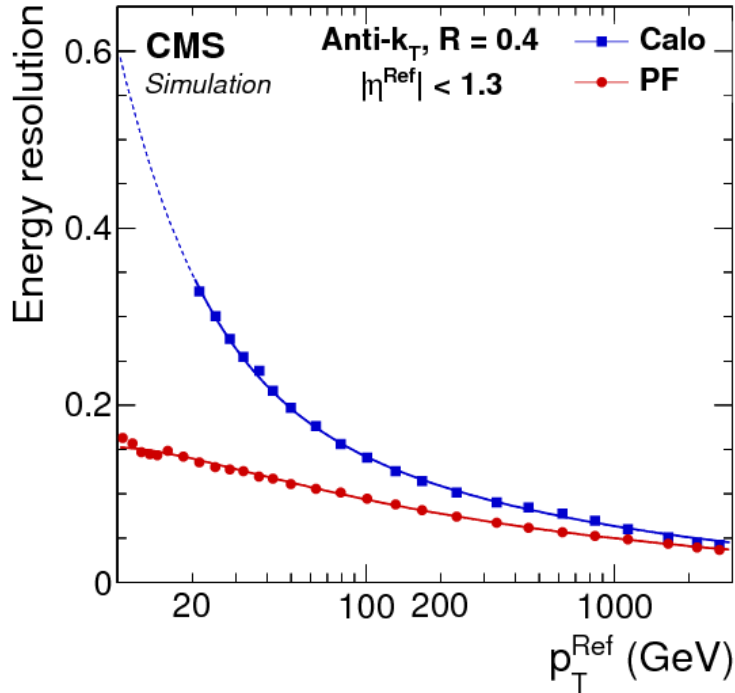


Figure 3.6: L1 trigger, ECAL energy resolution [142]

energy can be precisely measured [143]. Figure 3.7 plots the HCAL’s energy resolution; note that the resolution changes with $|\eta|$ [142].

There are four sub-sections of the HCAL: the inner barrel (HB) and the outer barrel (HO), two endcaps (HE), and two forward calorimeters (HF). The HF are the most relevant to this analysis because of their use in triggering on non-hadronic events. Fig.3.8 shows the HCAL energy resolution [142].

3.2.3.1 Hadronic forward calorimeters

The Hadronic Forward Calorimeters (HF) absorbs the greatest portion of energy from collisions. As named, it is located in the forward region ($3.0 < |\eta| < 5.2$) of CMS and complements the coverage provided by the barrel and endcap detectors.

HCAL is made of quartz fibers and steel absorbers for maximum radiative resistance. When high energy particles pass through the quartz fibers, these particles are moving faster than the speed of light in the medium, depositing energy that causes particle showers. These showers give off

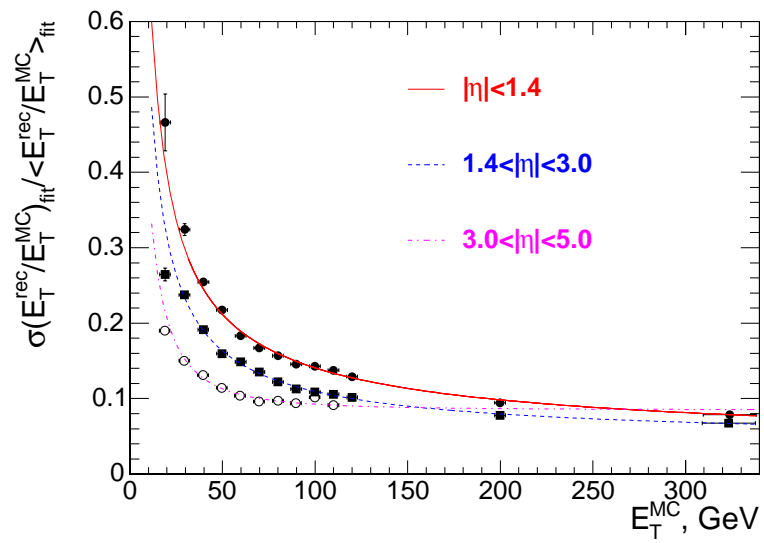


Figure 3.7: HCAL energy resolution [142]

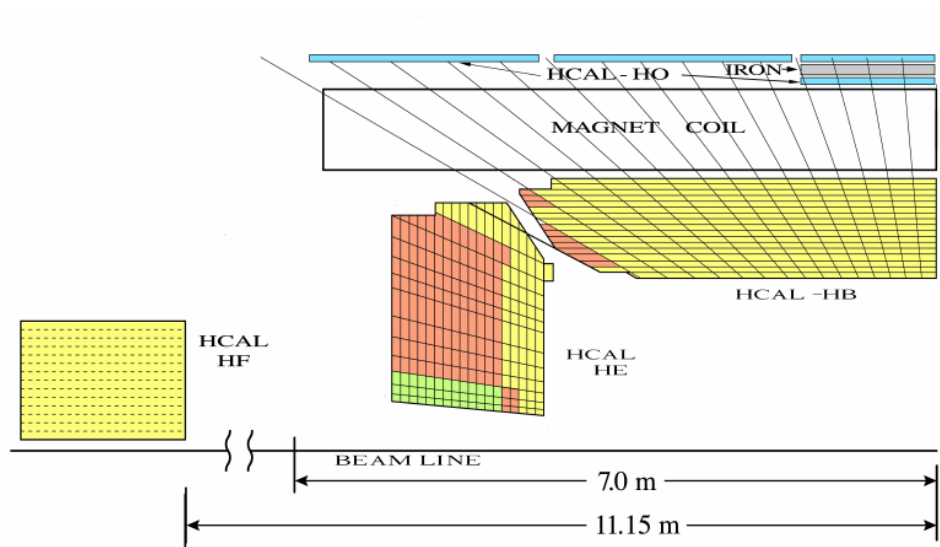


Figure 3.8: HCAL Components [142]

light, in the form of Cherenkov radiation, that the fibers transmit to photomultiplier tubes (PMTs). The PMT signals are converted into a digital signal by a charge integration encoder (QIE) chip. Then HCAL trigger and readout boards (HTR) use these digital signals to calculate luminosity. The HTR information is part of the data used for L1-triggering. Triggering on HF can also be done by vetoing on HF activity.

Hits in the HF are used to measure the instantaneous luminosity of CMS. As shown in fig.3.7, the HF have a finer E_T resolution than the other parts of the HCAL, making it suitable for high precision measurement of luminosity. Furthermore, because HF noise is comparatively small with respect to Minbias HF threshold, the veto of the HF threshold is a reliable measure of HF "emptiness".

3.2.4 Muon detector

The outermost layer of CMS consists of the muon detectors, as seen in figure 3.9 [142]. Muons are particles nearly identical to electrons, except for their mass, which exceeds that of the electron by some two orders of magnitude. High mass particles, like the Higgs boson, often decay into a final state containing muons. The muon detector not only identifies muons, but also measures their momentum. The muon detector has readout fast enough for triggering on muons [144] [145].

The muon detector consists of three types of component: muon drift tubes (DT), cathode strip chambers (CSC), and resistive plate chambers (RPC). The DTs are gas filled chambers that contain a stretched metal wire. When muons pass through the DT gas, electrons are excited. These electrons escape from the gas atoms and are attracted to the metal wire, which triggers a signal. The CSC, located in the endcaps, operate under similar principles, but contain perpendicular arrays of positively charged and negatively charged wires immersed in gas. The RPC do not use electrode wires to detect excited electrons; instead, high-resitiviy plates are used as alternating cathodes and anodes [146].

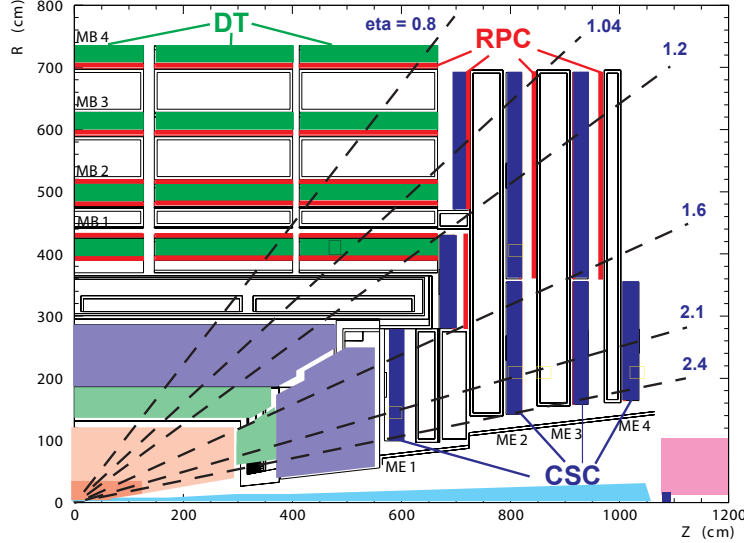


Figure 3.9: Pseudorapidity acceptance of muon detector [142]

3.2.5 Zero degree calorimeter

The zero degree calorimeters are both sides of CMS, approximately 140 meters from the interaction point. Each ZDC consists of two independent systems: an electromagnetic calorimeter, for detecting very forward photons, and a hadronic calorimeter, for detecting neutrons. Because these neutrons result from the dissociation of nuclei, the ZDC can measure the centrality of heavy-ion collisions. Hadrons in the forward region have energy on the TeV scale, so the ZDC's hadronic calorimeter is made of thick tungsten plates [147]. For a UPC process, the photon emitting nucleus is most likely to remain intact; therefore, ZDC data can the photon direction of a process, and by extension it's energy. Tagging forward neutrons can also be used as an online luminometer [148].

3.2.6 Particle flow algorithm

Raw data from the sub-detectors is combined, for data analysis, by the particle-flow (PF) algorithm. The PF takes the data about tracks in the tracker and energy deposits in the calorimeter, and uses them to reconstruct physics-related data objects, like jets, and to identify specific particles, such as photons and muons. The PF also identifies missing energy and momentum for use in neutrino studies.

Unlike physics-objects in the data of previous experiments, PF physics-objects can fire HLTs. After an event passes the L1 trigger, a partial event reconstruction is performed. Energy deposits in the HCAL that can be associated with a track signify charged hadron candidates; if the track-associated energy deposit is in the ECAL, the corresponding object is an electron candidate. Tracks not associated with a calorimeter deposit are considered muon candidates. Left over energy deposits are used to create neutral hadron candidates, if in the HCAL, or photon candidates, if in the ECAL. Each of these candidates is assigned a four-vector based on the sub-detector information [149].

The collection of basic PF candidates are used to create more complex physics objects. The total transverse momentum of the event is used to locate "missing transverse momentum" (MET). MET candidates have a four-vector, and can be used to construct exotic physics-objects such as neutrinos. The curvature of tracks is used to measure the momentum and charge to mass ratio of the charged hadrons, and thus their particle species. The identity of the particles can then be interpreted as the decay of short-lived particles, such as the τ lepton. The speed and efficiency of the calculation and combination of PF objects enables CMS to trigger for a wide variety of physics by modifying software.

The PF is also responsible for implementing the jet reconstruction algorithms of CMS. This thesis's analysis uses the anti- kt jet reconstruction algorithm. Anti- kt algorithms are sequential algorithms that take into account two quantities: the distance between two given particles i and j , d_{ij} , and the distance between a given particle i and the beam, d_{iB} . For a specific particle i , all the d_{ij} and d_{iB} are calculated. If the smallest quantity in the collection is d_{ij} , the particles i and j are combined as four-vectors. The sum four-vector replaces particle i , and all of the distances are recalculated. If the smallest quantity d_{iB} is the smallest quantity, then i is designated a "jet" and removed from the collection. This process iterates until all particles are removed from the collection, replaced by "jets" associated with one or more particles [150].

CMS gains significant jet reconstruction efficiency via the PF. At low transverse momentum, PF reconstructs jets at nearly twice the resolution of HCAL and ECAL. This increase in efficiency

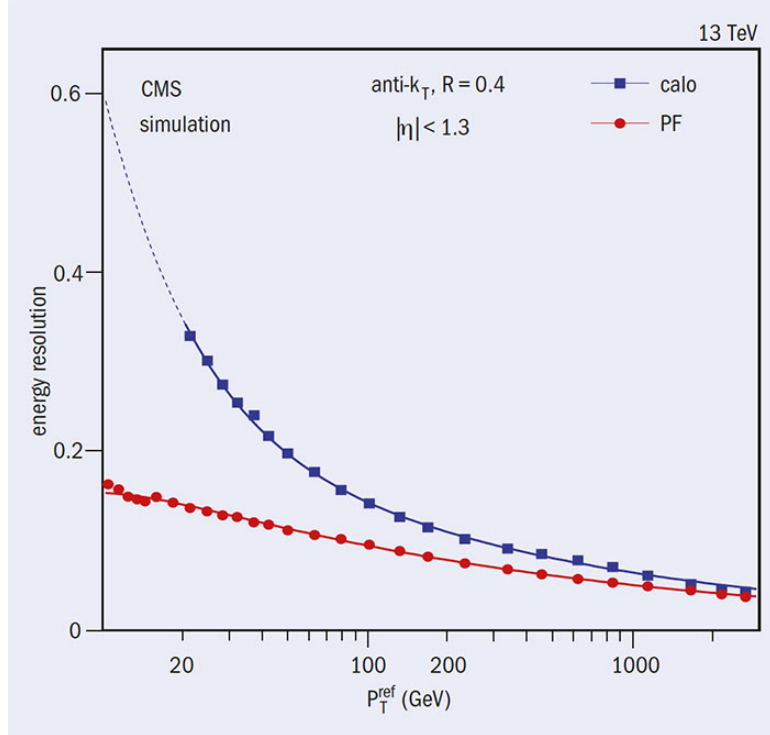


Figure 3.10: Performance of particle flow alorgithm compared to calorimeter readout [151]

comes from the PF integrating in track data with the calorimeter tower data. Figure 3.10 compares the performance of the PF algorithm to the calorimter reconstruction [151].

CMS was the first modern collider experiment to replace traditional triggering, based on energy-deposits and tracks, with HLTs leveraging PF-reconstructed particles. This achievement was enabled by the high precision, high accuracy technologies described in this chapter. Experimentalists, now more than ever, prepare their analyses with unprecedently accurate analogues to processes calculated by theorists. For a given process, a theorist can determine the properties of the final state particles, and encode these in an MC generator. Experimentalists can then run the MC through a simulation of CMS and compare what the PF reconstructs to the MC-truth. This technique is particularly useful for emulating the performance of trigger menus for specific particle productions [149].

Chapter 4

Measuring luminosity

4.1 Instantaneous luminosity

One of the most important quantities measured by CMS is luminosity. Luminosity is necessary to convert the number of events detected, for a given channel, into a collision cross-section. Collision cross-sections are among the primary observables predicted by theoretical physics, specifically quantum field theory. For particle physics, the collision cross-section of a process is typically measured through the relation:

$$\sigma = \frac{R}{L}, \quad (4.1)$$

where σ is the cross-section, R is the rate at which the process occurs per collision, and L is the instantaneous luminosity. L is measured via the rate of a given luminometer and taking into account both the acceptance A ,

$$L = \frac{R}{\sigma_o(E)A(t, \mu, n_b, \dots)}, \quad (4.2)$$

The denominator is typically measured as the visible cross section, σ_{vis} ,

$$\sigma_{vis} = \sigma_o(E)A(t, \mu, n_b, \dots), \quad (4.3)$$

where $\sigma_o(E)$ is comes from the separating out the dependence of σ_{vis} on collision energy E . σ_{vis} ideally has no dependence on time or experiment conditions, i.e. constant with respect to pile-up and invariant to filling scheme. For example activity in the HF scales with the instantaneous luminosity. Therefore, the visible cross-section – which has no time dependence – can be used as calibration constant for converting the rate of HF activity into instantaneous luminosity. Every luminometer should have its own characteristic visible cross section. In this way, multiple

independent luminometers can cross check each other [152] [153][154].

4.2 Luminometers

There are two kinds of CMS luminometer: online and offline. Online luminometers readout the luminosity per bunch in real time. As of 2015 there are three online luminometers: the pixel luminosity telescope (PLT), the HF, and the beam conditions monitor (BCM1f). There is a high-rate, independent data-acquisition system for each of the online luminometers. Offline luminometers measure the rate of reconstructed objects. The primary offline lumimoneter is the pixel tracker. In general, the offline luminometers have better stability over time. [155]

The online and offline luminometers complement each other for high precision data analysis. Specifically, the offline data can be used to calibrate out imperfections in the online data.

In addition to these hardware luminometers, CMS can use physics processes as luminosity benchmarks. For example, other experiments have measured the Z-boson cross-section to a high accuracy and high precision. Comparing this cross-section to the Z-boson mass-peak ,in CMS data, provides a cross-check to the delivered luminosity.

4.2.1 Pixel cluster counting

One of the primary methods of measuring instantaneous luminosity is through pixel cluster counting (PCC) in the pixel-tracker. The collision rate is linked to instantaneous luminosity L via the total inelastic cross-section σ_T

$$v\mu = L\sigma_T, \quad (4.4)$$

where $v = 11246$ Hz is the beam revolution frequency and μ is the number of collisions per bunch crossing. We define the average number of pixel clusters per event, $\langle n \rangle$, as

$$\langle n \rangle = \mu n_1, \quad (4.5)$$

and the visible cross section σ_{vis} as

$$\sigma_{vis} = \sigma_T n_1, \quad (4.6)$$

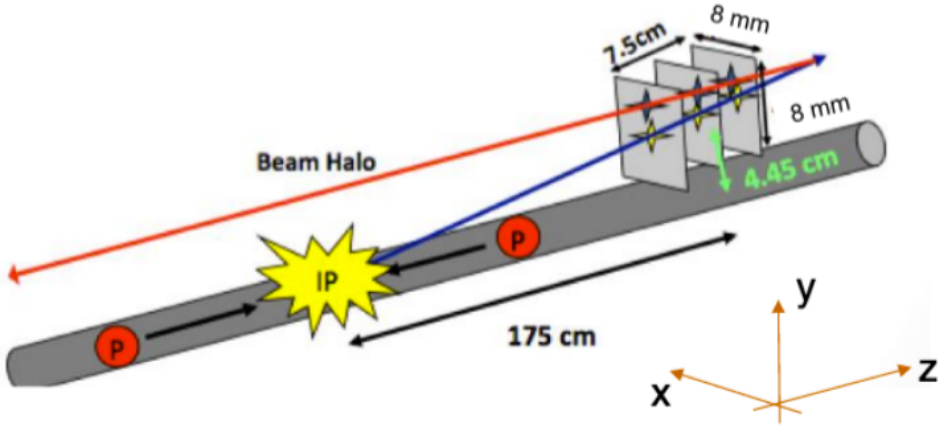


Figure 4.1: PLT triple coincidence

where n_1 is the average number of pixel clusters per inelastic collision. Leveraging the previous two equations, the instantaneous luminosity reduces to

$$L = \frac{v \langle n \rangle}{\sigma_{vis}}, \quad (4.7)$$

such that L can be calculated after measuring the actual $\langle n \rangle$ of the data [152]

4.2.2 Pixel luminosity telescope

The pixel luminosity telescope (PLT) is one of the online luminometers of CMS. The PLT consists of 8 pixel telescopes arranged around the beamline on either side of the CMS interaction point. Each telescope has three layers of silicon pixel detector. Triple coincidences in these telescopes are measured as luminosity on a bunch-by-bunch basis. As an independent luminometer, the PLT data is also useful for reducing the systematic uncertainty of the luminosity delivered to CMS.

The PLT was installed as part of the CMS Run-2 upgrades. As of this writing, it is the only subdetector of CMS dedicated solely to measuring instantaneous luminosity. The hardware of the pixel sensors and the readout chip are similar to those used by the pixel tracker. However, the readout chips (ROC) of the PLT are capable of delivering fast-OR formatted data; the pixel tracker cannot do this. The fast-OR readout is optimized for delivering triple-coincidence data; whereas the standard pixel data readout has a max frequency of 100 kHz, the PLT fast-OR readout maxes out at an orders of magnitude greater frequency, at 40 Mhz [156].

4.2.3 Hadronic forward calorimeter

The hadronic forward calorimeter (HF) of CMS is capable of measuring luminosity. Because of the high flux of particles through the forward region, the HF-luminosity is less subject to statistical uncertainty than the PCC-luminosity. The HF can measure luminosity per bunch through its own dedicated high-rate acquisition system that is separate from the CMS DAQ. Within the HF, the HTR boards each have an additional HF luminosity transmission circuit (HLX). The HLX are mounted in one of the mezzanine expansion slots of the HTR.

The HF luminosity is subject to two difficulties. Because the PMTs require a calibrated voltage, the accumulation of gain changes over long periods of time will cause calibration drifts. Furthermore, the HF detector response has been shown to be nonlinear with respect to vertex pile-up. Substantial data analysis goes into calculating the corrections to these two sources of error [152].

4.2.4 Fast Beam Conditions Monitor

The CMS Beam Conditions and Radiation Monitoring System (BRM) provides a wide variety of information on the accumulated radiation dosage into CMS. This information is essential for protecting CMS from radiation damage. There are many subcomponents to the BRM system, one of which is the Fast Beam Conditions Monitor (BCM1f). The BCM1f is capable of measuring the beam-halo background and the flux from collision products. Similar to the PLT, BCM1f is located close to the beam pipe; however, BCM1f uses diamonds instead of silicon pixels. The readout from BCM1f is not digital, but an analog signal sent through optical fibres.

There are 24 single crystal diamond sensors in the BCM1f system. The BCM1f is located very close to interaction point, specifically 1.8 m on either side. This location is chosen specifically to take advantage of the 25 ns between bunch crossings. From the BCM1f vantage point there is a 12.5 ns delay between particle fluxes from the machine induced background and those coming from actual collisions. Thus the BCM1f can use timing to distinguish between signal and background [157].

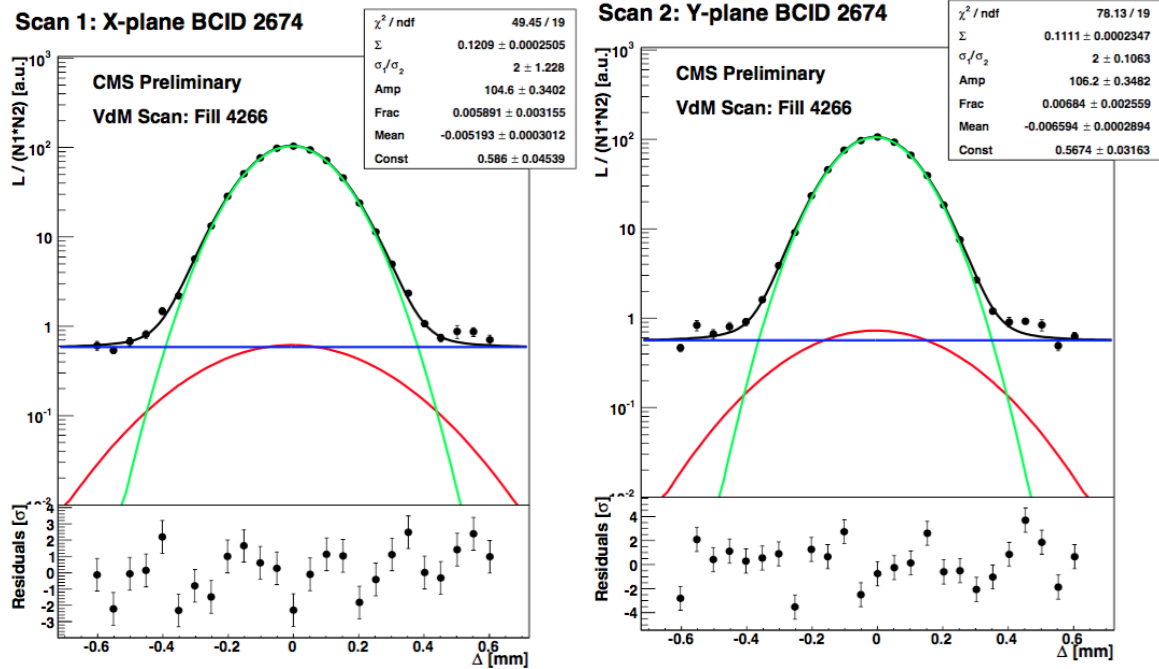


Figure 4.2: PCC VdM Scans [152]

4.3 Van de Meer scanning calibration

The luminometers of CMS produce signals proportional to the instantaneous luminosity of the LHC beam. However, these signals need to be properly calibrated with respect to a known visible cross-section for each luminometer. This calibration is accomplished via Van de Meer scanning [158]. The opposing beams of LHC are moved back and forth in the transverse plane. During the scan, the detector response is measured as a function of beam displacement. The beam widths are calculated from Gaussian fits to the detector response. The visible cross-section of the luminometer in question is then derived from the width of the beams, and acts as the calibration of the detector response. Figure 4.2 presents the fitting of the VdM scan in the X and Y planes [152].

$$\sigma_{vis} = \frac{2\pi\Sigma_x\Sigma_y v \langle n \rangle_{\Delta=0}}{N_1 N_2}, \quad (4.8)$$

4.4 Corrections to VDM scans

Several corrections must be applied to VdM scan data before calculating the visible cross section. These corrections are considered uncorrelated, i.e. it does not matter in what order they are applied.

The results of the VDM scan must be corrected for the following phenomena: the length scale, the ghosts and satellite background, the growth in beam emittance, orbit drift, and beam-beam electromagnetic effects. These affect the normalization of the VDM scans, and so the corrections take the form of calibration constants derived from additional scans and beam monitoring subdetectors [152].

The length scale correction is derived by comparing the effects of a length scan to the response of the tracker; checking the difference between the reported beam displacement and that seen in the tracker. In addition to the circulating bunches, the LHC beams can be polluted by foreign particles that were not intended for injection by LHC commissioning. The presence of these foreign particles – fleeting "ghosts" and persistent "satellites" – can be detected by comparing the total beam current, measured by the DC beam current transformer, against the per bunch current measured by the FBCT. The FBCT, because it is timed for bunch crossings, is less likely to interact with ghosts and satellites. Variations in beam emittance affect the VdM scans by changing the amplitude and width of the rate profile. The orbit drift correction is based on data from the Beam Position Monitors (BPM), which measure the position of the beam orbit in LHC. Lastly, beam-beam effects refer to the electromagnetic forces that the beams exert on each other; for example, when the beams are transversely separated there is a small, but statistically significant, induced magnetic force.

4.5 Systematic uncertainty

Figure 4.3 displays the systematic uncertainties associated with the delivered luminosity. The "normalization" uncertainties are for the visible cross section, σ_{vis} . The "integration" uncertainties are for the integrated luminosity that is calculated using the σ_{vis} . The stability uncertainty is calculated from comparing the relative contributions of pixel tracker layers to total number of pixel clusters measured in a span of time. From run to run, each pixel layer contribution varies by no more than 1%. It is possible for the rate of high track multiplicity events to exceed the temporary storage capacity of the tracker read-out buffer; the resulting inefficiencies are mainly found in the first barrel layer of the tracker. The "afterglow" refers to background noise associated with electrical

	Systematic	correction (%)	uncertainty (%)
Integration	Stability	-	1
	type 1	7 – 9	0.6
	type 2	0 – 4	0.7
	CMS deadtime	-	0.5
	Dynamic Inefficiency	-	0.4
Normalization	XY-Correlations	1.1	1.5
	Beam current calibration	-	0.3
	Ghosts and satellites	-	0.2
	Length scale	-3.2	1.5
	Orbit Drift	-	0.4
	Beam-beam deflection	1.8	0.4
	Dynamic- β	-	0.5
	Total		2.7

Figure 4.3: Systematic Uncertainty During 2015 pp Run [152]

excitations in the detector material, and warrants a correction factor to the integrated luminosity.

4.6 Author’s contributions

LHC produces a staggering amount of data. The 2015 heavy-ion run itself recorded some $1.4 pb^{-1}$ in integrated luminosity. This integrated luminosity is reconstructed into data on the order of pentabytes. Figure 4.4 is a table of the LHC comprising the 2015 Pb-Pb run, and presents for each fill the peak instantaneous luminosity, delivered integrated luminosity, and recorded integrated luminosity. The last column, EffbyLumi, is the ratio of the delivered to recorded integrated luminosities.

I contributed to CMS luminosity validation, and performed studies on the long-term stability of the BRIL luminometers. On a week by week basis, I would examine the data from online and offline luminometers and certify that it met the quality standards of CMS. If the data exhibited non-linear behavior, I would de-certify the corresponding lumi-sections in the BRIL json files.

All CMS data has to go through a data certification workflow. Data certification insures that only valid data is used in CMS analyses. Decisions on data certification are recorded in two systems: the DQM Run Registry, shown here in figure 4.5, and the normtag JSON files of the BRIL-DPG. There are occasions when the sub-detectors of CMS might record poor quality data. For example, the software reading out data from the PLT could crash and thus compromise the

Fill	Begin Time YYYY.MM.DD HH:MM	Duration HH:MM	PeakInstLumi $\times 10^{30} \text{cm}^{-2}\text{s}^{-1}$ pp $\times 10^{24} \text{cm}^{-2}\text{s}^{-1}$ ions	DeliveredLumi pb^{-1} pp μb^{-1} PbPb	RecordedLumi pb^{-1} pp μb^{-1} PbPb	EffByLumi %
4658	2015.11.25 09:59	05:40	1	0.0	0.0	84.4
4659	2015.11.25 22:51	02:12	89	0.6	0.5	95.6
4661	2015.11.26 07:04	02:55	97	0.8	0.5	69.6
4664	2015.11.26 16:33	04:27	547	5.3	4.5	85.7
4666	2015.11.27 08:34	05:05	721	7.0	6.2	88.8
4669	2015.11.27 21:31	06:10	1327	16.1	12.8	79.2
4671	2015.11.28 11:13	09:03	1115	16.5	14.3	86.9
4672	2015.11.28 23:53	06:55	1085	14.0	11.9	84.6
4677	2015.11.29 17:42	06:54	1011	14.0	12.5	89.6
4679	2015.11.30 08:27	06:58	1092	14.5	12.9	88.8
4680	2015.11.30 21:17	05:13	1820	19.6	16.7	85.4
4681	2015.12.01 07:40	11:51	1856	28.4	25.1	88.2
4685	2015.12.02 05:39	03:28	1040	8.5	6.0	70.4
4688	2015.12.03 02:44	00:18	1887	1.9	1.0	51.1
4689	2015.12.03 09:03	09:04	1254	10.2	9.9	97.1
4690	2015.12.03 22:10	08:27	2030	22.0	21.7	98.5
4691	2015.12.04 12:51	07:31	2072	26.7	25.8	96.6
4692	2015.12.04 23:23	07:40	2334	30.3	29.7	98.1
4693	2015.12.05 10:22	00:60	2314	7.1	6.9	97.2
4695	2015.12.05 17:29	07:14	2216	27.8	26.2	94.3
4696	2015.12.06 07:03	05:29	1795	19.9	19.4	97.7
4697	2015.12.06 16:34	05:30	1879	20.5	20.1	98.2
4698	2015.12.07 01:41	00:09	2102	1.0	0.9	87.2
4699	2015.12.07 05:30	05:40	1885	21.5	20.4	94.8
4705	2015.12.08 05:37	02:24	183	1.1	1.1	97.8
4706	2015.12.08 11:08	04:32	2433	23.5	22.7	96.5
4709	2015.12.09 08:41	05:47	2161	23.3	22.8	97.8
4710	2015.12.09 17:42	05:52	2967	32.8	32.2	98.3
4711	2015.12.10 02:38	06:37	2886	31.6	31.1	98.4
4714	2015.12.11 01:20	06:39	2500	29.3	28.2	96.2
4715	2015.12.11 11:37	06:31	2559	30.6	29.3	95.7
4717	2015.12.11 23:00	10:21	0	0.0	0.0	0.0
4719	2015.12.12 17:26	04:36	2652	27.2	25.6	94.1
4720	2015.12.13 01:10	10:60	3036	44.9	44.2	98.5
Summary		199:09	3036	578.4	543.1	93.9

Figure 4.4: Luminosity by CMS fill.

output. In this case the certification workers would record the lumi sections during which the PLT software crashed. These lumi sections would be removed from the normtag JSON file passed on to the BRIL group. If all te luminometers are malfunctioning, a whole run could be invalidated in the run registry.

In additon to data certification, I reviewed the long-term stability of the BRIL luminometers during the 2015 and 2016 proton-proton runs. Stability refers to the comparative performance of the different luminometers. Ideally, the ratio of the instantaneous luminosity reported by separate luminometers should be a constant ratio, but in fact there is a tendency for this ratio to drift as a result of radiation damage to the luminometers. This drift can be seen in plotting the average ratio

Figure 4.5: CMS Run Registry.

as a function of interaction rate and of the different measures of LHC time: runs, lumi-sections, and bunch-crossings. Instantaneous luminosity, in theory, should be independent of machine conditions like acceptance and efficiency. Figure 4.6 is records the sum of the delivered and recorded integrated luminosity for each day of the 2015 Pb-Pb run.

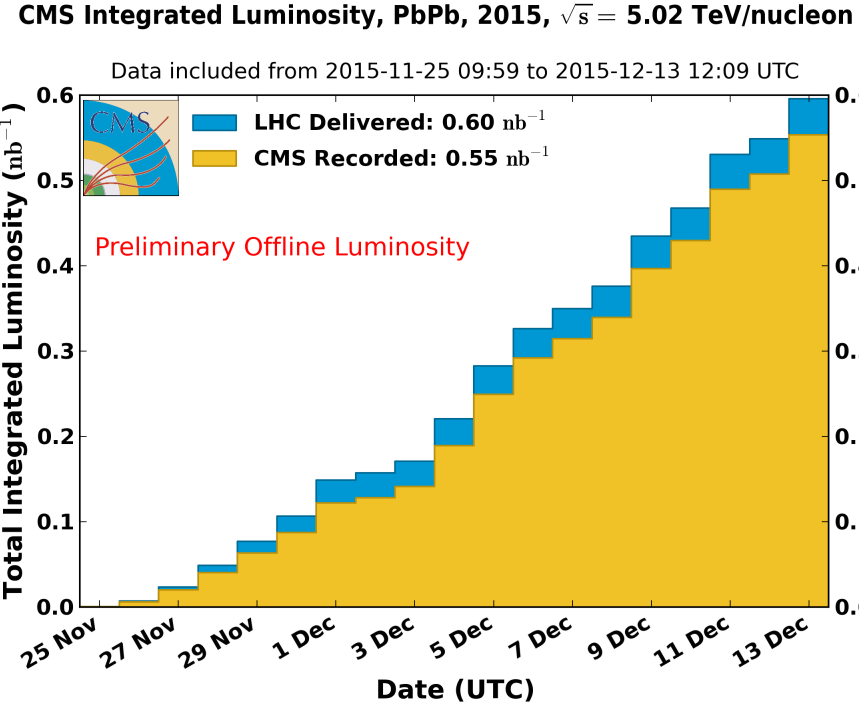


Figure 4.6: CMS lumi during HI-2015.

Figure 4.7 is the CMS-recorded integrated luminosity for each proton-proton era of LHC. No-

tice that as the collision energy increases, the recorded luminosity grows at steeper and steeper rate. This acceleration in the recorded luminosity is consistent with the higher multiplicity of high energy collisions. As LHC pushes the energy frontier, high quality luminosity analysis will become even more fundamental for the continued performance of CMS. The "High Luminosity Large Hadron Collider" (HL-LHC) is a project to increase the design luminosity of LHC by an order of magnitude by 2025. To fully leverage the power of this increased luminosity, particularly for studying possible anomalous couplings, CMS must continue providing measures of luminosity with tightly controlled systematic uncertainty.

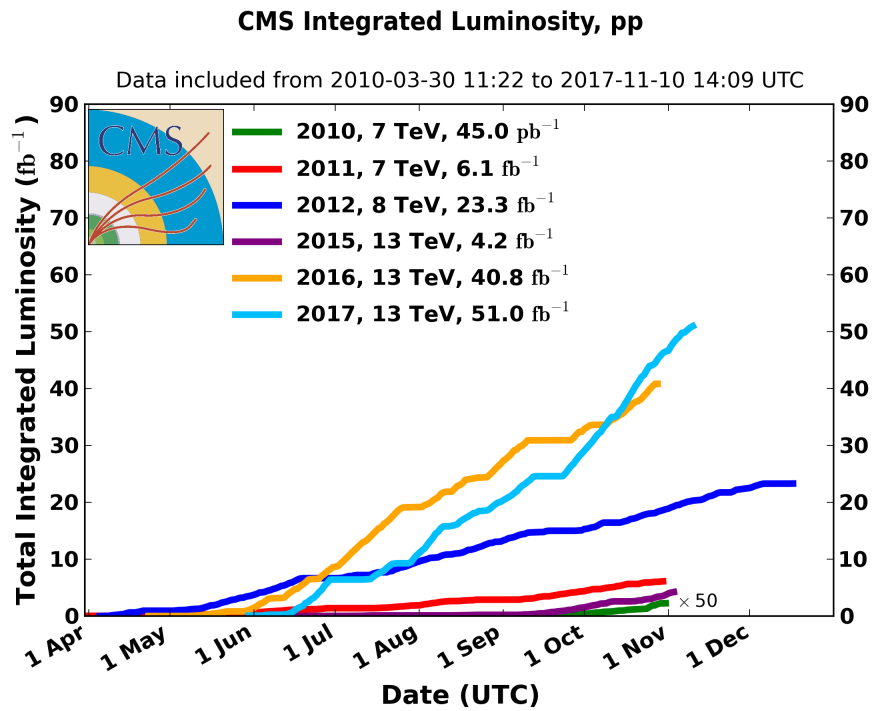


Figure 4.7: CMS Lumi by Era.

Chapter 5

Trigger development and performance

5.1 Introduction to triggering

Modern "triggering" methods began with Walther Bothe's development of the coincidence method.

In 1923 Bothe and Hans Geiger performed experiments on recoil electrons from Compton scattering. It was observed that there was a strong correlation between the trajectory of the recoil electron and that of the scattered photon. The correlation exhibited conservation of energy, conservation of momentum, and was consistent with the quantisation of energy.

Bruno Rossi improved on Bothe and Geiger's photography based equipment with an electrical circuit. The coincidence circuit accepts two inputs. If these inputs are received within the same time window, approximating coincidence, the circuit passes an output. Figure 5.1 is the diagram of a coincidence circuit [159]. Notice that there are three transistors that are each connected to a

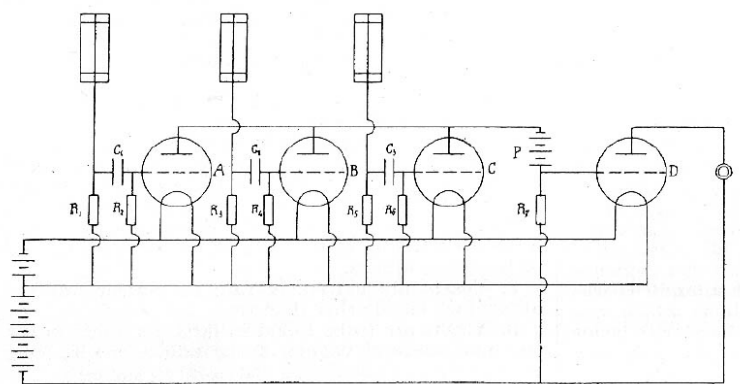


Figure 5.1: Rossi circuit with three Geiger-Muller coincidence circuits [159]

muon detector. These three transistors are in series with each other, but are in parallel with a fourth transistor. A signal registers when current passes through this fourth transistor. To open the fourth

transistor, all three of the muon detectors must fire within a given time interval specified by the transistors.

The first coincidence circuits were used in cosmic ray experiments as higher frequency alternative to ion cloud chambers.

5.2 Triggering at CMS

At stable beams, the LHC delivers bunch crossings every 25 nanoseconds. Each bunch crossing in turn will have some 20 hadron collisions. The resulting interaction rate – 10^9 interactions per second – is orders of magnitude greater than the frequency that events can be written to disk, 10^2 events per second. CMS therefore needs a means of filtering out the most interesting 10^2 interactions per second while declining the other 10^6 interactions per second.

CMS uses a two-tiered triggering system. The first tier, the L1 trigger, is hardware based. The second tier, the high-level trigger (HLT), is software based. The L1 trigger receives raw data from the calorimeters and the muon detectors; this determines when the tracker will readout data. The raw data from the tracker, calorimeters, and muon detectors is then passed on to a computer farm running the HLT menu. The HLT then performs a simplistic reconstruction of the raw data into physics objects useful for analysis: jets, tracks, and identifiable particles. If an event passes the HLT, the raw data is permanently stored in preparation for a more complex reconstruction [160][161].

The initial interaction rate is approximately $3.2 \mu s$. The L1 trigger can only pass some 1 in 1000 interactions to the HLT. The L1 trigger menu has an output rate of approximately 100 kHz. L1 achieves this rate by only considering data of reduced granularity and reduced resolution. A buffer is used to store the full event data while the L1 runs. The HLT menu reduces this to about 100 Hz as required by the limit on disk writing.

The 2015 UPC triggers were for low multiplicity events and low transverse momentum events. Typical heavy-ion collisions are high multiplicity events. Hard scattering dominates. Fig.5.4 is an event display of one of the first heavy-ion collisions at CMS in 2010.

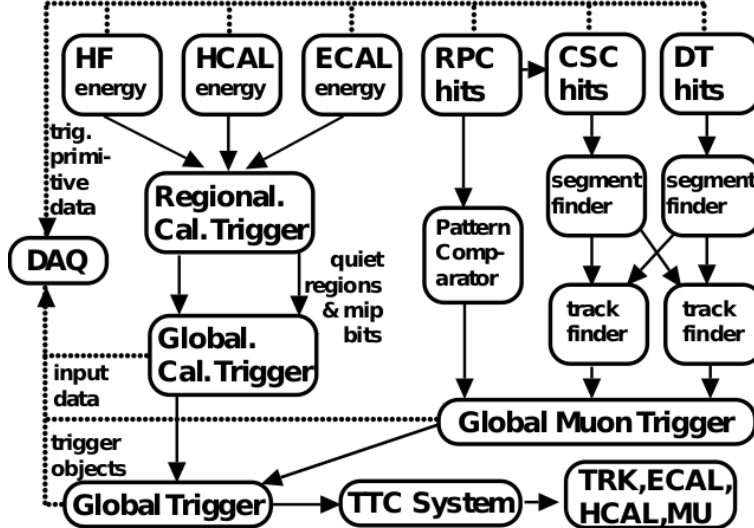


Figure 5.2: Flow of information in L1 trigger

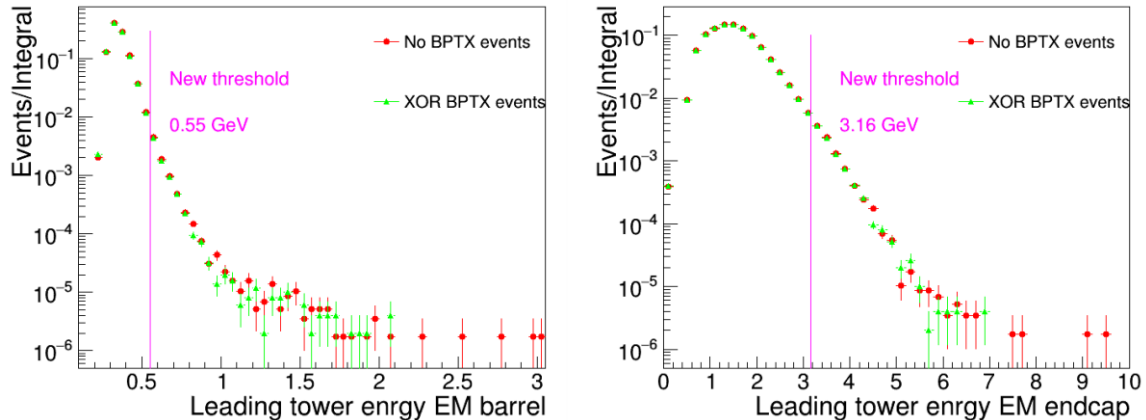


Figure 5.3: Leading tower energy distribution in HF

Fig.5.5 is the event display of a UPC upsilon candidate. Notice that there are only two reconstructed tracks, and that CMS is otherwise empty in all calorimeters. These events constitute a complement to those passing conventional more heavy-ion triggers. However, for Run-2 the Pb-Pb luminosities are high enough that UPC final states can be studied over a wide range of rapidity and p_T .

For this analysis, the L1 trigger applies two selections. First, the L1 checks that at least one of the HF is empty. This is the most important part of the trigger in so far as it suppressed the hadronic contamination of the dataset. Then, if there is at least 5 GeV of energy deposited in the

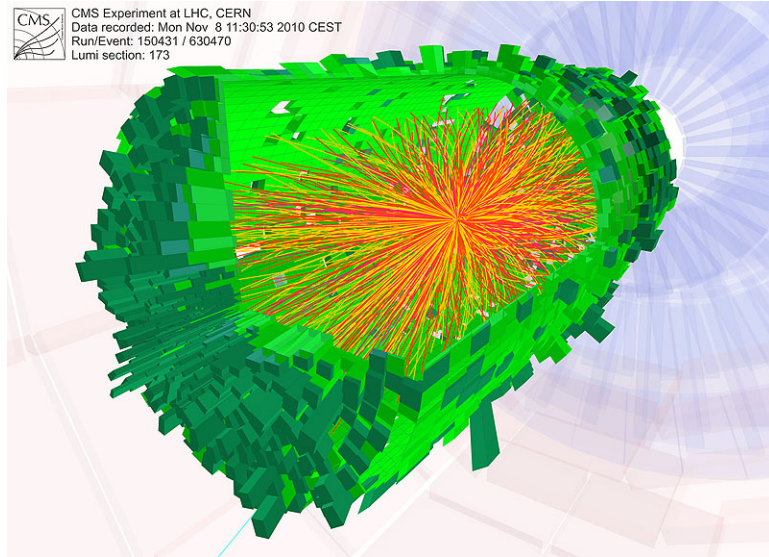


Figure 5.4: High multiplicity PbPb collision

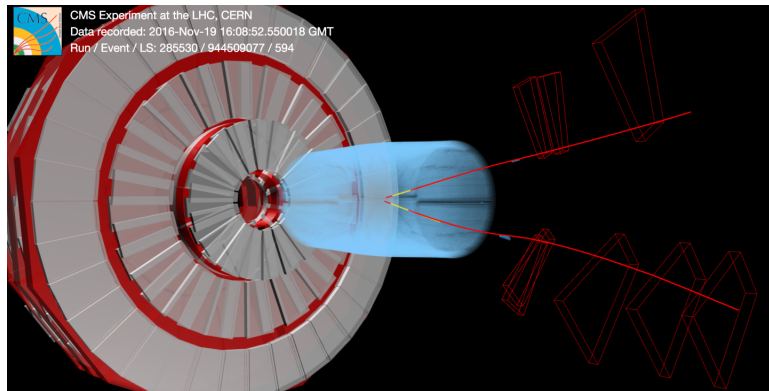


Figure 5.5: UPC Upsilon candidate

ECAL, the event passes to the HLT.

Low multiplicity events are difficult to distinguish from background. To compensate, the HLT in turn requires that there be at least once reconstructed track from the pixel tracker, to make sure that there are particles that will be reconstructed by the complete tracker. Only the pixel tracker is used for these HLTs to increase the speed of reconstruction while decreasing needed computer cycles.

5.3 Author's contributions

5.3.1 Pb+Pb 2015 UPC Triggers

In preparation for the 2015 heavy-ion run and the 2016 p-Pb run, I prepared high-level trigger menus for the CMS Forward-HI group. This trigger menu was optimized for firing on ultra-peripheral collisions. I tested the menu's performance on Monte Carlo generated by STARLIGHT and reconstructed through a GEANT4 simulation of CMS. During the experiment, I was present at CERN to monitor the trigger rates and deliver daily reports on their performance.

CMSSW includes an emulator for the L1 trigger. This software can re-emulate alternative L1 menus on previously taken CMS data. The performance of a trigger on the 2011 PbPb data, taken at $\sqrt{s_{NN}} = 2.7\text{TeV}$ is extrapolated to the higher energy, $\sqrt{s_{NN}} = 5.2\text{TeV}$, of the 2015 PbPb run.

I tested my HLT menu on both STARLIGHT MC and on data from the 2011 Pb+Pb run. STARLIGHT is a MC generator for ultra-peripheral collisions, in particular for the vector-meson photoproduction channels. I used STARLIGHT to generate MC sets for $Pb + Pb \rightarrow J/\Psi + Pb + Pb$ and $Pb + Pb \rightarrow \Upsilon(1s) + Pb + Pb$. I then used CMSSW to test the performance of the component bits of the HLT paths with respect to these MC sets.

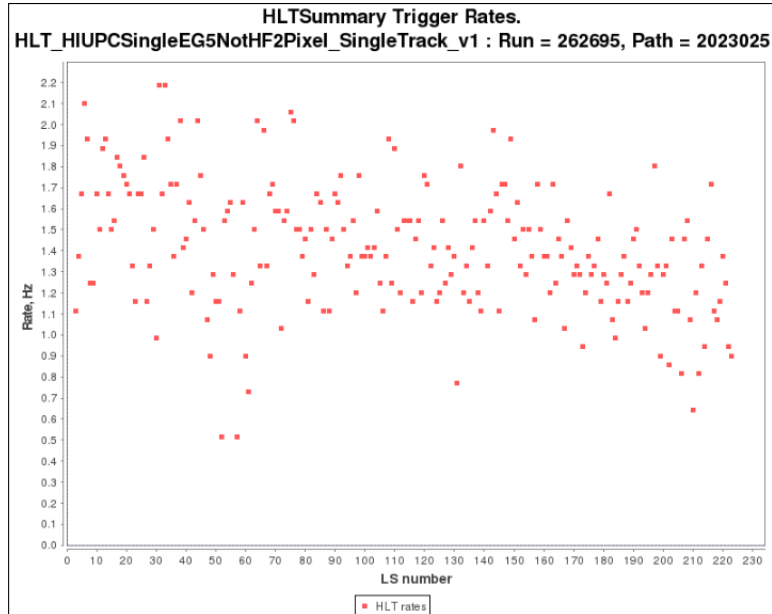


Figure 5.6: Example of trigger rate.

It was my duty to carefully observe the state of the UPC triggers during the heavy-ion run. If the total HLT rate ever drifted above 100 Hz, the HLT menu could crash and CMS lose considerable data. It was important for the trigger contacts to make sure that there HLT paths were behaving stably. I also analyzed express physics data to test that the vector-meson triggers saw appropriate mass resonances.

Table 5.1: L1 Trigger Average Rates for Run 263757

L1 Type	Pre-DT Rate (Hz)	Pre-DT RMS Rate (Hz)	Post-DT Rate (Hz)	Post-DT RMS Rate (Hz)	Initial Prescale	Final Prescale
Double muon + HF veto (thresh. 1)	7.78	8.39	7.64	8.24	0	0
Double muon + HF veto (thresh. 2)	7.86	8.49	7.71	8.33	0	0
Single muon + HF veto (thresh. 2)	85.58	89.76	84.31	88.53	0	0
Double EG2 + HF veto (thresh. 2)	2.26	2.62	2.19	2.54	0	0
Single EG5 + HF veto (thresh. 2)	13.71	16.13	10.8	13.14	0	0

Table 5.2: HLT Average Rates for Run 263757

HLT Type	L1 Seed	Average Rate of HLT (Hz)
L1 pass through	Double muon + HF veto (thresh. 1)	7.64
Requires pixel track	Double muon + HF veto (thresh. 1)	1.09
L1 pass through	Double muon + HF veto (thresh. 2)	7.71
Requires pixel track	Double muon + HF veto (thresh. 2)	1.11
L1 pass through	Single muon + HF veto (thresh. 2)	22.41
Requires pixel track	Single muon + HF veto (thresh. 2)	11.18
L1 pass through	Double EG2 + HF veto (thresh. 2)	2.19
Requires pixel track	Single EG5 + HF veto (thresh. 2)	3.96

5.3.2 p+Pb 2016 UPC Triggers

For the 2016 $p + Pb$ run I prepared a trigger menu similar to that of the 2015 $Pb + Pb$ run.

Table 5.3: L1 Trigger Average Rates for Run 285530

L1 Type	Pre-DT Rate Before Prescale (Hz)	Pre-DT Rate After Prescale (Hz)	Post-DT Rate (Hz)
Double muon + HF veto (1 Tower)	5.47	5.47	5.38
Double muon + HF veto (2 Tower)	5.47	5.47	5.38
Single muon + HF veto (1 Tower)	123.31	123.31	121.15
Single muon + HF veto (2 Tower)	123.31	123.31	121.15
Double EG2 + HF veto (1 Tower)	228.22	N/A	N/A
Double EG2 + HF veto (2 Tower)	228.22	N/A	N/A
Single EG5 + HF veto (1 Tower)	211.17	211.17	207.00
Single EG5 + HF veto (2 Tower)	211.17	211.17	207.00

Table 5.4: HLT Average Rates for Run 285530

HLT Type	L1 Seed	Average Rate of HLT (Hz)
L1 pass through	Double muon + HF veto (1 Tower)	5.40
Requires pixel track	Double muon + HF veto (1 Tower)	1.20
L1 pass through	Double muon + HF veto (2 Tower)	5.40
Requires pixel track	Double muon + HF veto (2 Tower)	1.20
L1 pass through	Single muon + HF veto (1 Tower)	121.70
Requires pixel track	Single muon + HF veto (1 Tower)	58.16
L1 pass through	Single muon + HF veto (2 Tower)	121.70
Requires pixel track	Single muon + HF veto (2 Tower)	58.16
L1 pass through	Double EG2 + HF veto (1 Tower)	N/A
Requires pixel track	Double EG2 + HF veto (1 Tower)	N/A
L1 pass through	Double EG2 + HF veto (2 Tower)	N/A
Requires pixel track	Double EG2 + HF veto (2 Tower)	N/A
L1 pass through	Single EG5 + HF veto (1 Tower)	208.18
Requires pixel track	Single EG5 + HF veto (1 Tower)	159.79
L1 pass through	Single EG5 + HF veto (2 Tower)	208.18
Requires pixel track	Single EG5 + HF veto (2 Tower)	159.79

5.4 Studies from trigger menus

The UPC HLTs I designed are fruitful for a variety of physics studies. In addition to the coherent dijet study that is the subject of this thesis, the data gathered through the 2015 trigger menu can address UPC photoproduction of coherent and incoherent J/Ψ , coherent $\Psi(2s)$, coherent ρ^0 , and

possible ρ^0 excited states. The 2016 trigger menu is uniquely suited for studying exclusive vector meson photoproduction off the proton in p-Pb UPC. All of these studies have the potential for expanding our knowledge of the nuclear gluon PDFs at small-x, from 10^{-2} to 10^{-5} .

Chapter 6

Data analysis

In this chapter our data sample will be analyzed according to the framework provided by Yoshikata Hatta. The angular correlation of jets is taken, and event mixing is used to factor out acceptance effects.

[Something about the MC generation [162]]

The ϕ distribution was taken for the data and gen-level MC. Figure 6.1 shows the ϕ distribution before the application of any corrections.

The event-mixing method was used to account for the acceptance effects within CMS. The dijets of two separate events are mixed to assure that any correlations are not the result of physics. The distribution of mixed-data and mixed-gen MC is shown in figure 6.2.

The "mixed" ϕ distribution is subtracted from the "raw" ϕ distribution. The "subtracted" ϕ distributions are shown in figure 6.3.

There is an additional R-factor that must be applied to account for the resolution of CMS. The corrected ϕ distribution can be seen in figure 6.4.

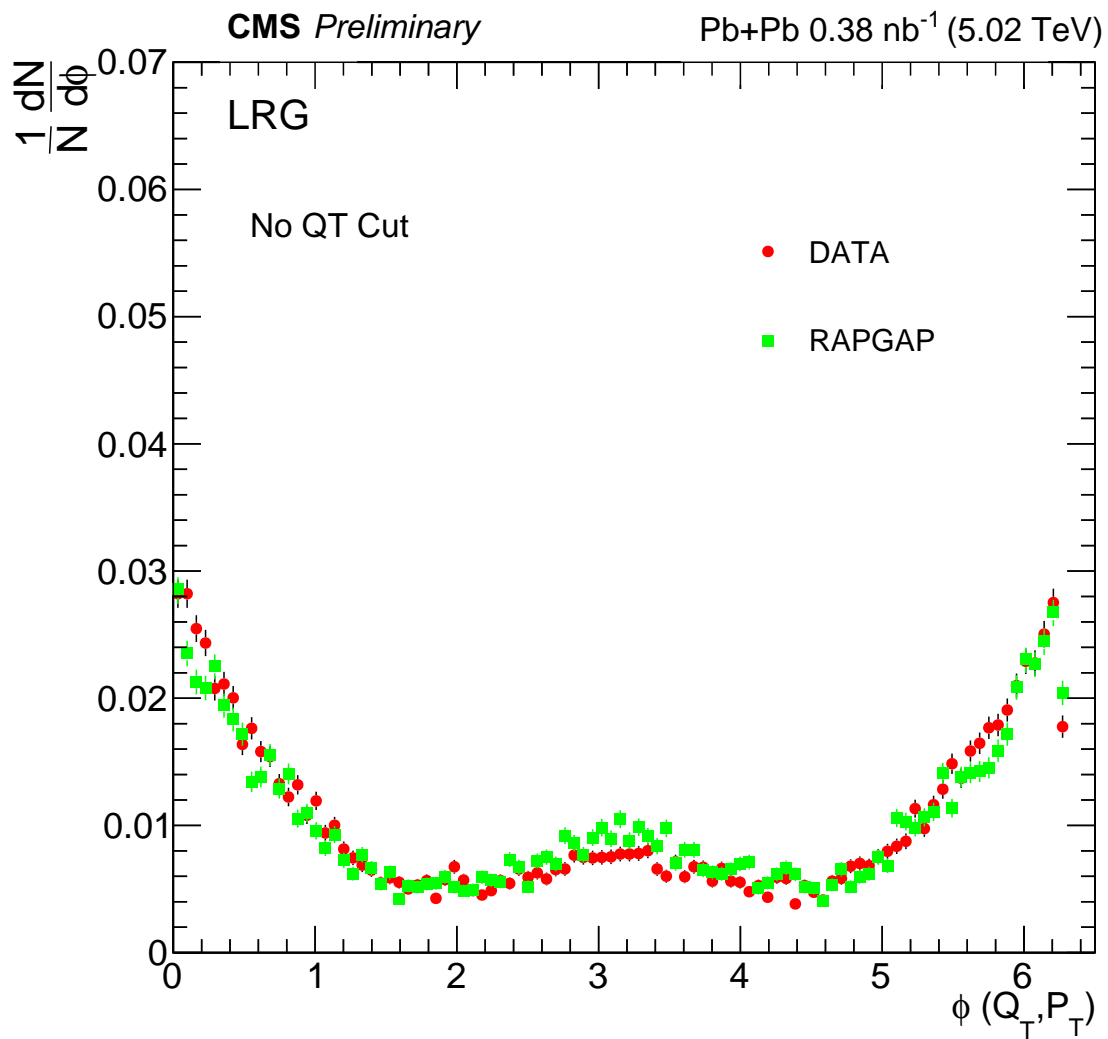


Figure 6.1: Raw ϕ distribution.

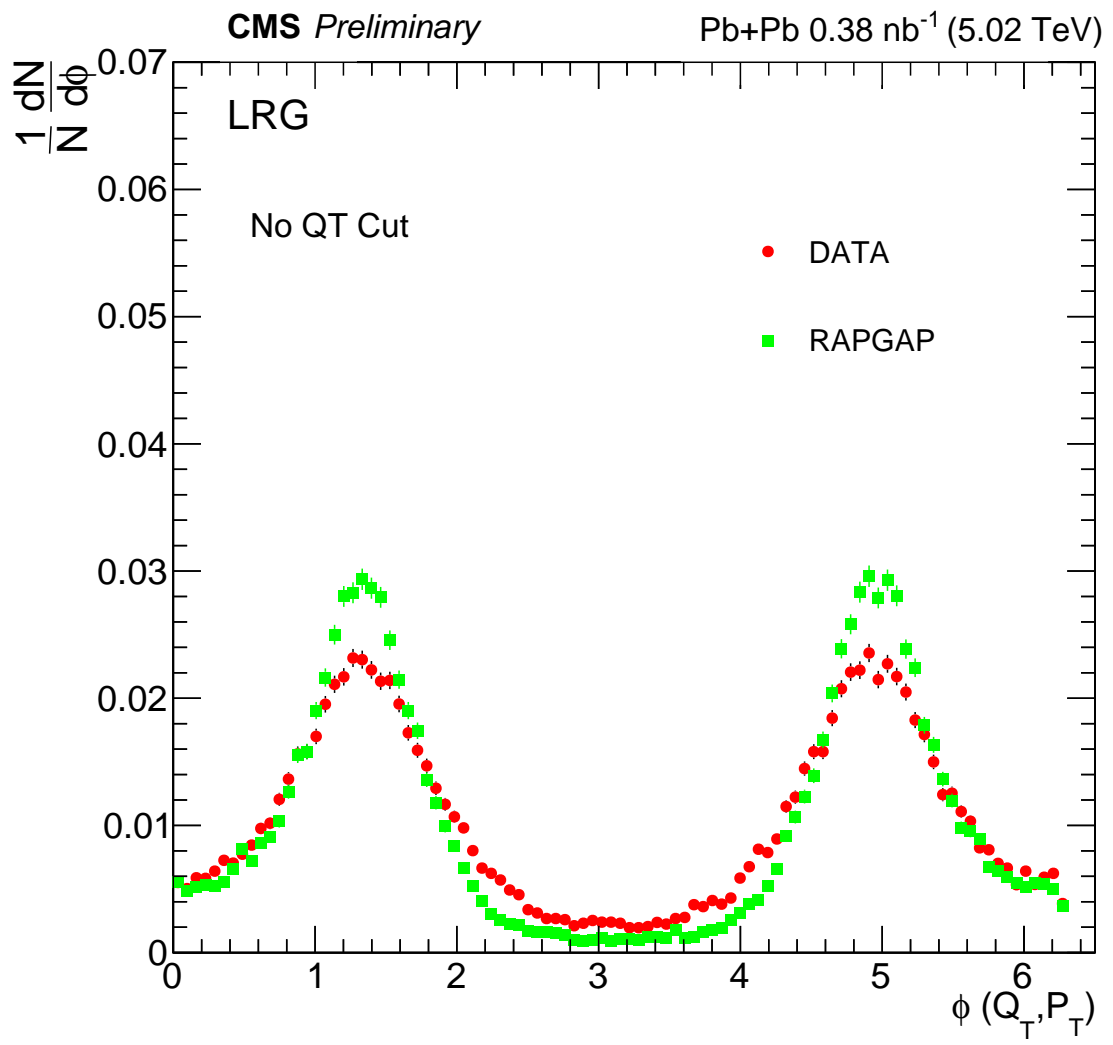


Figure 6.2: Mixed ϕ distribution.

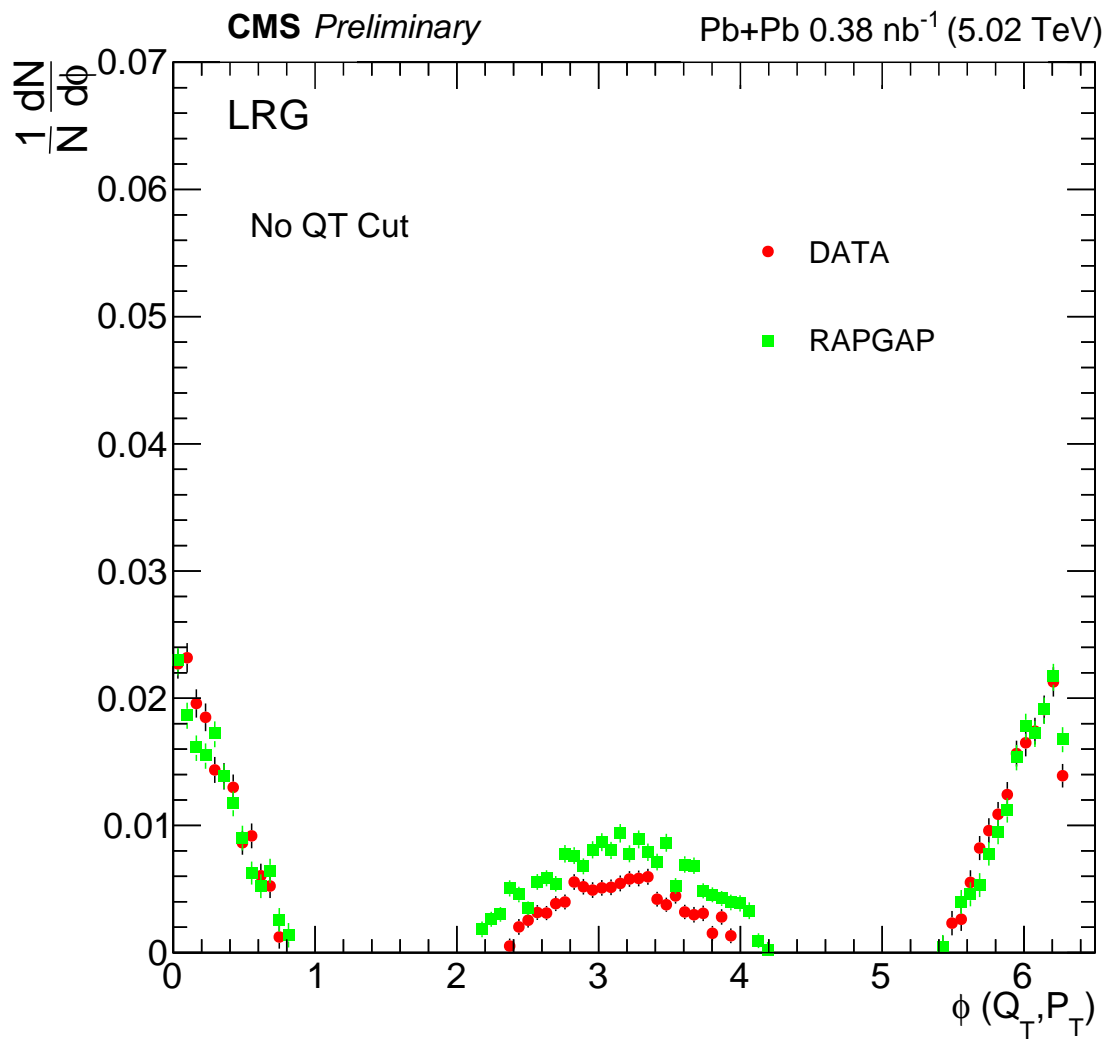


Figure 6.3: Subtracted ϕ distribution.

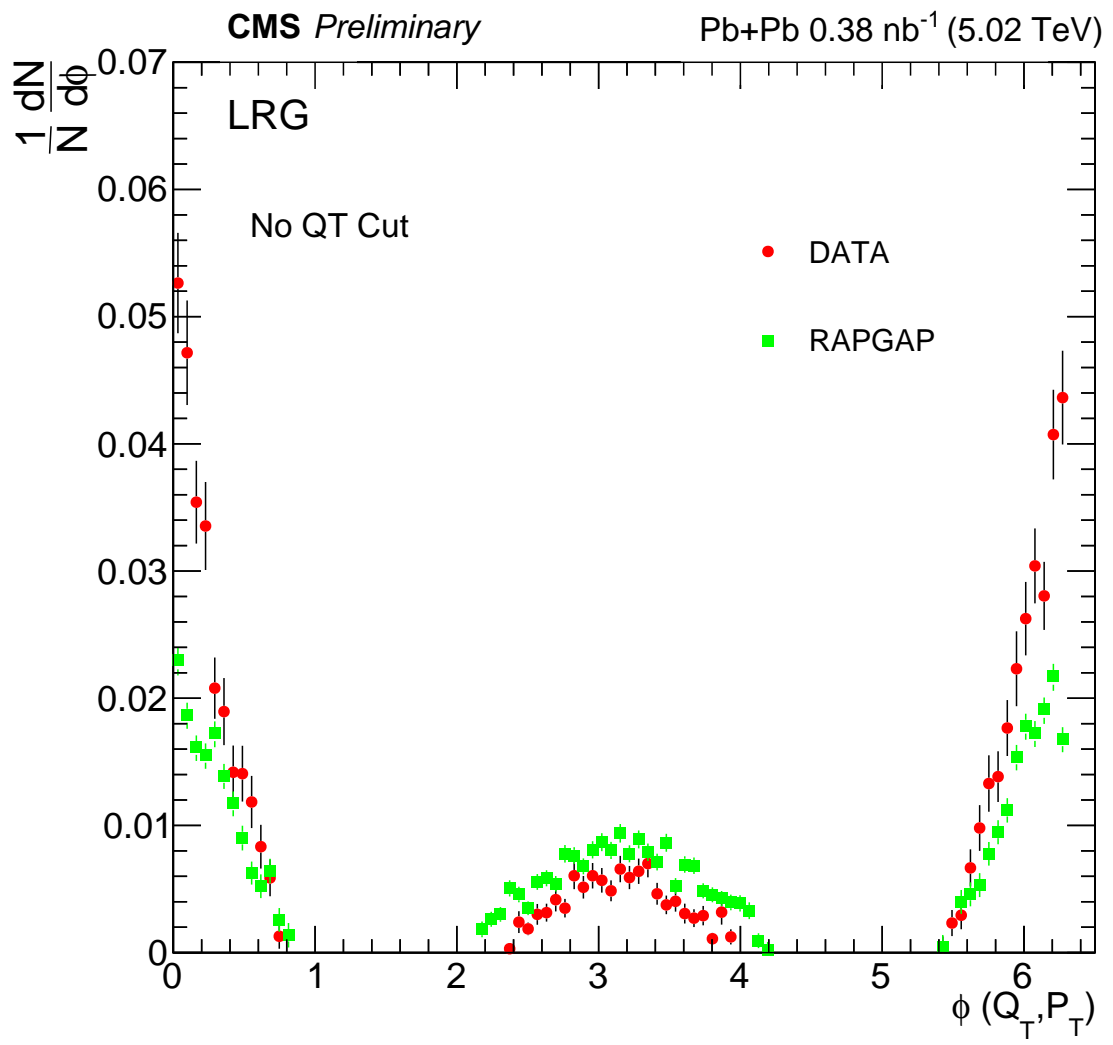


Figure 6.4: Final ϕ distribution.

Chapter 7

Systematic uncertainties

The primary sources of systematic uncertainty in this analysis are the measurements of track vertex, jet momentum, jet pseudorapidity, and HF energy.

Chapter 8

Results and conclusions

In this chapter, the angular anisotropy of the elliptic gluons is compared to theoretical predictions from variations of NLO-QCD.

References

- [1] J. Rafelski, “Connecting QGP-Heavy Ion Physics to the Early Universe,” 2013. [Nucl. Phys. Proc. Suppl. 243-244, 155 (2013)].
- [2] I. Arsene *et al.*, “Quark gluon plasma and color glass condensate at RHIC? The Perspective from the BRAHMS experiment,” *Nucl. Phys.*, vol. A757, pp. 1–27, 2005.
- [3] “The Frontiers of Nuclear Science, A Long Range Plan,” 2008.
- [4] Y. Hagiwara, Y. Hatta, and T. Ueda, “Wigner, Husimi, and generalized transverse momentum dependent distributions in the color glass condensate,” *Phys. Rev.*, vol. D94, no. 9, p. 094036, 2016.
- [5] J. G. Contreras and J. D. Tapia Takaki, “Ultra-peripheral heavy-ion collisions at the LHC,” *Int. J. Mod. Phys.*, vol. A30, p. 1542012, 2015.
- [6] C. von Weizsäcker, “Radiation emitted in collisions of very fast electrons,” *Z. Phys.*, vol. 88, pp. 612–625, 1934.
- [7] E. Williams, “Nature of the high-energy particles of penetrating radiation and status of ionization and radiation formulae,” *Phys. Rev.*, vol. 45, pp. 729–730, 1934.
- [8] F. J. Dyson and A. Lenard, “Stability of matter. I,” vol. 8, pp. 423–434, Mar. 1967.
- [9] K. Huang, *Statistical Mechanics*. John Wiley & Sons, 2 ed., 1987.
- [10] F. Halzen and A. D. Martin, *QUARKS AND LEPTONS: AN INTRODUCTORY COURSE IN MODERN PARTICLE PHYSICS*. 1984.

- [11] M. E. Peskin and D. V. Schroeder, *An Introduction to quantum field theory*. Reading, USA: Addison-Wesley, 1995.
- [12] D. Griffiths, *Introduction to elementary particles*. 2008.
- [13] “Wiki Commons,”
- [14] R. Bouchendira, P. Clade, S. Guellati-Khelifa, F. Nez, and F. Biraben, “New determination of the fine structure constant and test of the quantum electrodynamics,” *Phys. Rev. Lett.*, vol. 106, p. 080801, 2011.
- [15] G. Abbiendi *et al.*, “Measurement of the running of the QED coupling in small-angle Bhabha scattering at LEP,” *Eur. Phys. J.*, vol. C45, pp. 1–21, 2006.
- [16] R. Brock *et al.*, “Handbook of perturbative QCD: Version 1.0,” *Rev. Mod. Phys.*, vol. 67, pp. 157–248, 1995.
- [17] F. Wilczek, “QCD made simple,” *Phys. Today*, vol. 53N8, pp. 22–28, 2000.
- [18] T. Schäfer, “Phases of QCD,” in *20th Annual Hampton University Graduate Studies Program (HUGS 2005) Newport News, Virginia, May 31-June 17, 2005*, 2005.
- [19] S. Bethke, “Experimental tests of asymptotic freedom,” *Prog. Part. Nucl. Phys.*, vol. 58, pp. 351–386, 2007.
- [20] A. Deur, S. J. Brodsky, and G. F. de Teramond, “The QCD Running Coupling,” *Prog. Part. Nucl. Phys.*, vol. 90, pp. 1–74, 2016.
- [21] J. D. Bjorken, “Asymptotic Sum Rules at Infinite Momentum,” *Phys. Rev.*, vol. 179, pp. 1547–1553, 1969.
- [22] M. Thomson, *Modern particle physics*. New York: Cambridge University Press, 2013.
- [23] L. McLerran, “The Color Glass Condensate and Glasma,” 2008.

- [24] F. Gelis, “Color glass condensate and glasma,” *Nuclear Physics A*, vol. 854, no. 1, pp. 10 – 17, 2011. Saturation, the Color Glass Condensate and the Glasma: What Have We Learned from RHIC?
- [25] J. Bjorken, “Highly Relativistic Nucleus-Nucleus Collisions: The Central Rapidity Region,” *Phys.Rev.*, vol. D27, pp. 140–151, 1983.
- [26] S. Shimizu, “Low Q^{**2} Structure Functions including the Longitudinal Structure Function,” in *QCD and high energy interactions. Proceedings, 44th Rencontres de Moriond, La Thuile, Italy, March 14-21, 2009*, pp. 301–304, 2009.
- [27] A. Martin, W. Stirling, R. Thorne, and G. Watt, “Parton distributions for the LHC,” *Eur.Phys.J.*, vol. C63, pp. 189–285, 2009.
- [28] K. J. Eskola, H. Paukkunen, and C. A. Salgado, “An Improved global analysis of nuclear parton distribution functions including RHIC data,” *JHEP*, vol. 0807, p. 102, 2008.
- [29] J. Pumplin, D. Stump, J. Huston, H. Lai, P. M. Nadolsky, *et al.*, “New generation of parton distributions with uncertainties from global QCD analysis,” *JHEP*, vol. 0207, p. 012, 2002.
- [30] S. Chatrchyan *et al.*, “ J/ψ and $\psi(2s)$ production in pp collisions at $\sqrt{s} = 7$ tev,” *Journal of High Energy Physics*, vol. 2012, no. 2, 2012.
- [31] Y. Hatta, B.-W. Xiao, and F. Yuan, “Probing the Small- x Gluon Tomography in Correlated Hard Diffractive Dijet Production in Deep Inelastic Scattering,” *Phys. Rev. Lett.*, vol. 116, no. 20, p. 202301, 2016.
- [32] D. Boer *et al.*, “Gluons and the quark sea at high energies: Distributions, polarization, tomography,” 2011.
- [33] M. Diehl, “Generalized parton distributions,” *Phys. Rept.*, vol. 388, pp. 41–277, 2003.
- [34] H. Satz, “The SPS heavy ion programme,” *Phys.Rept.*, vol. 403-404, pp. 33–50, 2004.

- [35] P. Steinberg, “Relativistic heavy ion physics: Results from AGS to RHIC,” *eConf*, vol. C020620, p. FRBT03, 2002.
- [36] H. Song, S. A. Bass, U. Heinz, T. Hirano, and C. Shen, “200 a gev Au + Au collisions serve a nearly perfect quark-gluon liquid,” *Phys. Rev. Lett.*, vol. 106, p. 192301, May 2011.
- [37] R. S. Bhalerao, “Relativistic heavy-ion collisions,” pp. 219–239. 21 p, Apr 2014. Comments: Updated version of the lectures given at the First Asia-Europe-Pacific School of High-Energy Physics, Fukuoka, Japan, 14-27 October 2012. Published as a CERN Yellow Report (CERN-2014-001) and KEK report (KEK-Proceedings-2013-8), K. Kawagoe and M. Mulders (eds.), 2014, p. 219. Total 21 pages.
- [38] S. Hands, “The Phase diagram of QCD,” *Contemp.Phys.*, vol. 42, pp. 209–225, 2001.
- [39] M. Gyulassy and M. Plumer, “Jet Quenching in Dense Matter,” *Phys.Lett.*, vol. B243, pp. 432–438, 1990.
- [40] T. Matsui and H. Satz, “ J/ψ Suppression by Quark-Gluon Plasma Formation,” *Phys.Lett.*, vol. B178, p. 416, 1986.
- [41] S. Margetis, K. Safarik, and O. Villalobos Baillie, “Strangeness production in heavy-ion collisions,” *Ann.Rev.Nucl.Part.Sci.*, vol. 50, pp. 299–342, 2000.
- [42] B. Alver *et al.*, “Importance of correlations and fluctuations on the initial source eccentricity in high-energy nucleus-nucleus collisions,” *Phys. Rev. C*, vol. 77, p. 014906, Jan 2008.
- [43] S. Chatrchyan *et al.*, “Multiplicity and transverse momentum dependence of two- and four-particle correlations in pPb and PbPb collisions,” *Phys.Lett.*, vol. B724, pp. 213–240, 2013.
- [44] F. Karsch, E. Laermann, and A. Peikert, “Quark mass and flavor dependence of the QCD phase transition,” *Nucl.Phys.*, vol. B605, pp. 579–599, 2001.
- [45] B. Abelev *et al.*, “Long-range angular correlations on the near and away side in p -Pb collisions at $\sqrt{s_{NN}} = 5.02$ TeV,” *Phys.Lett.*, vol. B719, pp. 29–41, 2013.

- [46] J.-Y. Ollitrault, “Anisotropy as a signature of transverse collective flow,” *Phys.Rev.*, vol. D46, pp. 229–245, 1992.
- [47] P. Sorensen, “Elliptic Flow: A Study of Space-Momentum Correlations In Relativistic Nuclear Collisions,” 2009.
- [48] R. Bhalerao, N. Borghini, and J. Ollitrault, “Genuine collective flow from Lee-Yang zeroes,” *Phys.Lett.*, vol. B580, pp. 157–162, 2004.
- [49] N. Borghini, P. M. Dinh, and J.-Y. Ollitrault, “Flow analysis from cumulants: A Practical guide,” 2001.
- [50] K. Ackermann *et al.*, “Elliptic flow in Au + Au collisions at $(S(NN))^{**}(1/2) = 130$ GeV,” *Phys.Rev.Lett.*, vol. 86, pp. 402–407, 2001.
- [51] N. Borghini, R. Bhalerao, and J. Ollitrault, “Anisotropic flow from Lee-Yang zeroes: A Practical guide,” *J.Phys.*, vol. G30, pp. S1213–S1216, 2004.
- [52] A. Bandyopadhyay, *Non-perturbative study of spectral function and its application in Quark Gluon Plasma*. PhD thesis, Saha Inst., 2017.
- [53] E. Witten, “Cosmic Separation of Phases,” *Phys.Rev.*, vol. D30, pp. 272–285, 1984.
- [54] H. Wang, *Study of particle ratio fluctuations and charge balance functions at RHIC*. PhD thesis, Michigan State U., 2012.
- [55] J. D. Bjorken, “Highly relativistic nucleus-nucleus collisions: The central rapidity region,” *Phys. Rev. D*, vol. 27, pp. 140–151, Jan 1983.
- [56] R. Vogt, “Quark-Gluon Plasma Signatures,” 1998.
- [57] G. Roland, K. Safarik, and P. Steinberg, “Heavy-ion collisions at the LHC,” *Prog.Part.Nucl.Phys.*, vol. 77, pp. 70–127, 2014.

- [58] L. Frankfurt, M. Strikman, and C. Weiss, “Small- x physics: From hera to lhc and beyond,” *Ann. Rev. Nucl. Part. Sci.*, vol. 55, pp. 403–465, 2005.
- [59] R. Vogt, “Heavy quark production in heavy ion colliders,” *Heavy Ion Phys.*, vol. 18, pp. 11–20, 2003.
- [60] A. V. Belitsky, X.-d. Ji, and F. Yuan, “Quark imaging in the proton via quantum phase space distributions,” *Phys. Rev.*, vol. D69, p. 074014, 2004.
- [61] T. Altinoluk, N. Armesto, G. Beuf, and A. H. Rezaeian, “Diffractive Dijet Production in Deep Inelastic Scattering and Photon-Hadron Collisions in the Color Glass Condensate,” *Phys. Lett.*, vol. B758, pp. 373–383, 2016.
- [62] D. Chakrabarti, T. Maji, C. Mondal, and A. Mukherjee, “Wigner distributions and orbital angular momentum of a proton,” *Eur. Phys. J.*, vol. C76, no. 7, p. 409, 2016.
- [63] D. Griffiths, *Introduction to Electrodynamics*. Prentice Hall, 1999.
- [64] A. Baltz, G. Baur, D. d’Enterria, L. Frankfurt, F. Gelis, *et al.*, “The Physics of Ultraperipheral Collisions at the LHC,” *Phys.Rept.*, vol. 458, pp. 1–171, 2008.
- [65] J. D. Jackson, *Classical electrodynamics*. New York, NY: Wiley, 3rd ed. ed., 1999.
- [66] C. A. Bertulani, S. R. Klein, and J. Nystrand, “Physics of ultra-peripheral nuclear collisions,” *Ann.Rev.Nucl.Part.Sci.*, vol. 55, pp. 271–310, 2005.
- [67] P. Stankus, “Direct photon production in relativistic heavy-ion collisions,” *Annual Review of Nuclear and Particle Science*, vol. 55, no. 1, pp. 517–554, 2005.
- [68] J. Hufner, B. Kopeliovich, and A. B. Zamolodchikov, “Inelastic J / psi photoproduction off nuclei: Gluon enhancement or double color exchange?,” *Z.Phys.*, vol. A357, pp. 113–120, 1997.

- [69] M. Wilde, “Measurement of direct photons in pp and pb–pb collisions with {ALICE},” *Nuclear Physics A*, vol. 904–905, no. 0, pp. 573c – 576c, 2013. The Quark Matter 2012 Proceedings of the {XXIII} International Conference on Ultrarelativistic Nucleus-Nucleus Collisions.
- [70] V. Andreev *et al.*, “Diffractive Dijet Production with a Leading Proton in ep Collisions at HERA,” *JHEP*, vol. 05, p. 056, 2015.
- [71] V. Rebyakova, M. Strikman, and M. Zhalov, “Coherent rho and J/psi photoproduction in ultraperipheral processes with electromagnetic dissociation of heavy ions at RHIC and LHC,” *Phys.Lett.*, vol. B710, pp. 647–653, 2012.
- [72] S. Chekanov *et al.*, “Exclusive photoproduction of J / psi mesons at HERA,” *Eur.Phys.J.*, vol. C24, pp. 345–360, 2002.
- [73] M. Klasen, “Hard photoproduction at hera,” 2007.
- [74] H. Emling, “Electromagnetic excitation of the two phonon giant dipole resonance,” *Prog.Part.Nucl.Phys.*, vol. 33, pp. 729–786, 1994.
- [75] E. de Passos, M. Hussein, L. Canto, and B. Carlson, “The Mean energy, strength and width of triple giant dipole resonances,” *Phys.Rev.*, vol. C65, p. 034326, 2002.
- [76] M. Ryskin, “Diffractive J / psi electroproduction in LLA QCD,” *Z.Phys.*, vol. C57, pp. 89–92, 1993.
- [77] M. Goldhaber and E. Teller, “On nuclear dipole vibrations,” *Phys.Rev.*, vol. 74, pp. 1046–1049, 1948.
- [78] V. Goncalves and M. Machado, “Vector Meson Production in Coherent Hadronic Interactions: An update on predictions for RHIC and LHC,” *Phys.Rev.*, vol. C84, p. 011902, 2011.

- [79] T. Lappi and H. Mantysaari, “ J/ψ production in ultraperipheral Pb+Pb and p +Pb collisions at energies available at the CERN Large Hadron Collider,” *Phys.Rev.*, vol. C87, no. 3, p. 032201, 2013.
- [80] J. Gaiser, “Charmonium Spectroscopy From Radiative Decays of the J/ψ and ψ' ,” 1982.
- [81] A. Aktas *et al.*, “Elastic J/ψ production at HERA,” *Eur.Phys.J.*, vol. C46, pp. 585–603, 2006.
- [82] E. Abbas *et al.*, “Charmonium and e^+e^- pair photoproduction at mid-rapidity in ultra-peripheral Pb-Pb collisions at $\sqrt{s_{NN}} = 2.76$ TeV,” *Eur.Phys.J.*, vol. C73, p. 2617, 2013.
- [83]
- [84] J. Nystrand, “Electromagnetic interactions in nucleus nucleus and proton proton collisions,” *Nucl. Phys.*, vol. A752, pp. 470–479, 2005.
- [85] C. Adler *et al.*, “Coherent ρ^0 production in ultra-peripheral heavy ion collisions,” *Phys. Rev. Lett.*, vol. 89, p. 272302, 2002.
- [86] V. Guzey and M. Zhalov, “Rapidity and momentum transfer distributions of coherent J/ψ photoproduction in ultraperipheral pPb collisions at the LHC,” *JHEP*, vol. 1402, p. 046, 2014.
- [87] L. Frankfurt, M. Strikman, and M. Zhalov, “Large t diffractive ρ -meson photoproduction with target dissociation in ultraperipheral p a and a a collisions at lhc,” 2006.
- [88] A. J. Baltz, S. R. Klein, and J. Nystrand, “Coherent vector meson photoproduction with nuclear breakup in relativistic heavy ion collisions,” *Phys. Rev. Lett.*, vol. 89, p. 012301, 2002.
- [89] S. R. Klein and J. Nystrand, “Photoproduction of quarkonium in proton proton and nucleus nucleus collisions,” *Phys. Rev. Lett.*, vol. 92, p. 142003, 2004.

- [90] B. Abelev *et al.*, “Coherent J/ψ photoproduction in ultra-peripheral Pb-Pb collisions at $\sqrt{s_{NN}} = 2.76$ TeV,” *Phys.Lett.*, vol. B718, pp. 1273–1283, 2013.
- [91] S. Klein and J. Nystrand, “Ultraperipheral nuclear collisions,” *Phys. Today*, vol. 70, no. 10, pp. 40–47, 2017.
- [92] A. Adeluyi and C. A. Bertulani, “Gluon distributions in nuclei probed at energies available at the CERN large hadron collider,” *Phys. Rev. C*, vol. 84, p. 024916, Aug 2011.
- [93] B. B. Abelev *et al.*, “Exclusive J/ψ photoproduction off protons in ultra-peripheral p-Pb collisions at $\sqrt{s_{NN}}=5.02$ TeV,” 2014.
- [94] V. Khachatryan *et al.*, “Coherent J/ψ photoproduction in ultra-peripheral PbPb collisions at $\sqrt{s_{NN}} = 2.76$ TeV with the CMS experiment,” *Phys. Lett.*, vol. B772, pp. 489–511, 2017.
- [95] A. Aktas *et al.*, “Diffractive photoproduction of ρ mesons with large momentum transfer at hera,” *Phys. Lett.*, vol. B638, pp. 422–431, 2006.
- [96] P. Faccioli, C. Lourenco, J. Seixas, and H. K. Wohri, “Towards the experimental clarification of quarkonium polarization,” *Eur.Phys.J.*, vol. C69, pp. 657–673, 2010.
- [97] S. R. Klein and J. Nystrand, “Exclusive vector meson production in relativistic heavy ion collisions,” *Phys. Rev. C*, vol. 60, p. 014903, Jun 1999.
- [98] S. R. Klein and J. Nystrand, “Interference in exclusive vector meson production in heavy-ion collisions,” *Phys. Rev. Lett.*, vol. 84, pp. 2330–2333, Mar 2000.
- [99] T. Teubner, “Diffractive production of vector mesons and the gluon at small x ,” *AIP Conf. Proc.*, vol. 792, pp. 416–419, 2005.
- [100] S. J. Brodsky, L. Frankfurt, J. Gunion, A. H. Mueller, and M. Strikman, “Diffractive leptoproduction of vector mesons in QCD,” *Phys.Rev.*, vol. D50, pp. 3134–3144, 1994.

- [101] M. L. Miller, K. Reygers, S. J. Sanders, and P. Steinberg, “Glauber modeling in high energy nuclear collisions,” *Ann.Rev.Nucl.Part.Sci.*, vol. 57, pp. 205–243, 2007.
- [102] V. Guzey, M. Strikman, and M. Zhalov, “Disentangling coherent and incoherent J/ψ photoproduction on nuclei by neutron tagging in ultraperipheral ion collisions at the LHC,” 2013.
- [103] M. Strikman, M. Tverskoy, and M. Zhalov, “Neutron tagging of quasielastic J/ψ photo-production off nucleus in ultraperipheral heavy ion collisions at RHIC energies,” *Phys.Lett.*, vol. B626, pp. 72–79, 2005.
- [104] V. Rebyakova, M. Strikman, and M. Zhalov, “Coherent ρ and J/Ψ photoproduction in ultraperipheral processes with electromagnetic dissociation of heavy ions at RHIC and LHC,” *Physics Letters B*, vol. 710, no. 4–5, pp. 647 – 653, 2012.
- [105] I. A. Pshenichnov, J. P. Bondorf, I. N. Mishustin, A. Ventura, and S. Masetti, “Mutual heavy ion dissociation in peripheral collisions at ultrarelativistic energies,” *Phys. Rev. C*, vol. 64, p. 024903, Jul 2001.
- [106] I. A. Pshenichnov, I. N. Mishustin, J. P. Bondorf, A. S. Botvina, and A. S. Iljinov, “Particle emission following coulomb excitation in ultrarelativistic heavy-ion collisions,” *Phys. Rev. C*, vol. 60, p. 044901, Sep 1999.
- [107] P. Chomaz, “Collective excitations in nuclei,” 1997.
- [108] M. Chiu, A. Denisov, E. Garcia, J. Katzy, A. Makeev, M. Murray, and S. White, “Measurement of mutual coulomb dissociation in $\sqrt{s_{NN}} = 130\text{GeV}$ $au + au$ collisions,” *Phys. Rev. Lett.*, vol. 89, p. 012302, Jun 2002.
- [109] V. Guzey, E. Kryshen, M. Strikman, and M. Zhalov, “Evidence for nuclear gluon shadowing from the ALICE measurements of pbpb ultraperipheral exclusive production,” *Physics Letters B*, vol. 726, no. 1–3, pp. 290 – 295, 2013.

- [110] K. Eskola, H. Paukkunen, and C. Salgado, “EPS09: A New Generation of NLO and LO Nuclear Parton Distribution Functions,” *JHEP*, vol. 0904, p. 065, 2009.
- [111] L. Frankfurt, V. Guzey, and M. Strikman, “Leading Twist Nuclear Shadowing Phenomena in Hard Processes with Nuclei,” *Phys.Rept.*, vol. 512, pp. 255–393, 2012.
- [112] A. Adeluyi and T. Nguyen, “Coherent photoproduction of ψ and Υ mesons in ultraperipheral pPb and PbPb collisions at the CERN Large Hadron Collider at $\sqrt{S_{NN}} = 5$ TeV and $\sqrt{S_{NN}} = 2.76$ TeV,” *Phys. Rev. C*, vol. 87, p. 027901, Feb 2013.
- [113] A. Cisek, W. Schafer, and A. Szczurek, “Exclusive coherent production of heavy vector mesons in nucleus-nucleus collisions at LHC,” *Phys.Rev.*, vol. C86, p. 014905, 2012.
- [114] R. Chudasama and D. Dutta, “Exclusive Photoproduction of Upsilon in pPb collisions with the CMS,” *PoS*, vol. ICPAQGP2015, p. 042, 2017.
- [115] M. Aaboud *et al.*, “Evidence for light-by-light scattering in heavy-ion collisions with the ATLAS detector at the LHC,” *Nature Phys.*, vol. 13, no. 9, pp. 852–858, 2017.
- [116] A. Collaboration, “ATLAS Event Display: Light-by-Light Scattering.” General Photo, Aug 2017.
- [117] D. d’Enterria, “Hard spectra and qcd matter: Experimental review,” *J. Phys.*, vol. G30, pp. S767–S774, 2004.
- [118] M. Strikman, R. Vogt, and S. White, “Probing small x parton densities in ultraperipheral a a and p a collisions at the lhc,” *Phys. Rev. Lett.*, vol. 96, p. 082001, 2006.
- [119] V. Guzey and M. Klasen, “A fresh look at factorization breaking in diffractive photoproduction of dijets at HERA at next-to-leading order QCD,” *Eur. Phys. J.*, vol. C76, no. 8, p. 467, 2016.
- [120] V. Guzey and M. Klasen, “Diffractive dijet photoproduction in ultraperipheral collisions at the LHC in next-to-leading order QCD,” *JHEP*, vol. 04, p. 158, 2016.

- [121] S. Chekanov *et al.*, “Deep inelastic scattering with leading protons or large rapidity gaps at HERA,” *Nucl. Phys.*, vol. B816, pp. 1–61, 2009.
- [122] T. Bauer, R. Spital, D. Yennie, and F. Pipkin, “The Hadronic Properties of the Photon in High-Energy Interactions,” *Rev.Mod.Phys.*, vol. 50, p. 261, 1978.
- [123] L. Frankfurt, M. Strikman, and M. Zhalov, “Elastic and large t rapidity gap vector meson production in ultraperipheral proton-ion collisions,” *Phys.Lett.*, vol. B640, pp. 162–169, 2006.
- [124] C. Alexa *et al.*, “Elastic and Proton-Dissociative Photoproduction of J/psi Mesons at HERA,” *Eur.Phys.J.*, vol. C73, p. 2466, 2013.
- [125] F. D. Aaron *et al.*, “Measurement of the cross section for diffractive deep-inelastic scattering with a leading proton at HERA,” *Eur. Phys. J.*, vol. C71, p. 1578, 2011.
- [126] F. D. Aaron *et al.*, “Diffractive Dijet Photoproduction in ep Collisions at HERA,” *Eur. Phys. J.*, vol. C70, pp. 15–37, 2010.
- [127] S. Donnachie, H. G. Dosch, O. Nachtmann, and P. Landshoff, “Pomeron physics and QCD,” *Camb.Monogr.Part.Phys.Nucl.Phys.Cosmol.*, vol. 19, pp. 1–347, 2002.
- [128] T. Sjöstrand, S. Mrenna, and P. Skands, “Pythia 6.4 physics and manual,” *Journal of High Energy Physics*, vol. 2006, no. 05, p. 026, 2006.
- [129] J. A. Crittenden, “Exclusive production of neutral vector mesons at the electron - proton collider HERA,” 1997.
- [130] L. Evans and P. Bryant, “LHC Machine,” *JINST*, vol. 3, p. S08001, 2008.
- [131] G. Aad *et al.*, “The ATLAS Experiment at the CERN Large Hadron Collider,” *JINST*, vol. 3, p. S08003, 2008.

- [132] K. Aamodt *et al.*, “The ALICE experiment at the CERN LHC,” *JINST*, vol. 3, p. S08002, 2008.
- [133] J. Alves, A. Augusto *et al.*, “The LHCb Detector at the LHC,” *JINST*, vol. 3, p. S08005, 2008.
- [134] V. Andreev, X. Aslanoglou, A. Azman, M. Bakirci, S. Basegmez, *et al.*, “Performance studies of a full-length prototype for the CASTOR forward calorimeter at the CMS experiment,” *Eur.Phys.J.*, vol. C67, pp. 601–615, 2010.
- [135] G. Bayatian *et al.*, “CMS technical design report, volume II: Physics performance,” *J.Phys.*, vol. G34, pp. 995–1579, 2007.
- [136] D. G. d’Enterria *et al.*, “CMS physics technical design report: Addendum on high density QCD with heavy ions,” *J. Phys.*, vol. G34, pp. 2307–2455, 2007.
- [137] L. R. F. Castillo, “The atlas and cms detectors,” in *The Search and Discovery of the Higgs Boson*, 2053-2571, pp. 4–1 to 4–8, Morgan and Claypool Publishers, 2015.
- [138] *The CMS tracker: addendum to the Technical Design Report*. Technical Design Report CMS, Geneva: CERN, 2000.
- [139] S. Chatrchyan *et al.*, “Alignment of the CMS Silicon Tracker during Commissioning with Cosmic Rays,” *JINST*, vol. 5, p. T03009, 2010.
- [140] A. Benaglia, “The CMS ECAL performance with examples,” *JINST*, vol. 9, p. C02008, 2014.
- [141] S. Baffioni, C. Charlot, *et al.*, “Electron reconstruction in cms,” *CMS NOTE 2006/40*, 2006.
- [142] G. L. Bayatian *et al.*, “CMS Physics,” 2006.
- [143] G. Baiatian *et al.*, “Design, Performance, and Calibration of CMS Hadron-Barrel Calorimeter Wedges,” 2007.

- [144] M. M. I. Bloch, E. J. A., E. D. Barge, C. Campagnari, P. Kalavase, V. Krutelyov, D. Kovalskyi, J. Ribnik, and N. Amapane, “Muon identification in cms,” *CMS Note*, vol. 2008/098, 2008.
- [145] T. C. collaboration, “Performance of cms muon reconstruction in pp collision events at $\sqrt{s} = 7$ tev,” *Journal of Instrumentation*, vol. 7, no. 10, p. P10002, 2012.
- [146] C. Albajar, J. de Troconiz, J. Rohlf, and G. Wrochna, “Conceptual design of an improved CMS RPC muon trigger using the hadron outer scintillators,” *Nucl.Instrum.Meth.*, vol. A545, pp. 97–113, 2005.
- [147] O. A. Grachov *et al.*, “Status of zero degree calorimeter for CMS experiment,” *AIP Conf.Proc.*, vol. 867, pp. 258–265, 2006.
- [148] A. J. Baltz, C. Chasman, and S. N. White, “Correlated forward–backward dissociation and neutron spectra as a luminosity monitor in heavy-ion colliders,” *Nuclear Instruments and Methods in Physics Research Section A: Accelerators, Spectrometers, Detectors and Associated Equipment*, vol. 417, no. 1, pp. 1 – 8, 1998.
- [149] F. Beaudette, “The CMS Particle Flow Algorithm,” in *Proceedings, International Conference on Calorimetry for the High Energy Frontier (CHEF 2013): Paris, France, April 22-25, 2013*, pp. 295–304, 2013.
- [150] S. D. Ellis and D. E. Soper, “Successive combination jet algorithm for hadron collisions,” *Phys. Rev.*, vol. D48, pp. 3160–3166, 1993.
- [151] A. M. Sirunyan *et al.*, “Particle-flow reconstruction and global event description with the CMS detector,” *JINST*, vol. 12, no. 10, p. P10003, 2017.
- [152] C. Collaboration, “CMS Luminosity Based on Pixel Cluster Counting - Summer 2013 Update,” 2013.
- [153] S. Chatrchyan *et al.*, “Measurement of CMS Luminosity,” 2010.

- [154] M. W. Krasny, J. Chwastowski, and K. Slowikowski, “Luminosity measurement method for lhc: The theoretical precision and the experimental challenges,” 2006.
- [155] CMS, “Measurement of CMS Luminosity,” 2010.
- [156] A. Kornmayer, “The CMS pixel luminosity telescope,” *Nucl. Instrum. Meth.*, vol. A824, pp. 304–306, 2016.
- [157] M. Guthoff, “Instrumentation for beam radiation and luminosity measurement in the CMS experiment using novel detector technologies,” *Nucl. Instrum. Meth.*, vol. A845, pp. 565–569, 2017.
- [158] S. van der Meer, “Calibration of the Effective Beam Height in the ISR,” 1968.
- [159] L. Bonolis, “Walther Bothe and Bruno Rossi: the birth and development of coincidence methods in cosmic-ray physics,” *Am. J. Phys.*, vol. 79, p. 1133, 2011.
- [160] S. Dasu *et al.*, “CMS. The TriDAS project. Technical design report, vol. 1: The trigger systems,” 2000.
- [161] P. Sphicas, “CMS: The TriDAS project. Technical design report, Vol. 2: Data acquisition and high-level trigger,” 2002.
- [162] J. Alwall, A. Ballestrero, P. Bartalini, S. Belov, E. Boos, *et al.*, “A Standard format for Les Houches event files,” *Comput.Phys.Commun.*, vol. 176, pp. 300–304, 2007.

Appendix A

Monte Carlo Generation and Reconstruction

The Monte Carlo (MC) for this analysis was generated using the RAPGAP software package. RAPGAP is a generator for electron-proton MC. The structure functions measured at HERA are used to model a variety of diffractive processes. Each event has a characteristic energy for the virtual photon exchanged by the electron and proton. This photon energy is used to reweigh the MC to model the energy distribution of the Weizacker Williams photon flux.

$$w(E) = \frac{dN_\gamma^{eff}}{dE} / \frac{dN_\gamma^{RAPGAP}}{dE} \quad (\text{A.1})$$

dN_γ^{RAPGAP}/dE is obtained by fitting the formula for the total electron-proton cross-section, $\sigma_{\gamma p}$ to the RAPGAP MC's energy distribution.

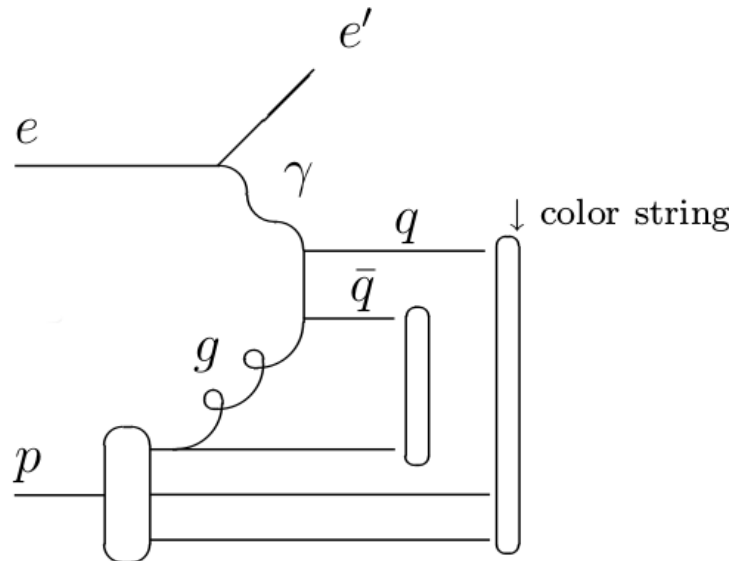


Figure A.1: RAPGAP process: boson-gluon fusion.

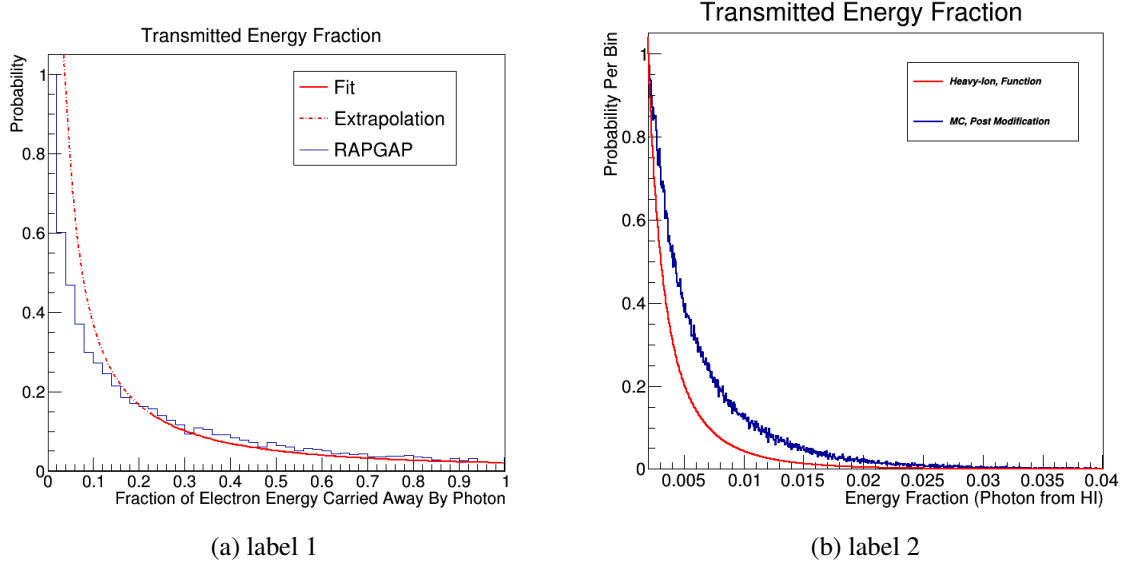


Figure A.2: Left: Energy Distribution Before Fitting, Right: Energy Distribution After Fitting

$$\frac{d^2\sigma_{ep}}{dy dQ^2} = \frac{\alpha}{2\pi Q^2} \left(\frac{1 + (1-y)^2}{y} - \frac{2(1-y)}{y} \cdot \frac{Q_{min}^2}{Q^2} \right) \cdot \sigma_{\gamma^* p}^{tot}(W_{\gamma^* p}), \quad (\text{A.2})$$

where

$$Q_{min}^2 \approx \frac{m_e^2 y^2}{1-y}. \quad (\text{A.3})$$

In this context, y is the energy fraction carried away from the electron by the mediating virtual photon, Q^2 is the photon virtuality, m_e is the electron mass, $\sigma_{\gamma^* p}^{tot}(W_{\gamma^* p})$ is the total photon-proton cross section, and $W_{\gamma^* p}$ is the center of mass energy of the photon-proton collision.